



저작자표시-비영리-변경금지 2.0 대한민국

이용자는 아래의 조건을 따르는 경우에 한하여 자유롭게

- 이 저작물을 복제, 배포, 전송, 전시, 공연 및 방송할 수 있습니다.

다음과 같은 조건을 따라야 합니다:



저작자표시. 귀하는 원저작자를 표시하여야 합니다.



비영리. 귀하는 이 저작물을 영리 목적으로 이용할 수 없습니다.



변경금지. 귀하는 이 저작물을 개작, 변형 또는 가공할 수 없습니다.

- 귀하는, 이 저작물의 재이용이나 배포의 경우, 이 저작물에 적용된 이용허락조건을 명확하게 나타내어야 합니다.
- 저작권자로부터 별도의 허가를 받으면 이러한 조건들은 적용되지 않습니다.

저작권법에 따른 이용자의 권리는 위의 내용에 의하여 영향을 받지 않습니다.

이것은 [이용허락규약\(Legal Code\)](#)을 이해하기 쉽게 요약한 것입니다.

[Disclaimer](#)

Doctoral Thesis

Two-Dimensional Materials for
Organic Reaction Vessels and
Proton Exchange Membranes

Seong In Yoon

Department of Energy Engineering

(Energy Engineering)

Graduate School of UNIST

2020

Two-Dimensional Materials for
Organic Reaction Vessels and
Proton Exchange Membranes

Seong In Yoon

Department of Energy Engineering
(Energy Engineering)

Graduate School of UNIST

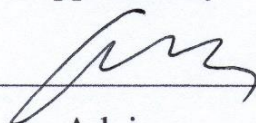
Two-Dimensional Materials for
Organic Reaction Vessels and
Proton Exchange Membranes

A thesis/dissertation submitted to the Graduate School of UNIST in partial
fulfillment of the requirements for the degree of Doctor of Philosophy

Seong In Yoon

12/04/2019

Approved by



Advisor

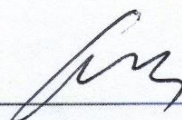
Hyeon Suk Shin

Two-Dimensional Materials for
Organic Reaction Vessels and
Proton Exchange Membranes

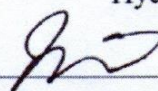
Seong In Yoon

This certifies that the thesis/dissertation of Seong In Yoon is approved.

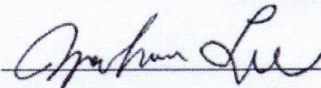
12/04/2019



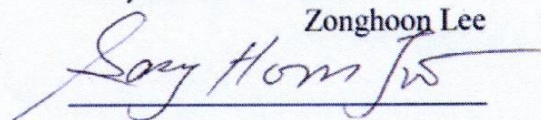
Hyeon Suk Shin



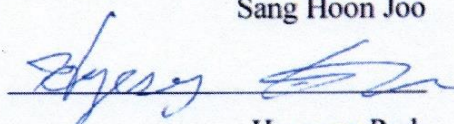
Tae-Young Kim



Zonghoon Lee



Sang Hoon Joo



Hyesung Park

Abstract

Two-dimensional (2D) materials are promising candidates for use in membrane applications owing to their high chemical stability, thermal stability, and outstanding mechanical strength. Especially, the graphene sandwich structure has been studied extensively as a container for well-defined 2D confined spaces. Many researchers have attempted to understand chemical reactions in confined spaces because unexpected reactions can occur owing to the nanoconfinement effect and high van der Waals (vdW) pressure. To understand chemical reactions in confined spaces, creating a well-defined 2D confined space is very important. Also, it was demonstrated that hexagonal boron nitride (h-BN) showed the highest proton conductivity than other 2D materials, and so interesting of h-BN for proton exchange membrane (PEM) has been increased. Since h-BN showed high chemical and thermal stability than conventional polymer PEM, it is important to explore application of h-BN for PEM. This paper discussed our approaches to understand organic chemical reaction in confined space of graphene sandwich and apply h-BN for proton exchange membrane.

The first part of my thesis pertains to the use of graphene sandwich nanoreactors for carrying out organic chemical reactions. Studies have observed phase transitions or hydrolysis of inorganic materials in the graphene sandwich structure, but organic chemical reactions in this structure have not been reported to date. To understand reactions in confined spaces, it is important to study organic chemical reactions in the graphene sandwich structure. I synthesized three monomers, namely dopamine, *o*-phenyldiamine (*o*PD), and 3,4-ethylene-dioxythiophene (EDOT) in a graphene sandwich. These monomers were 2D polymerized in a 2D confined space with polycrystallinity. In addition, 2D polycrystalline polydopamine exhibited reduced sheet resistance and increased bending stability and Young's modulus.

The second part pertains to the use of hexagonal boron nitride (h-BN) for fabricating proton exchange membranes. A fuel cell with a large-area single-oriented AA'-stacked trilayer h-BN were fabricated. The fuel cell with the AA'-stacked trilayer h-BN exhibited high power density of 0.66 W cm^{-1} and an open circuit voltage (OCV) of 0.958 V. The OCV degradation rate of h-BN (10% for single-layer BN and 5% for AA'-stacked trilayer h-BN) was low compared to that of Nafion (56%) in stability tests conducted under harsh condition because the h-BN blocked gas crossover and reduced generation of reactive radicals. Furthermore, I tried to fabricate new fuel cell structure for trilayer h-BN with AA'-stacking by Pt deposition in third part. To reduce costs of Pt and oxygen resistance in cathode reaction, deposition of Pt nanoparticles on trilayer h-BN with AA'-stacking were studied. By atomic layer deposition, uniform high density of Pt nanoparticles was prepared, successfully. Uniform Pt nanoparticles were used cathodes of new fuel cell based on trilayer h-BN with AA'-stacking.

Contents

Abstract

Contents

List of Figures

List of Tables

Chapter 1: Research Background for Two-Dimensional (2D) Materials Membrane.....	1
1.1 Importance of confined space in chemistry.....	1
1.2 Graphene sandwich for confined reaction.....	4
1.3 Proton conductivity of h-BN.....	7
1.3.1 Proton conductivity mechanism of h-BN.....	7
1.3.2 Proton conductivity mechanism of h-BN in aqueous solutions.....	8
1.4 h-BN for proton exchange membranes and energy applications.....	11
1.4.1 Proton conductivity through exfoliated 2D crystal.....	11
1.4.2 Chemical vapor deposition h-BN for proton exchange membranes in DMFCs.....	13
1.4.3 Chemical vapor deposition h-BN for proton exchange membranes in battery.....	15
1.5 Research objectives and approaches.....	16
1.6 References.....	17
Chapter 2: Graphene Sandwich for Confined Vessel.....	20
2.1 Introduction.....	20
2.2 Experimental process.....	22
2.2.1 Growth of graphene.....	22
2.2.2 Preparation of dopamine and oPD solutions.....	22
2.2.3 Preparation of graphene sandwich vessel containing monomers and polymerization by heating.....	23
2.2.4 Theoretical calculations.....	23
2.3 Results and discussions.....	24
2.3.1 Characterization: polymerization of dopamine in graphene sandwich vessel.....	24
2.3.2 Crystallinity of polydopamine in graphene sandwich vessel.....	27
2.3.3 Structural dependency of monomers in graphene sandwich vessel.....	33
2.3.4 Theoretical calculations.....	37
2.3.5 Effect of confined space for polymerization.....	39

2.3.6 Proposed structure of polydopamine in graphene sandwich.....	41
2.3.7 Improved sheet resistance and mechanical properties of G/polydopamine/G.....	43
2.3.8 Optical property of 2D polydopamine.....	45
2.3.7 Extraction of polydopamine from graphene sandwich.....	47
2.4 Reference.....	49
Chapter 3: h-BN for Proton Exchange Membrane in Proton Exchange Membrane Fuel Cells.....	52
3.1 Introduction.....	52
3.2 Experimental process.....	54
3.2.1 Growth of single-layer graphene.....	54
3.2.2 Growth of single-layer h-BN.....	54
3.2.3 Growth of trilayer h-BN.....	54
3.2.4 Preparation of trilayer h-BN by repeated transfer method.....	54
3.2.5 Characterization of trilayer h-BN with AA' stacking order.....	55
3.2.6 Fabrication process of fuel cells using 2D materials.....	55
3.2.7 Evaluation of fuel cells.....	56
3.3 Results and discussions.....	57
3.3.1 Fabrication of fuel cells using 2D Materials.....	59
3.3.2 Performances of fuel cell using single-layer materials.....	59
3.3.3 Performances of fuel cell using only IBL layers.....	59
3.3.4 Performances of fuel cell using trilayer h-BN; turbostratic stacking and AA'-stacking.....	59
3.3.5 Characterization of 3L-BN-transferred and AA'-stacked 3L-BN.....	60
3.3.6 Measurement of proton conductivity of performances of fuel cell using trilayer h-BN; turbostratic stacking and AA'-stacking.....	69
3.3.7 Direct methanol fuel cell application of h-BN membranes.....	69
3.3.8 Accelerated stress test (AST) for fuel cell with 2D materials.....	72
3.3.9 Comparison of before and after AST for fuel cell with 2D materials.....	74
3.4 References.....	81
Chapter 4: Pt NPs/h-BN hybrid system for cathode.....	84
4.1 Introduction.....	84
4.2 Experimental process.....	85
4.2.1 Growth of trilayer h-BN.....	85
4.2.2 Preparation of Pt on substrate by electrochemical deposition.....	85

4.2.3 Preparation of Pt on substrate by atomic layer deposition.....	85
4.2.4 Fabrication of fuel cells using 2D materials with prepared Pt nanoparticles.....	85
4.2.5 Evaluation of fuel cells.....	86
4.3 Results and disucssions.....	87
4.3.1 Pt deposition on graphene by electrochemical deposition.....	87
4.3.2 Pt deposition on SiO ₂ by atomic layer deposition.....	91
4.3.3 Characterization of Pt NPs.....	91
4.3.4 Fabrication of fuel cell based on Pt NPs/h-BN hybrid system and evaluation.....	95
4.4 References.....	98
Chapter 5: Conclusion and Future Work.....	100
5.1 Conclusion.....	100
5.2 Future work.....	102

Lists of Figures

[Chapter 1]

Figure 1.1.1 Schematic illustrations of a) 0D, b) 1D and c) 2D confined space in catalyst system.

Figure 1.2.1 Schematic illustrations of water molecule in graphene sandwich.

Figure 1.2.2 a-c) Phase transition or chemical reaction of inorganic substances in graphene sandwich.

Figure 1.3.1. Schematic illustrations of pores for a) graphene, b) monolayer hBN and c) monolayer MoS₂. The red lines indicate the pore sizes available for proton transport. Proposed aqueous proton penetration modes: d) dissociation-penetration, e) adsorption-penetration and f) H₃O⁺ penetration.

Figure 1.4.1. a) Optical photo of device for measuring proton conductivity of 2D materials. Scale bar, 1 cm. b) I–V characteristics for monolayers of h-BN, graphite and MoS₂. c) Histograms for 2D crystals used in.

Figure 1.4.2. a) Schematic illustration of a sandwich membrane consisting of a graphene film and Nafion membranes. b) MeOH concentration vs. time curve of the sandwich membrane at room temperature. c) I-V characteristics of sandwich-membrane-based passive DMFCs with 5.0 M, 10.0 M, and 15.0 M methanol solutions. d) Schematic illustration of setup of DMFCs. Maximum power densities measured at different temperatures for the e) standard MEA (SLG) and f) standard MEA (h-BN).

[Chapter 2]

Figure 2.3.1. Schematic illustration of polymerization in graphene sandwich and characterization. a) Schematic illustration of experimental process. To study solid-state reaction, we chose thermal oxidation process for polymerization of dopamine. b) XPS spectra compare G/D/G and G/PD/G. After polymerization, imine nitrogen (-N=) and pyrrolic nitrogen (-NH-) were formed, indicating cyclization of dopamine. c) To check polymerization of dopamine, G/D/G and G/PD/G were compared by UV-vis-NIR spectra. G/PD/G showed that weak absorption in range of 400 - 500 nm. By increasing amount of dopamine by immersion, clear 420 nm absorption peak was confirmed, indicating polydopamine. d) Raman spectra of G/G, G/D/G, and G/PD/G. After polymerization, dramatic reduction of I_{2D}/I_G (G band enhancement) was observed.

Figure 2.3.2. High angle annular dark field (HAADF) images of a) G/D/G and b) G/PD/G. HAADF images was distinguished by bright and dark regions. According to EDS results, amount of dopamine is larger in bright region than dark region. After polymerization, part ratio is changed. Bright region decreased from 65.83 to 48.63 % while dark region increased from 34.17 to 51.37 %. Shrinking of bright region is related to crystallization.

Figure 2.3.3. a) HR-image and b) fast fourier transform (FFT) of a) G/D/G. After heating, we measured TEM images of G/PD/G. c) HR-image, d) FFT and e) inverse FFT (IFFT) image of G/PD/G (bright) and f) HR-image, g) FFT and h) IFFT image of G/PD/G (dark)g) G/PD/G (dark) were measured. To check thickness difference of G/PD/G (bright) and G/PD/G (dark), cross-section of f) G/PD/G (bright) and i) G/PD/G (dark) were measured.

Figure 2.3.4. GI-WAXD images of a) G/D/G and b) G/PD/G. After polymerization, peaks 1 and 2 are, indicating crystalline structure. c) Linecut profile along to xy-direction and z-direction. d-spacing value could be matched with TEM results.

Figure 2.3.5. AFM data of graphene on Cu foil AFM images of a-c) graphene on Cu foil and d) its surface roughness. They show large surface roughness.

Figure 2.3.6. Polymerization of oPD and EDOT in graphene sandwich. b) Raman spectra of before and after polymerization of oPD and EDOT in graphene sandwich. Comparison of change of I_{2D}/I_G ratio of used monomers to polymers

Figure 2.3.7. XPS spectra of before and after polymerization using d) oPD and e) EDOT in sandwiched graphene. UV-vis-NIR spectra of before and after polymerization using f) oPD and g) EDOT in sandwiched graphene.

Figure 2.3.8. HR- and IFFT images of G/oPD/G, G/EDOT/G, G/PoPD/G, and G/PEDOT/G HR-images of a) before and b) after polymerization of G/oPD/G. Diffraction patterns (insets) showed that both oPD and PoPD showed ring patterns, indicating polycrystalline structure. c) IFFT image of PoPD shows 2D crystalline sheets. HR-images of d) before and e) after polymerization of G/EDOT/G. Diffraction patterns (insets) showed that PEDOT showed ring patterns, indicating polycrystalline structure. e) IFFT image of PEDOT shows small sized of crystalline domain.

Figure 2.3.9. Calculations of monomers on graphene and in graphene sandwich. a-c) monomers on graphene. Geometry and binding energy of a) dopamine, b) oPD and c) EDOT on graphene. Binding energy for each monomer is calculated in each figure. Geometry and binding energy of d) dopamine, e) oPD and f) EDOT in graphene sandwich. Binding energy for each monomer is calculated in each figure.

Figure 2.3.10. Comparison of non-sandwiched and sandwiched samples. a) XPS and b) Raman spectra of D/G and PD/G. PD/G is prepared by heating, and XPS confirmed polydopamine is successfully synthesized. TEM images and FFT of c) PD/G and d) G/PD/G. PD on graphene showed amorphous while PD in graphene sandwich showed polycrystalline characteristics.

Figure 2.3.11. High-magnified IFFT image of G/PD/G (dark). a-c) In single-layer polydopamine sheets, many five-membered rings were observed. d-f) Proposed structure of polydopamine base on each figure a-c.

Figure 2.3.12. a) Bending stability test of G/G and G/PD/G. G/PD/G maintained sheet resistance even applying high strain compared to G/G. Transmittance of G/G and G/PD/G is 95.4% and 94.84%, respectively. b) Young's modulus of G/G and G/PD/G was measured by nanoindentation test. Polydopamine enhanced Young's modulus of two-layer graphene.

Figure 2.3.13. Reflectance contrast spectra of G/G (black), PD/G (red, PD is amorphous), G/D/G (green) and G/PD/G (blue, PD is 2D polycrystalline polydopamine). Strong absorption at 600 nm is due to graphene. Strong reflectivity at 520 nm is due to 2D polycrystalline polydopamine compared to results of PD/G.

[Chapter 3]

Figure 3.3.1. Schematic illustration of fuel cells formed using 2D materials for proton exchange membrane. a), Schematic illustration of fuel cell formed using AA'-stacked 3L-BN for proton exchange membrane. b) Schematic illustration of process for fabricating fuel cells using 2D materials. Fabrication process is modified and different from general process for fabricating PEMFCs.

Figure 3.3.2. Comparison of performances for fuel cell using various 2D materials and commercial Nafion 211. a) Polarization curves, b) power density curves, and c) H_2 permeation current density results d) cyclic voltammetry (CV) for various 2D materials and Nafion 211. To obtain polarization results, fuel cells are operated at 70 °C and relative humidity 100%. H_2 gas (0.06 L min^{-1}) and air (0.246 L min^{-1}) were used as fuel and oxidant, respectively. For H_2 permeation current density measurements, H_2 gas was supplied at anode (0.2 L min^{-1}) and N_2 gas was supplied at cathode (0.075 L min^{-1}). All measurements were performed at atmospheric pressure condition.

Figure 3.3.3. Performances of fuel cell using single-layer graphene. a) polarization, b) power density, c) H_2 permeation current density, and d) CV results for fuel cell using single-layer graphene. To obtain polarization results, fuel cells are operated at 70 °C, relative humidity 100%, and atmospheric and H_2 gas (0.06 L min^{-1}) and air (0.246 L min^{-1}) was used as fuel and oxidant, respectively. For CV and H_2 permeation current density measurements, H_2 gas was supplied at anode (0.2 L min^{-1}) and N_2 gas was supplied at cathode (0.075 L min^{-1}). All measurements were done at atmospheric pressure condition.

Figure 3.3.4. Schematic illustrations of proton exchange membranes in d) 1L-BN, e) 3L-BN made by transfer repeatedly, f) AA'-stacked 3L-BN. Through defects of 1L-BN, H_2 gas crossover occurred,

corresponds to high H₂ permeation current density and low OCV of fuel cell with 1L-BN. In case of 3L-BN (transferred, turbostratic stacking), H₂ permeation current density was lowered, but current density is also lowered due to prevention of proton transport. AA'-stacking configuration does not prevent proton transport and blocks H₂ gas crossover, resulting in high OCV and low H₂ permeation current density.

Figure 3.3.5. Performances of fuel cell using only IBL (without 2D materials). a) CV curve of fuel cell using only IBL. b) H₂ permeation current density measurement indicates that considerable gas crossover occurred. Inclined feature indicates internal short circuit in fuel cell using only IBL. For CV and H₂ permeation current density measurements, H₂ gas was supplied at anode (0.2 L min⁻¹) and N₂ gas was supplied at cathode (0.075 L min⁻¹). All measurements were done at atmospheric pressure condition.

Figure 3.3.6. Characterization of trilayer BN with AA' stacking order. a) Photograph of 2 cm x 2 cm sized AA'-stacked 3L-BN transferred onto SiO₂ substrate. b) Atomic force microscope (AFM) image of AA'-stacked 3L-BN transferred onto SiO₂ substrate, indicating 1.3 nm thickness of AA'-stacked 3L-BN. Scale bar is 1 μm. c) Raman and d) UV-vis-NIR spectroscopy of AA'-stacked 3L-BN on Al₂O₃ substrate. e) Low-energy electron diffraction (LEED) pattern of single-oriented AA'-stacked 3L-BN on Al₂O₃ substrate, which was measured at 123 eV. The spots marked with red and yellow circles in zoomed-in LEED pattern correspond to h-BN and Al₂O₃, respectively. f) Transmission electron microscope top-view image of AA'-stacked 3L-BN and inset is fast Fourier transform image of AA'-stacked 3L-BN, which indicates AA' stacking order. Scale bar is 2 nm.

Figure 3.3.7. AFM images of AA'-stacked 3L-BN. 20 μm x 20 μm size AFM images of AA'-stacked 3L-BN on sapphire substrate (a and b were measured at different positions), which indicates wrinkle-free surface. Root mean square (RMS) roughness in a) and b) is 0.0913 and 0.0854 nm, respectively. c) From 10 μm x 10 μm size AFM image of AA'-stacked 3L-BN transferred onto SiO₂ substrate, indicating that AA'-stacked 3L-BN exhibits still smooth surface after transfer onto SiO₂ substrate. RMS roughness is 0.180 nm. White scale bars in (a and b) are 4 μm and black scale bar in (c) is 2 μm. d) Histogram of height distribution (surface roughness) of area 1, 2, and 3 (corresponding to a to c) measured by AFM.

Figure 3.3.8. TEM results of 3L-BN-transferred. a) High-resolution TEM top-view image and b) diffraction pattern of 3L-BN-transferred. A Moiré pattern in top-view image and diffraction pattern indicates that 3L-BN-transferred shows turbostratic stacking order. Scale bar in a) is 5 nm.

Figure 3.3.9. Schematic illustration of proton conductivity measurement system and results of proton conductivity. The resistance (R) of the membrane is measured by impedance spectroscopy. And, the proton conductivity (σ) of the membrane was calculated by using the equation, $\sigma = L/RWd$, where L is

the distance between Pt electrodes, W is the width of the membrane, and d is the thickness of the membrane.

Figure 3.3.10. Comparison of performances of DMFCs using Nafion 212 (50 μm)/Nafion 212, Nafion 212/AA'-stacked 3L-BN/Nafion 212, Nafion 212/3L-BN-transferred/Nafion 212.

Figure 3.3.11. Evolution of open circuit voltage (OCV) over time of fuel cell using AA'-stacked 3L-BN, 1L-BN, and commercial Nafion 211 during accelerated stress test (AST). AA'-stacked 3L-BN and 1L-BN shows excellent chemical stability (See red and blue arrows for degradation rate after 100 h AST) compared to Nafion 211 (See green arrow). AST was operated at 90 $^{\circ}\text{C}$, relative humidity 30%, and atmospheric pressure condition. H_2 gas (0.06 L min^{-1}) and Air (0.246 L min^{-1}) was used as fuel and oxidant, respectively.

Figure 3.3.12. a-c) Comparison of fuel cells using AA'-stacked 3L-BN, 1L-BN, and commercial Nafion 211 before and after AST. a) Polarization curves, b) power density, and c) H_2 permeation current density results for AA'-stacked 3L-BN, 1L-BN, and Nafion 211 before and after AST. Current density and power density of Nafion 211 dramatically decreased after AST (See green arrow) compared to AA'-stacked 3L-BN and 1L-BN (see red and blue arrows, respectively). From c) H_2 permeation current density results, degradation of Nafion after AST was confirmed (See change of green graph).

Figure 3.3.13. Changes in a) open circuit voltage, b) maximum power density, and c) H_2 permeation current density for each fuel cell before and after AST are described.

Figure 3.3.14. Comparison of cross-sectional SEM images of membranes using AA'-stacked 3L-BN and commercial Nafion 211 before and after AST. a-b) Cross-sectional SEM images of the MEA using the membrane based on AA'-stacked 3L-BN (IBL/ AA'-stacked 3L-BN/IBL) a) before and b) after AST. c-d) Cross-sectional SEM images of the MEA using Nafion 211 c) before and d) after AST. To measure cross-sectional SEM images, MEAs used in this work were cut by a microtome.

Figure 3.3.15. Comparison of degradation mechanism in case of Nafion and h-BN membrane at harsh condition. In case of Nafion, reactive radicals generated by gas crossover attack Nafion to break C-S bonds and sulfonated groups of Nafion. Thus, degradation and thinning of Nafion membrane were observed. Meanwhile, h-BN membrane has high thermal stability and low gas crossover. Also, it has strong B-N bonds, and so h-BN membrane withstands attack by reactive radicals. Therefore, less degradation of h-BN membrane was observed.

[Chapter 4]

Figure 4.3.1. Portion of total fuel cell costs

Figure 4.3.2. Schematic illustration of Pt NPs/h-BN hybrid system for cathode.

Figure 4.3.3. SEM images of Pt NPs on graphene by electrochemical deposition for a) 1min, b) 15 min and b) 30 min.

Figure 4.3.4. a) SEM images of Pt NPs on SiO₂ by ALD min and b) magnified image of a).

Figure 4.3.5. XPS spectra of Pt NPs on SiO₂ a) before and b) after annealing.

Figure 4.3.6. SEM images of Pt NPs on SiO₂ a) before and b) after transfer.

Figure 4.3.7. H₂ permeation current density of fuel cell based on Pt/h-BN hybrid cathode.

Lists of Tables

[Chapter 1]

Table 1. Proton and H₂ barriers for graphene and h-BN

[Chapter 3]

Table 1. OCV, current density, and H₂ permeation current density values of fuel cells based on 2D materials and Nafion 211 film.

Table 2. OCV, current density, power density, and H₂ permeation current density of fuel cells using AA'-stacked 3L-BN, 1L-BN, and Nafion 211 film: before and after 100 h of accelerated stress test.

[Chapter 4]

Table 1. ICP elemental analysis of Pt NPs on SiO₂ by ALD.

Chapter 1: Research Background for Two-Dimensional (2D) Materials Membrane

The main topic of my Ph. D is application of 2D materials membrane. Before presenting my detailed experiment results, I will introduce research backgrounds for graphene sandwich for confined reaction vessel and h-BN for proton exchange membrane. Further, I will discuss my research purpose and strategy. In section 1.1 and 1.2, importance of confined space and application of graphene sandwich will be discussed. In section 1.3 and 1.4, proton conductivity of h-BN and application of h-BN for proton exchange membrane will be introduced. Finally, purpose and strategy of the research are introduced in section 1.5.

1.1. Importance of confined space in chemistry

Over the years, many scientists have attempted to understand how chemical reactions change fundamentally when the system is confined to a narrow space of nanoscale dimensions. When molecules or substances are confined in a nanoscale space, their physicochemical properties such as reactivity, catalytic activity, and density might be altered dramatically compared to those in bulk space. This change can be attributed to the nanoconfinement effect, which occurs in confined spaces.¹ The nanoconfinement effect is often observed in advanced materials such as nanomaterials,² micro- and meso-porous materials,^{3,4} and patterned surfaces.⁵ Therefore, an understanding of the nanoconfinement effect would help one to not only understand new chemical reactions in confined spaces but also facilitate the design of advanced materials.

Increasing interest in the nanoconfinement effect has spurred discussions on the construction of confined spaces. Notably, confined environments for heterogeneous catalysts can stabilize active sites and modulate reactivity, resulting in improved catalytic performance. Chemical reactions in zero-dimensional (0D) confined spaces such as metal-organic frameworks (MOFs) and zeolites have shown enhanced catalytic activities.^{6,7} For example, theoretical studies have demonstrated that spatially changed activities of confined molecules induce the nanoconfinement effect, and this effect increases or changes the activities of confined molecules in zeolites.⁶ Moreover, new Raman spectra and fluorescence of benzylidene were observed when a benzylidene molecule was inserted inside a protein β -barrel.⁸ Single-wall carbon nanotubes (CNTs) have been fabricated as one-dimensional (1D) confined spaces. The unique Raman response of S₂ molecules in CNTs was observed through van der Waals (vdW) interactions between walls and molecules.⁹ Pan and Bao *et al.* demonstrated that confinement energy could be used to predict the catalytic properties of various transition metals

confined within CNTs.¹⁰ The nanoconfinement effect weakens substrate adsorption interactions. As a result, optimal catalytic behavior of these metals with a higher binding energy was observed. Both 0D confined spaces in zeolites or MOFs and 1D confined spaces induce changes in catalytic effects, but compositional and structural complexities make it difficult to understand such confinement for novel chemical reactions in confined spaces.

Compared to 0D and 1D confined systems, it is expected that 2D confined systems will be well-defined. 2D materials such as graphene and hexagonal boron nitride (h-BN) have been proposed as candidates for constructing 2D confined spaces. Many studies have demonstrated that molecules such as oxygen can be stable in 2D materials. For example, O₂ molecules can be intercalated between graphene and Ru (0001), and these molecules exhibit high levels of stability in confined spaces.¹¹ Furthermore, these O₂ molecules alter the electronic band structure of monolayer graphene on Ru (0001), indicating that 2D confined spaces can induce other catalytic effects. This observation led to studies on the catalytic effects of 2D materials in 2D confined spaces. Haobo Li *et al.* constructed 2D confined structures by covering graphene on the surface of Pt (111) and reported changes in its catalytic effect.¹² By covering the surface of a Pt (111) substrate with planar 2D graphene or h-BN, they induced the confinement effect on Pt (111), and this effect reduced the dissociation-adsorption energy to enhance the reactivity of the reactant. Notably, 2D confined Pt catalyst improved oxygen reduction reactions. This highlights the importance of constructing 2D confined spaces.

Types of confined spaces

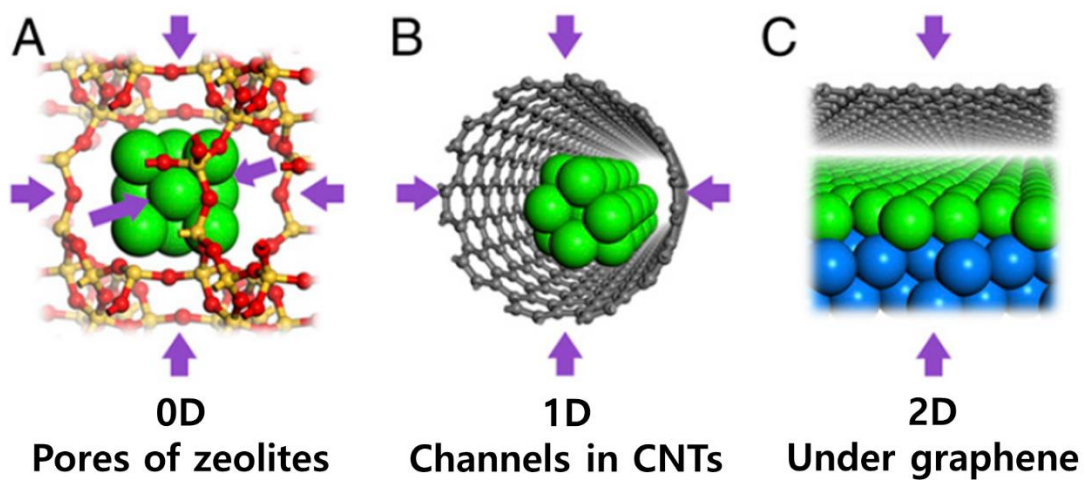


Figure 1.1.1 Schematic illustrations of a) 0D, b) 1D and c) 2D confined space in catalyst system.¹²

1.2. Graphene sandwich for confined reaction

The graphene sandwich structure, which is created by encapsulating a material between two graphene layers, is expected to be a well-defined 2D confined space. Because graphene has high mechanical strength and the ability to contain substances for reaction, the graphene sandwich structure can be used as a container for reactants in a confined space.

In 2015, Algara-Siller *et al.* observed AA stacking of water molecules in a graphene sandwich by using a transmission electron microscope (TEM, also transmission electron microscopy).¹³ Normally, AA stacking of water cannot be measured in the bulk environment at room temperature, indicating that it can be observed only in confined spaces. Moreover, they demonstrated that vdW pressure can alter the phase transition of water molecules in a graphene sandwich. The calculated vdW pressure in the graphene sandwich was around 1 GPa, and this vdW pressure induced an unexpected phase transition of water molecules in the graphene sandwich. Vasu *et al.* demonstrated that vdW pressure can induce hydrolysis reactions.¹⁴ They prepared a graphene sandwich reaction vessel containing MgCl_2 , $\text{Mg}(\text{OH})_2$, and CsI. When they measured the prepared samples by using a TEM, they confirmed the formation of MgO through hydrolysis because of high vdW pressure. Phase transition of CaSO_4 under heating was observed in a graphene sandwich containing CaSO_4 .¹⁵ CaSO_4 was placed in a graphene sandwich, and the samples thus prepared were heated. Gypsum-type CaSO_4 at room temperature transitioned to anhydrite-type CaSO_4 , as confirmed from the phase diagram. Thus far, only reactions or phase transitions of inorganic substances have been observed. However, for acquiring a comprehensive understanding of confined spaces, study for chemical reaction of organic substances in confined spaces is crucial.

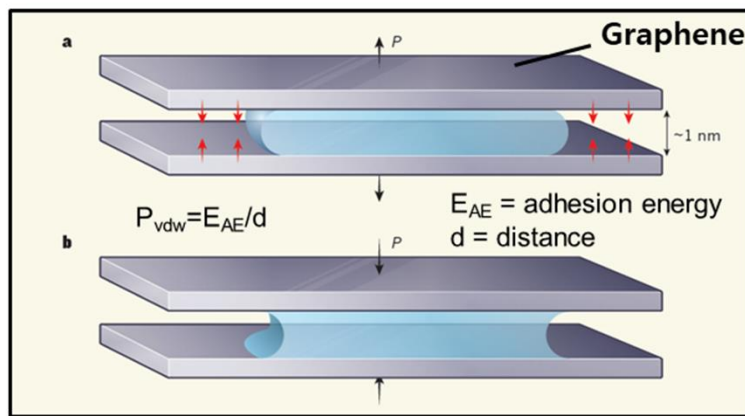


Figure 1.2.1 Schematic illustrations of water molecule in graphene sandwich.

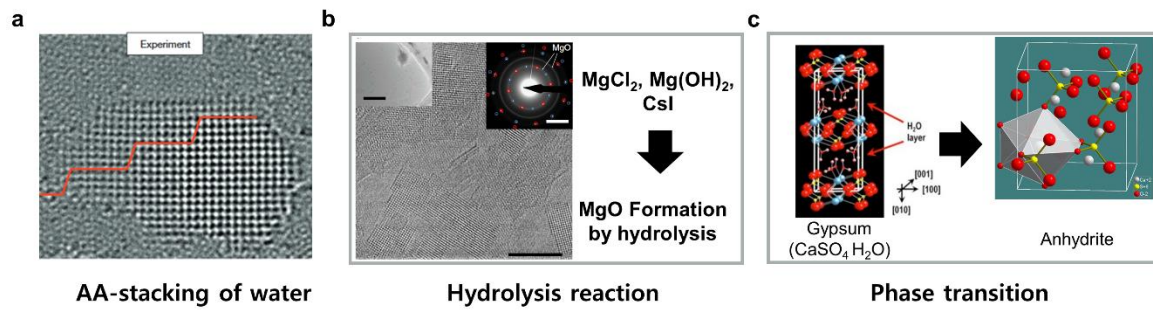


Figure 1.2.2 a-c) Phase transition or chemical reaction of inorganic substances in graphene sandwich.¹³⁻

15

1.3. Proton Conductivity of h-BN

Hexagonal boron nitride (h-BN) is an atomically thin materials, which is similar to graphene. h-BN consists of alternating boron and nitrogen atoms forming hexagonal structures and it exhibits insulating properties.^{16,17} Thus far, h-BN has been used as an alternative for SiO₂ substrates to overcome interface issues in 2D devices. In addition to studies on alternative substrates, h-BN membranes have also been investigated for their outstanding mechanical strength and proton conductivity.¹⁸⁻²² In principle, h-BN membranes are impermeable to all particles other than protons. Protons can travel through the centers of hexagonal rings in h-BN sheets while other large molecules are blocked.¹⁸⁻²⁰ In addition, it is expected that fuel cells with h-BN membranes could be operated at higher temperatures based on the high thermal stability of h-BN compared to traditional polymers. Therefore, the power density of fuel cells can be enhanced. Additionally, h-BN is a promising molecular separation membrane based on its high permeability and selectivity.²³⁻²⁶

1.3.1. Proton conductivity mechanisms of h-BN

In 2014, Geim's group demonstrated that protons can pass through the center pores of the hexagonal rings of h-BN.¹⁸ Considering the electron density of graphene, the size of the electron cloud of each carbon atom is consistent because graphene consists solely of C atoms (**Fig. 1.3.1**). The centers of the hexagonal rings of graphene are pores, where electron clouds do not exist and protons can pass through. In contrast, h-BN consists of two atoms: B and N. The electron negativity of nitrogen is much stronger than that of boron, so the electron clouds on nitrogen atoms are much larger than those on boron atoms (**Fig. 1.3.1b**). Based on the different electron negativity of boron and nitrogen atoms, the pores in h-BN have triangular shapes, unlike circular pores in graphene. When comparing the densities of electron clouds in h-BN and graphene, the electron clouds of h-BN are less dense, so the pore size of h-BN (approximately 3.0 Å²) is greater than that of graphene (approximately 2.3 Å², red lines in **Fig. 1.3.1a** and **Fig. 1.3.1b**). Therefore, it is expected that proton transport through h-BN is faster than that through graphene. MoS₂ is non-permeable because it consists of three atomic layers, and Mo and S atoms are relatively large compared to C, B, and N atoms, resulting in much denser electron clouds (red lines in **Fig. 1.3.1c**). *Ab initio* molecular dynamics simulations revealed that the estimated proton penetration barriers are approximately 1.34 and 0.7 eV for graphene and h-BN, respectively (Table 1). Furthermore, they demonstrated that the addition of Pt NPs can reduce the proton penetration barrier of h-BN to 0.5 eV. Following this research, other calculation results were also reported, which is related to penetration of proton and H atom through h-BN and other 2D materials (Table 1).²²

1.3.2. Proton conductivity mechanisms of h-BN in aqueous solutions

If 2D materials are employed as proton exchange membranes in real fuel cell, the mechanisms of proton passing in aqueous solutions should be considered. In 2017, Zhao's group reported a detailed mechanism for protons passing through 2D materials in an actual fuel cell based on discrete Fourier transform calculations.²⁷ To consider aqueous environments, they calculated the movement of hydronium (H_3O^+) on 2D materials. H_3O^+ is dissociated when it has the longest type of O-H bonds (1.5 Å) and H atoms move closest to 2D materials. Based on calculation results indicating that protons from H_3O^+ pass through 2D materials, they proposed three penetration models (**Fig. 1.3.1d** to **Fig. 1.3.1f**). i) Dissociation-penetration mode, where protons are dissociated from H_3O^+ and penetrate through the pores of 2D materials (**Fig. 1.3.1d**). Following penetration, protons combine with water molecules to form new H_3O^+ molecules. ii) Adsorption-penetration mode, where protons are dissociated from H_3O^+ and adsorbed onto 2D materials. The adsorbed protons then flip to the other side of the material (**Fig. 1.3.1e**). iii) Direct-penetration mode, where H_3O^+ penetrates 2D materials directly. Regarding direct-penetration mode, H_3O^+ ions are much larger than the pore sizes of 2D materials, so direct-penetration mode is impossible (**Fig. 1.3.1f**). Therefore, they focused on the dissociation-penetration and adsorption-penetration modes.

To investigate which penetration mode is more likely to occur qualitatively, they calculated the transformation energy barriers of H_3O^+ to protons for the adsorption mode. The transformation energies are 1.01 and 0.52 eV for graphene and h-BN, respectively. It should be noted that protons are more likely to exist in the H_3O^+ form, rather than the adsorbed form, near 2D materials. Therefore, the dissociation-penetration mode is favored over the adsorption-penetration mode for proton transport. However, the proton penetration energies of the dissociation-penetration mode are 4.31 and 3.55 eV for graphene and h-BN, respectively (Table 1), indicating that proton penetration does not occur at room temperature. However, if high thermal energy or other catalytic effects are introduced, the penetration of protons through 2D materials is possible.

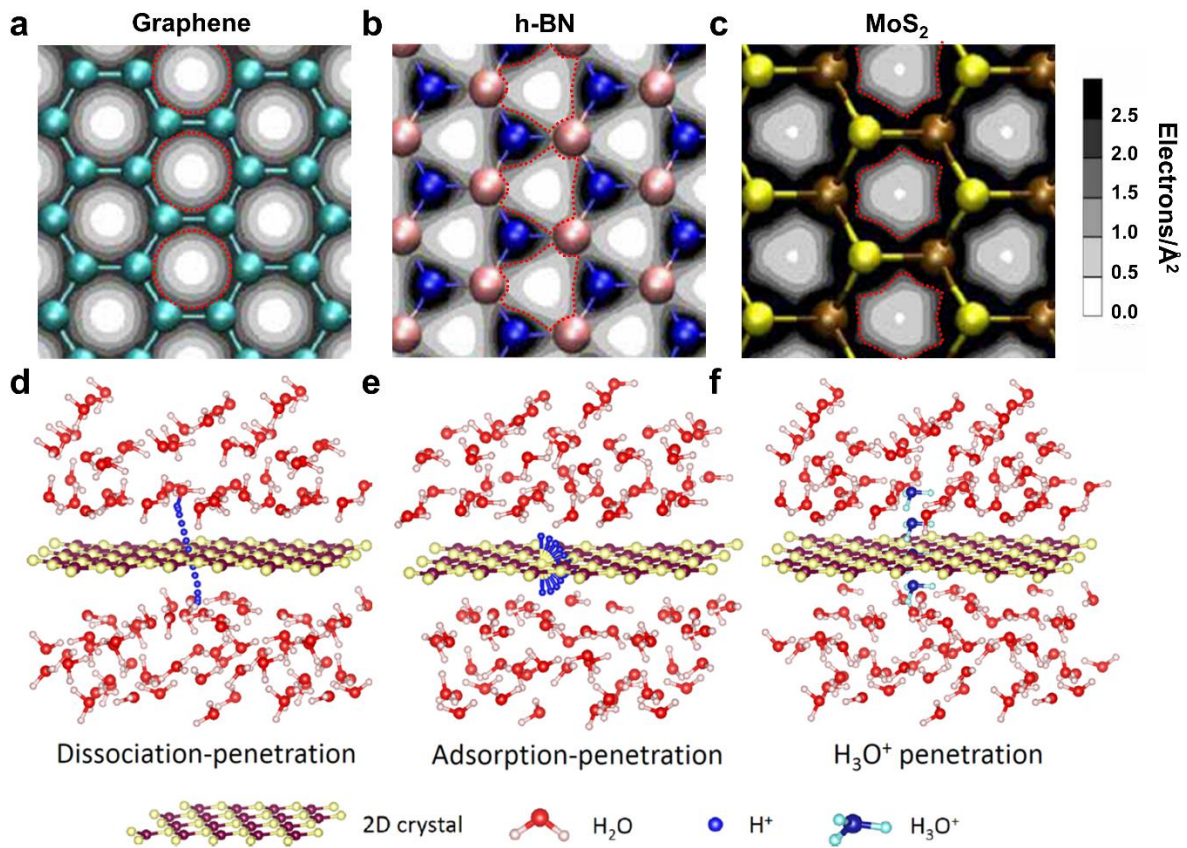


Figure 1.3.1. Schematic illustrations of pores for a) graphene, b) monolayer hBN and c) monolayer MoS₂. The red lines indicate the pore sizes available for proton transport. Proposed aqueous proton penetration modes: d) dissociation-penetration, e) adsorption-penetration and f) H₃O⁺ penetration.

Table 1. Proton and H₂ barriers for graphene and h-BN

Ref	Graphene	h-BN	
[18]	1.34 eV	0.7 eV	Proton barriers
[22]	1.56 eV	0.91 eV	Proton barriers
[27] In aqueous solution	4.31 eV	3.55 eV	Proton barriers
[27] In aqueous solution	1.01 eV	0.52 eV	Transformation energy from H ₃ O ⁺ to protons
[22]	4.61 eV	6.38 eV	Hydrogen atom barriers

1.4. h-BN for proton exchange membranes and energy applications

Based on theoretical calculations, the potential of using h-BN for proton exchange membranes has been explored by a few researchers. Regarding the feasibility of using 2D materials for proton exchange membranes, some researchers have synthesized mechanical-exfoliated 2D materials to measure their proton conductivity. They analyzed the proton conductivity of exfoliated 2D crystals experimentally. They also investigated the application of h-BN to direct methanol fuel cells (DMFCs) and vanadium redox batteries.

1.4.1 Proton conductivity through exfoliated 2D crystal

Research on the proton conductivity of 2D crystals (mechanical-exfoliated h-BN and graphene) was conducted by researchers at the University of Manchester (A.K. Geim, M. Lozada-Hidalgo, and S. Hu). In 2014, Hu *et al.* reported the proton conductivity of mechanical-exfoliated 2D crystals (monolayer h-BN, graphene, MoS₂).¹⁸ They measured the proton current I , which varies with V , where the conductance $S = I/V$. The area conductivity $\sigma = S/A$, where A is the area of the membrane. **Fig. 1.4.1** reveals that monolayer h-BN exhibits the greatest proton current (approximately 100 mS cm⁻²) among the tested 2D materials and that monolayer graphene exhibits a greater current than monolayer MoS₂. Based on the Arrhenius equation ($\sigma = \exp(-E_a / k_B T)$), they were able to obtain proton penetration barriers, where σ is proton conductivity, E_a is the proton penetration barrier, k_B is the Boltzmann constant, and T is temperature.²⁸ The proton penetration barriers are 1.2 and 0.7 eV for graphene and h-BN, respectively. These values are very similar to the results of previous theoretical calculations. Also, they measured proton selectivity during ion transport through 2D crystals.²⁹⁴ It should be noted that for perfect proton selectivity, high-quality 2D materials without vacancies or atomic defects are required.

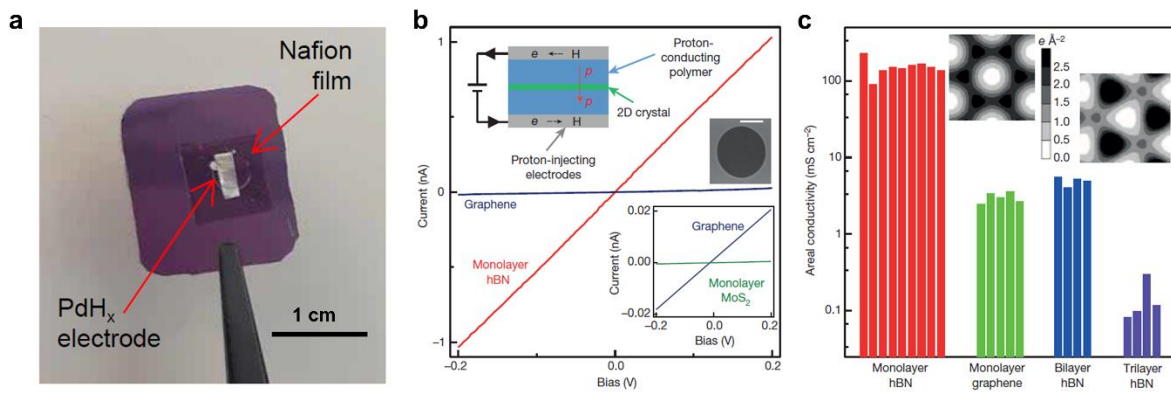


Figure 1.4.1. a) Optical photo of device for measuring proton conductivity of 2D materials. Scale bar, 1 cm. b) I–V characteristics for monolayers of h-BN, graphite and MoS₂. c) Histograms for 2D crystals used in.

1.4.2. CVD h-BN for proton exchange membranes in DMFCs

For the first real-world application of proton exchange membranes, 2D materials were employed in DMFCs as proton exchange membranes (**Fig. 1.4.2**). DMFCs are fuel cells using MeOH as a fuel and air as an oxidant. In 2016, Yan *et al.* inserted monolayer graphene between Nafion membranes to create proton exchange membranes.¹⁹ For real-world applications of proton exchange membranes, large-scale 2D materials are required. So, they employed 2D materials grown *via* CVD. When using Nafion membranes with inserted graphene, MeOH permeability decreases by 68.6% (from 1.40×10^{-6} to $0.44 \times 10^{-6} \text{ cm}^2 \text{ s}^{-1}$) with a 7% decrease in proton conductivity (0.14 to 0.12 S cm^{-1} compared to a pristine Nafion membrane). When 5% MeOH was employed as fuel, the maximum power density was 23.0 mW cm^{-2} . Holmes *et al.* also fabricated DMFCs with Nafion-2D hybrid membranes.²⁰ They employed both monolayer graphene and h-BN. Similar to the previous study, they employed CVD-grown graphene and h-BN based on requirement for large-scale materials. The open circuit voltage (OCV) value of the Nafion-2D hybrid membrane (0.668 V) was greater than that of pristine Nafion (0.625 V). Additionally, they measured MeOH permeability and found that it decreased from 3.14×10^{-6} to $2.19 \times 10^{-6} \text{ cm}^2 \text{ s}^{-1}$ when graphene was employed as a hybrid membrane. By reducing MeOH crossover, the power density of the fuel cell was enhanced. One interesting difference between graphene and h-BN lies in their temperature dependencies. The DMFC with a Nafion-graphene hybrid membrane only exhibited enhanced performance in the temperature range of $50\text{--}90 \text{ }^\circ\text{C}$, whereas the Nafion-BN hybrid membrane exhibited enhanced performance at all temperatures. This indicates that h-BN is more effective over a wider temperature range.

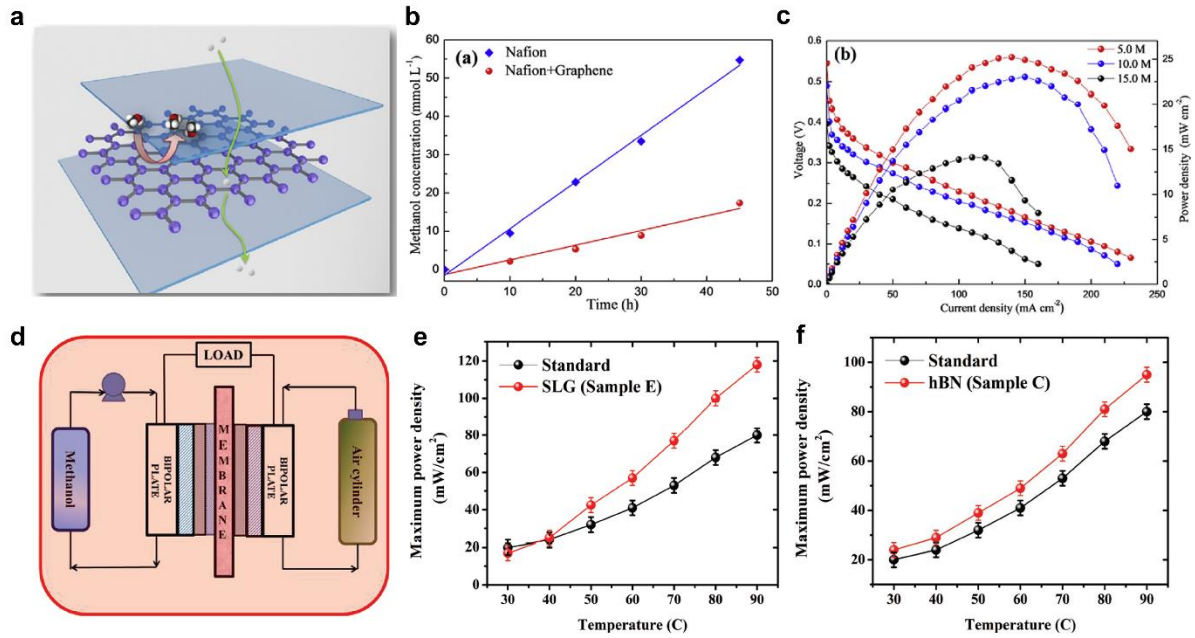


Figure 1.4.2. a) Schematic illustration of a sandwich membrane consisting of a graphene film and Nafion membranes. b) MeOH concentration vs. time curve of the sandwich membrane at room temperature. c) I-V characteristics of sandwich-membrane-based passive DMFCs with 5.0 M, 10.0 M, and 15.0 M methanol solutions. d) Schematic illustration of setup of DMFCs. Maximum power densities measured at different temperatures for the e) standard MEA (SLG) and f) standard MEA (h-BN).

1.4.3. CVD h-BN for proton exchange membranes in battery

Liu *et al.* employed h-BN to enhance the ion selectivity of sulfonated poly (ether ether ketone) (SPEEK) in vanadium ion batteries (VIBs).²¹ They created a Nafion-assisted h-BN membrane by coating Nafion onto CVD-grown h-BN directly. In SPEEK, protons can transport along water channels that are formed by sulfonated groups. However, vanadium ions can pass through SPEEK based on the large size of the water channels. An additional h-BN layer can block vanadium ions while the transport of protons is largely unaffected. They also investigated performance in terms of coulombic efficiency (CE), voltage efficiency (VE), and energy efficiency (EE). CE, which is the ratio of discharge capacity to charge capacity, increased from 92% for SPEEK to 95% for Nafion/h-BN/SPEEK at a current density of 40 mA cm⁻¹. This means that h-BN has excellent flux capabilities with blocking properties. VE, which is defined as the ratio of discharge voltage to charge voltage, was similar for all three membranes. With increasing current density, the VE of Nafion/h-BN/SPEEK decreased more based on voltage loss caused by the insulating properties of h-BN. Overall, EE, which combines CE and VE, reached 91% for Nafion/h-BN/SPEEK at a current density of 40 mA cm⁻¹, which is 4% greater than the value for SPEEK. These results indicate that the superior ion selectivity of h-BN results in enhanced performance for VIBs.

1.5. Research objectives and approaches

Graphene and h-BN have excellent mechanical strength, and they can be used to fabricate membranes. Especially, 2D confined spaces can be constructed between two graphene layers arranged in the graphene sandwich structure. An understanding of chemical reactions in 2D materials is crucial because unexpected chemical reactions or effects can be observed in confined spaces due to nanoconfinement and high vdW pressure. Thus far, only phase transitions and hydrolysis reactions of inorganic substances in confined spaces have been reported. However, for acquiring a comprehensive understanding of confined reactions, chemical reactions of organic substances in the graphene sandwich structure should be studied. In **Chapter 2**, I will describe the polymerization reaction in the graphene sandwich structure. By using the graphene sandwich structure, I observed 2D polymerization and crystallization in a confined space, which are different from those in the bulk environment.

Meanwhile, I demonstrate the feasibility of using h-BN to fabricate proton exchange membranes for use in real applications. However, a CVD h-BN membrane is used along with a commercial polymer film, where the polymer film is the primary proton exchange membrane, while the h-BN is an additional proton exchange membrane. In **Chapter 3**, I will introduce trilayer h-BN with AA'-stacking to fabricate proton exchange membranes for use in proton exchange membrane fuel cells. In this study, the primary proton exchange membrane is trilayer h-BN with AA'-stacking. Furthermore, the configuration of the trilayer h-BN with AA'-stacking reduces gas crossover effectively. Consequently, the fuel cell with the h-BN membrane exhibits outstanding thermal and chemical stability. In addition, I tried to fabricate new fuel cell structure for trilayer h-BN with AA'-stacking by Pt deposition in **Chapter 4**. To reduce costs of Pt and oxygen resistance in cathode reaction, I focused on cathode catalyst materials. So, I prepared uniform high density of Pt nanoparticles by atomic layered deposition. Uniform Pt nanoparticles were used cathodes of new fuel cell based on trilayer h-BN with AA'-stacking.

1.6. References

- (1) Chen, Y. *et al.* Insights into the effect of nanoconfinement on molecular interactions. *Nanoscale*, **2014**, *6*, 9563-9567.
- (2) Dosch, H. Some general aspects of confinement in nanomaterials. *Appl. Surf. Sci.*, **2001**, *182*, 192-195.
- (3) Kidder, M. K. *et al.* Pyrolysis of mesoporous silica-immobilized 1,3-diphenylpropane. impact of pore confinement and size. *J. Am. Chem. Soc.*, **2005**, *127*, 17.
- (4) Wolkin, M. V. *et al.* Electronic states and luminescence in porous silicon quantum dots: The role of oxygen. *Phys. Rev. Lett.*, **1999**, *82*, 197.
- (5) Crommie, M. F.; Lutz, C. P. and Eigler, D. M., Confinement of electrons to quantum corrals on a metal surface. *Science*, **2012**, *262*, 218-220.
- (6) Sastre, G. and Corma, A. The confinement effect in zeolites. *J. Mol. Catal. Chem.*, **2009**, *305*, 3-7.
- (7) Zhao, M. *et al.*, Metal-organic frameworks as selectivity regulators for hydrogenation reactions. *Nature*, **2016**, *539*, 76-80.
- (8) Williams, D. E. *et al.* Mimic of the green fluorescent protein β -barrel: photophysics and dynamics of confined chromophores defined by a rigid porous scaffold. *J. Am. Chem. Soc.*, **2015**, *137*, 2223–2226.
- (9) Li, G. *et al.*, Giant raman response to the encapsulation of sulfur in narrow diameter single-walled carbon nanotubes. *J. Am. Chem. Soc.*, **2016**, *138*, 40-43.
- (10) Xiao, J.; Pan, X.; Guo, S.; Ren, P. and Bao, X. Toward fundamentals of confined catalysis in carbon nanotubes. *J. Am. Chem. Soc.*, **2015**, *137*, 477-482.
- (11) Shutter, P.; Sadowski, J. T. and Shutter, E. A. Chemistry under Cover: tuning metal–graphene interaction by reactive intercalation. *J. Am. Chem. Soc.*, **2010**, *132*, 8175-8179.
- (12) Li, H.; Xiao, J.; Fu, Q. and Bao, X. Confined catalyst under two-dimensional materials. *Proc. Natl. Acad. Sci. USA*, **2017**, *111*, 17023-17028.
- (13) Algara-Siller, G. *et al.* Square ice in graphene nanocapillaries *Nature*, **2015**, *519*, 443-446.

- (14) Vasu, K. S. *et al.*, van der Waals pressure and its effect on trapped interlayer molecules. *Nat. Commun.*, **2016**, *7*, 12168.
- (15) Lehnert, T. *et al.* *In situ* crystallization of the insoluble anhydrite AII phase in graphene pockets. *ACS Nano*, **2017**, *11*, 7967-7973.
- (16) Britnell, L. *et al.* Electron tunneling through ultrathin boron nitride crystalline barriers. *Nano Lett.*, **2012**, *12*, 1707-1710.
- (17) Goldberg, D. *et al.* Boron nitride nanotubes and nanosheets. *ACS Nano*, **2010**, *4*, 2979-2993.
- (18) Hu, S. *et al.* Proton transport through one-atomic-thick crystals. *Nature*, **2014**, *516*, 227-230.
- (19) Yan, X. *et al.* A monolayer graphene – nafion sandwich membrane for direct methanol fuel cells. *J. Power Sources*, **2016**, *311*, 188-194.
- (20) Holmes, S. *et al.* 2D crystals significantly enhance the performance of a working fuel cell. *Adv. Energy Mater.* **2017**, *7*, 1601216.
- (21) Liu, J. *et al.* Sandwiching h-BN monolayer films between sulfonated poly(ether ether ketone) and nafion for proton exchange membranes with improved ion selectivity. *ACS Nano*, **2019**, *13*, 2094-2102.
- (22) Seel, M. and Pandey, R. Proton and hydrogen transport through two-dimensional monolayers. *2D Mater.*, **2016**, *3*, 025004
- (23) Chen, C. *et al.* Functionalized boron nitride membranes with ultrafast solvent transport performance for molecular separation. *Nat. Commun.*, **2018**, *9*, 1902.
- (24) Zhang, Y. *et al.* Hexagonal boron nitride with designed nanopores as a high-efficiency membrane for separating gaseous hydrogen from methane. *J. Phys. Chem. C*, **2015**, *119*, 19826-19831
- (25) Ganji, M. D. and Dodangeh, R. Hydrogen purification performance of a nanoporous hexagonal boron nitride membrane: molecular dynamics and first-principle simulations. *Phys. Chem. Chem. Phys.*, **2017**, *19*, 12032-12044.
- (26) Zhou, S. *et al.* Nanoporous boron nitride membranes for helium separations. *ACS Appl. Nano Mater.*, **2019**, *2*, 4471-4479.
- (27) Shi, L.; Xu, A.; Chen, G. and Zhao, T. Theoretical understanding of mechanisms of proton exchange membranes made of 2D crystals with ultrahigh selectivity. *J. Phys. Chem. Lett.*, **2017**, *8*, 4354-4361.

(28) Miao, M.; Nardelli, M. B.; Wang, Q. and Liu, Y. First principles study of the permeability of graphene to hydrogen atoms. *Phys. Chem. Chem. Phys.*, **2013**, *15*, 16132-16137.

(29) Lozada-Hidalgo, M. *et al.* Sieving hydrogen isotopes through two-dimensional crystals. *Science*, **2016**, *351*, 68-70.

Part 2: Graphene Sandwich for Confined Vessel

2.1. Introduction

Thus far, many attempts have been made to understand chemical reactions in confined spaces. In a confined space, unexpected reactions can occur, and the reactivity of molecules could increase owing to the nanoconfinement effect, which is different from the behavior of molecules in bulk space.^{1,2} Thus, many scientists have shown interest in utilizing confined spaces for carrying out chemical reactions. Theoretical studies have demonstrated that a confined space increases molecular orbital energies and changes molecular activity in 0D zeolites.³ Moreover, experimental reports revealed that carbon nanotubes (CNTs) affect catalytic effects strongly.⁴ Even though zeolites and CNTs exhibit catalytic effects in confined spaces for 0D and 1D materials, 0D and 1D confined spaces are structurally complex, and therefore, it is difficult to understand the nanoconfinement effect. Compared with 0D and 1D confined spaces, 2D confined spaces have considerably superior structural definition. Haobo Li *et al.* constructed a 2D confined structure by covering graphene on the surface of Pt (111), and they observed a change in its catalytic effect.² By covering Pt (111) with planar 2D graphene or h-BN, they induced the confinement effect on Pt (111), which reduced the dissociation-adsorption energy required to enhance the reactivity of the reactant. Notably, the 2D-confined Pt catalyst improved oxygen reduction reactions.

Recent studies have demonstrated that the graphene sandwich structure can be used as a reaction vessel to construct 2D confined structures. Generally, the graphene sandwich structure has been used as a liquid cell in TEM because of its high transparency and thermal conductivity, which help minimize damage due to electron beams and, thus, facilitate observations of metal nanoparticles or biological samples.⁵⁻¹³ Furthermore, it has been demonstrated that the graphene sandwich structure can be used as a high-pressure reaction vessel, where the vdW pressure has been predicted experimentally to be around 1.2 GPa.¹² In such high-vdW-pressure-induced chemical reactions, where metal salts are converted into metal oxides by hydrolysis, phase transitions of water and inorganic salt crystals that cannot occur at atmospheric pressure have been observed.¹¹⁻¹³ Thus far, hydrolysis and phase transition of inorganic chemical reactions have been reported, but there is no report of organic chemical reactions in the graphene sandwich structure. From the viewpoint of basic chemistry, it is crucial to investigate and reveal monomer polymerization in the graphene sandwich structure under the nanoconfinement effect and high vdW pressure.

Herein, we prepared graphene sandwich vessels containing monomers such as dopamine, o-phenylenediamine (oPD), and ethylenedioxythiophene (EDOT) by spin-coating each on bottom

graphene and transferring top graphene on top of it. Prepared monomers are oxidative-polymerized by heating. During oxidative polymerization, it is observed that these monomers, which are usually polymerized in amorphous and linear form in bulk space, are 2D polymerized in confined space with polycrystallinity. Transmission electron microscopy (TEM) studies and Grazing-incidence wide X-ray angle diffraction (GI-WAXD) demonstrated that polymers in confined space exhibited polycrystalline characteristics. By removing graphene signal, thin polydopamine with many five membered rings was observed. Theoretical calculation supported polymerization and crystallization in graphene sandwich because of high vdW pressure. 2D polycrystalline polydopamine exhibited reduced sheet resistance. As polydopamine is a well-known adhesive, G/PD/G shows much improved mechanical property compared to G/G in bending stability and nanoindentation for Young's modulus. It indicates that this method enhances mechanical properties of graphene without any loss of its sheet resistance.

2.2 Experimental Process

2.2.1. Growth of graphene

Single-layer graphene was grown on Cu foil (99.8 % purity, 0.025 mm thick, Alfa Aesar) via low-pressure chemical vapor deposition (LP-CVD) method. Cu foil was placed at the center of quartz CVD furnace, and the furnace was heated to 1000 °C in flow of H₂ gas 10 sccm. The Cu foil was pre-annealed at 1000 for 30 minutes. After growth time for 30 minutes, the furnace was cooled down to room temperature, quickly.

2.2.2. Preparation of dopamine and oPD solutions

Dopamine hydrochloride (Sigma Aldrich, 98%) is dissolved into deionized (DI) water (2 mg ml⁻¹), and prepared solution is ultra-sonicated for 5 min. For preventing self-polymerization of dopamine solution, pH of dopamine solution is set to 3.8 by adding 20 µl of 0.1 M hydrochloride solution. oPD is also dissolved into DI water to make oPD solution (0.1 M).

2.2.3. Preparation of graphene sandwich vessel containing monomers and polymerization by heating

Prepared monomer solutions (dopamine, oPD, EDOT) are spin-coated onto CVD-grown graphene (G) on Cu foil to get monomers/G/Cu. At the same time, poly(methyl methacrylate)(PMMA) is spin-coated onto another graphene on Cu foil, and Cu foil is etched away by using ammonium persulfate (APS) solution to get PMMA/G. PMMA/G is rinsed by DI-water, and PMMA/G is transferred onto monomers/G/Cu foil to get PMMA/G/monomers/G/Cu foil. Cu foil of prepared sample (PMMA/G/monomers/G/Cu foil) is etched away again by APS solution, and PMMA/G/monomers/G is transferred onto SiO₂ substrate. Using acetone, PMMA is removed, and we get G/monomers/G/SiO₂. G/monomers/G/SiO₂ is polymerized by heating on hot plate (180 for 3hr), and G/polymers/G/SiO₂ is successfully prepared.

2.2.4. Theoretical calculations

DFT calculations were performed *via* the Vienna Ab Initio Simulation Package. The interaction between valence electrons and ion cores was described by the projected augmented wave method. Generalized gradient approximation was adopted for the exchange-correlation functional. The DFT-D2 method was used to describe the weak van der Waals interaction in the system. An energy cutoff of 400 eV was used for the plane wave basis. All structures were relaxed until the force on each atom converged to 0.01 eV Å⁻¹ and the energy converged to 1×10^{-4} eV. The size of the unit cell was $22.14 \times 22.14 \times$

20 \AA^3 , and k-point mesh was sampled by $2 \times 2 \times 2$. The single layer graphene consisted of 162 carbon atoms.

2.3 Results and discussions

2.3.1. Characterization: polymerization of dopamine in graphene sandwich vessel

Polymerization of dopamine in a graphene sandwich vessel is illustrated schematically in **Fig. 2.3.1a**. A thin film of dopamine on graphene was prepared by spin-coating a dopamine solution (1 mg mL^{-1}).¹⁵ The pH of the dopamine solution was adjusted to 4.0 or lower to suppress self-polymerization.¹⁶⁻¹⁸ Thereafter, another graphene layer was transferred onto the dopamine/graphene layer to create a graphene sandwich vessel containing dopamine (graphene/dopamine/graphene, G/D/G). Graphene/polydopamine/graphene (G/PD/G) was fabricated by heating G/D/G at $180 \text{ }^\circ\text{C}$ for 3 h.¹⁹ Normally, dopamine is polymerized in a basic solution (pH 8.5) by accelerating its oxidation to obtain the polydopamine structure, which is called bulk polydopamine in this paper. Although the exact structure of bulk polydopamine has not been elucidated, it is known to be an amorphous polymer with a linear form, and it has a randomly distributed structure consisting of three components, namely dopamine, 5,6-dihydroxyindole, and leukodopamine-chrome.^{15,17,18}

The results of X-ray photoelectron spectroscopy (XPS) in **Fig. 2.3.1b** indicate that the dopamine in the graphene sandwich changed to polydopamine. To understand the XPS spectrum of the polydopamine in the graphene sandwich, one should consider the TEM and grazing incidence wide-angle X-ray diffraction (GI-WAXD) results together. TEM and GI-WAXD indicated that the polydopamine in the graphene sandwich was 2D and polycrystalline. Considering the XPS, TEM, and GI-WAXD data, the XPS peaks of the 2D polycrystalline polydopamine in the graphene sandwich correspond to the amine group (399.7 eV , 19.80%, originated from graphitic N), -NH- group (400.3 eV , 16.74%, originated from pyrrolic N), and -N= group (398.5 eV , 63.44%, originated from pyridinic N), exhibiting cyclization and polymerization of dopamine.²⁰⁻²² This result is different from that of bulk polydopamine, which exhibits linear and amorphous characteristics. The XPS peaks of bulk polydopamine correspond to the amine group (399.7 eV , 31.36%, originated from dopamine), -NH- group (400.3 eV , 30.34%, originated from leukodopaminechrome), and -N= group (398.5 eV , 38.30%, originated from 5,6-dihydroxyindole). Bulk polydopamine powder was prepared according to the following method. Dopamine was polymerized to polydopamine by setting the pH level to 8, and the resulting product was evaporated in oven at 70°C for one day to obtain polydopamine in powder form. Since there is difference in the synthetic environments of confined and bulk spaces, the corresponding XPS results are different as well. Meanwhile, I prepared polydopamine on graphene and on SiO_2 by following the same method. Repeated units of polydopamine on graphene were similar to the polydopamine in the graphene sandwich, consisting of 23.03% of the amine group, 16.00% of the -NH- group, and 60.97% of the -N= group. In the case of polydopamine on SiO_2 , an increase in only the full

width at half maximum (FWHM) of the peaks was observed, indicating that the polymerization of polydopamine through heating was difficult without graphene. The ultraviolet visible near infrared (UV-vis-NIR) spectra indicated the formation of polydopamine in the graphene sandwich (**Fig. 2.3.1c**). G/D/G was polymerized to G/PD/G upon heating. G/PD/G (blue graph in **Fig. 2.3.1c**) exhibited weak absorption in the wavelength range of 400–500 nm, which corresponds to the result obtained for polydopamine in a previous study.¹⁷

To examine polydopamine in the graphene sandwich, Raman spectroscopy was used (**Fig. 2.3.1d**). Graphene/graphene (G/G, red curve in **Fig. 2.3.1d**, $I_{2D}/I_G = 2.84$) exhibited a turbostratic stacked graphene Raman feature.^{23,24} When dopamine was inserted into the graphene sandwich vessel, I_{2D}/I_G decreased slightly to 1.76 (blue curve in **Fig. 2.3.1d**). The aromatic ring in dopamine and the graphene interacted with each other through a strong π - π interaction, resulting in a slight decrease in I_{2D}/I_G .^{25,26} Interestingly, I_{2D}/I_G decreased significantly to 0.56 after the polymerization of dopamine (green graph in **Fig. 2.3.1d**). This dramatic reduction in I_{2D}/I_G (dramatic enhancement of the G band) can be explained using the zone-folding effect through superlattice formation. Because of superlattice formation, the M point of graphene was folded to the Γ point or the K point.^{27,28} When energy of the excitation laser was close to the energy separation between the π and π^* bands around the folded M point, strong optical absorption occurred, leading to a dramatic increase in the intensity of the G band. As mentioned earlier, the dopamine in the graphene sandwich was polymerized with 2D and polycrystalline characteristics. The resulting 2D-polycrystalline polydopamine and the top and bottom graphene layers formed a superlattice in the graphene sandwich vessel system, resulting in enhancement of the G band. Polycrystalline polydopamine will be discussed in depth in the TEM study part. The Raman spectra (range of 1000–1500 cm^{-1}) of G/Polymer/G was more pronounced compared to that of G/G or G/monomer/G. This feature is related to the Raman mode for rotation mismatch, called R and R' at 1360–1520 and 1580–1620 cm^{-1} , respectively, which originated from rotation mismatch between the crystalline polymer and graphene in the experiment. Their frequencies depend on the rotation angle due to the superlattice-activated Raman process.²⁹ The diffraction pattern showed many different rotation angles between crystalline polymer and graphene, and as a result, the R and R' bands were broad.

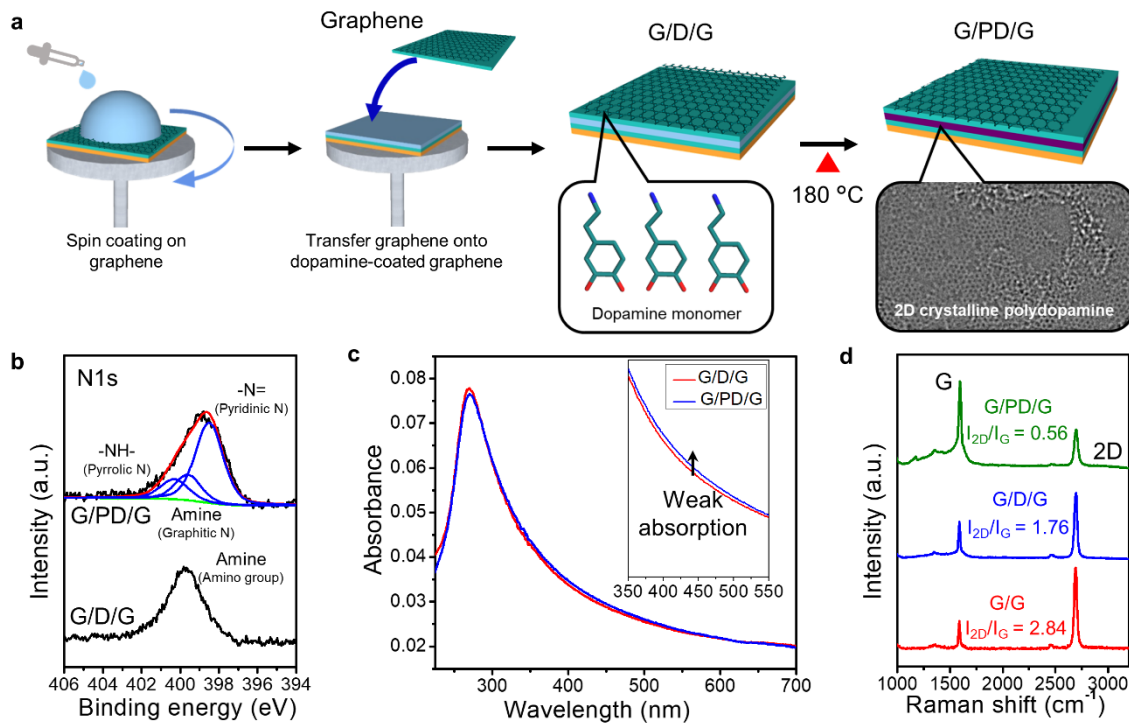


Figure 2.3.1. Schematic illustration of polymerization in graphene sandwich and characterization. a) Schematic illustration of experimental process. To study solid-state reaction, we chose thermal oxidation process for polymerization of dopamine. b) XPS spectra compare G/D/G and G/PD/G. After polymerization, imine nitrogen (-N=) and pyrrolic nitrogen (-NH-) were formed, indicating cyclization of dopamine. c) To check polymerization of dopamine, G/D/G and G/PD/G were compared by UV-vis-NIR spectra. G/PD/G showed that weak absorption in range of 400 - 500 nm. By increasing amount of dopamine by immersion, clear 420 nm absorption peak was confirmed, indicating polydopamine. d) Raman spectra of G/G, G/D/G, and G/PD/G. After polymerization, dramatic reduction of I_{2D}/I_G (G band enhancement) was observed.

2.3.2. Crystallinity of polydopamine in graphene sandwich vessel

Transmission electron microscopy (TEM) was used to evaluate the crystal structure of polydopamine in the graphene sandwich vessel at the atomic resolution (**Fig. 2.3.2** and **Fig. 2.3.3**). The high-angle annular dark field image of G/D/G contains distinct bright and dark regions (**Figs. 2.3.2a** and **2.3.2b**). The bright and dark regions indicate thin and thick regions of the dopamine layer (or polydopamine), respectively. After polymerization, the hole shown in **Fig. 2.3.2a** was measured. A comparison of the images before and after polymerization indicated that the size of the dark region increased from 34.17% to 51.37% while that of the bright region decreased from 65.83% to 48.63% after polymerization. Shrinkage of the bright region was ascribed to the is crystallization of polydopamine.

To analyze atomic images and crystal structures, high-resolution (HR) TEM images were acquired (**Fig. 2.3.3**). The dopamine in the graphene sandwich may not have been well aligned, because of which it did not considerably affect the moiré patterns of the two-layer graphene structure (**Figs. 2.3.3a** and **2.3.3b**). After polymerization, different moiré patterns were observed compared to those of G/D/G (**Figs. 2.3.3c** and **2.3.3f**). Notably, the stacking angles of two-layer graphene in the diffraction patterns before and after polymerization were different because I could not perform measurements from the same position. Regardless of the stacking angle, the fast Fourier transforms (FFT) of G/PD/G (bright) and G/PD/G (dark) exhibited that ring patterns were formed after polymerization (**Figs. 2.3.3d** and **2.3.3g**), suggesting that polycrystalline structures were formed. The d-spacing values of the first and second ring patterns were 2.2 Å and 1.4 Å, respectively, which correspond to the (0-110) and (1-210) planes in the benzene ring.³⁰ To obtain clear information about the polycrystalline structure, I removed the graphene signal from the HR-images of G/PD/G by using inverse FFT (IFFT) methods. In the resulting IFFT images, clear 2D crystalline sheets were observed in the dark and bright regions of G/PD/G (**Figs. 2.3.3e** and **2.3.3h**). The polycrystallinity of polydopamine indicated the existence of considerable rotation mismatch between the polymer and graphene layers, which is consistent with the broad R and R' bands obtained in the Raman results. Furthermore, 2D polydopamine formed superlattices with the top and bottom graphene layers, and it induced G band enhancement in the Raman spectra through the zone-folding effect. Moreover, the amount of polydopamine in the bright region was confirmed to be greater than that in the dark region. A cross-sectional image of PD (bright) indicated the presence of 3–5 polydopamine layers in the bright region (**Fig. 2.3.3i**). Top-view and cross-sectional images of PD (dark) revealed the existence of a single polydopamine layer in the dark region (**Fig. 2.3.3j**). Thus, I successfully observed single-layer 2D polycrystalline polydopamine in the dark region.

To check crystallinity of the above polymers at a large scale, I measured their diffraction patterns by using GI-WAXD (**Fig. 2.3.4**). To carry out GI-WAXD measurements, G/D/G and G/PD/G were

prepared on Cu foils. New peaks 1 and 2 were observed after polymerization. Peak 1 represents the xy-direction diffraction peak (d value of peak a is 2.4 Å), and it is slightly larger than that in the diffraction pattern (2.2 Å) obtained using TEM. Because the ring pattern obtained using TEM is relatively broad, d-spacing along the xy-direction would be close to 2.4 Å. Peak 2 represents the z-direction peak (d value of peak b, 3.69 Å), and its value is similar to that in the cross-sectional TEM images (3.5 Å). Peaks 1 and 2 are shown as ring patterns, indicating the formation of crystallites at various possible orientations with respect to the xyz directions. The samples were prepared on Cu foil, and its surface roughness was very high. Owing to this high surface roughness, crystallization was measured at various orientations (**Fig. 2.3.5**).

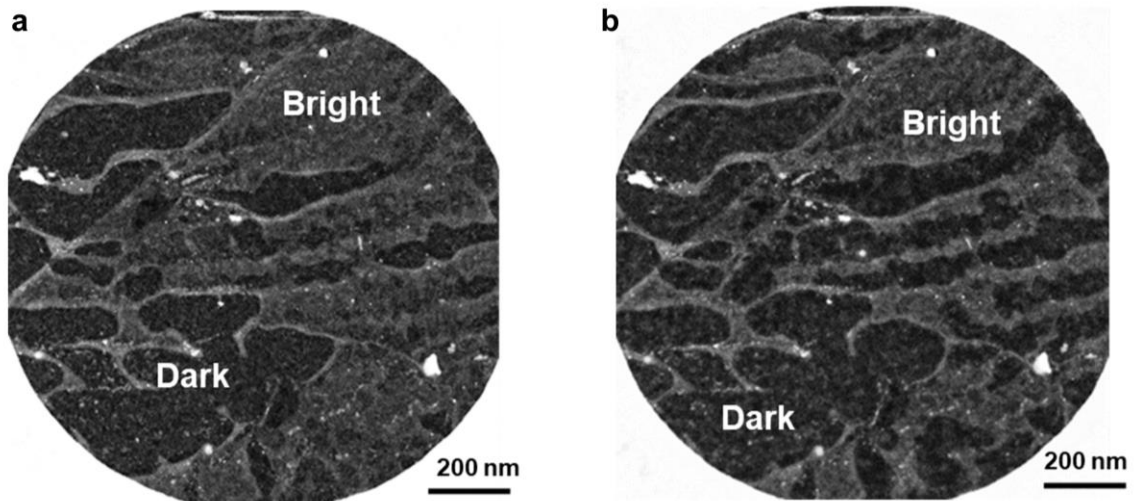


Figure 2.3.2. High angle annular dark field (HAADF) images of a) G/D/G and b) G/PD/G. HAADF images was distinguished by bright and dark regions. According to EDS results, amount of dopamine is larger in bright region than dark region. After polymerization, part ratio is changed. Bright region decreased from 65.83 to 48.63 % while dark region increased from 34.17 to 51.37 %. Shrinking of bright region is related to crystallization.

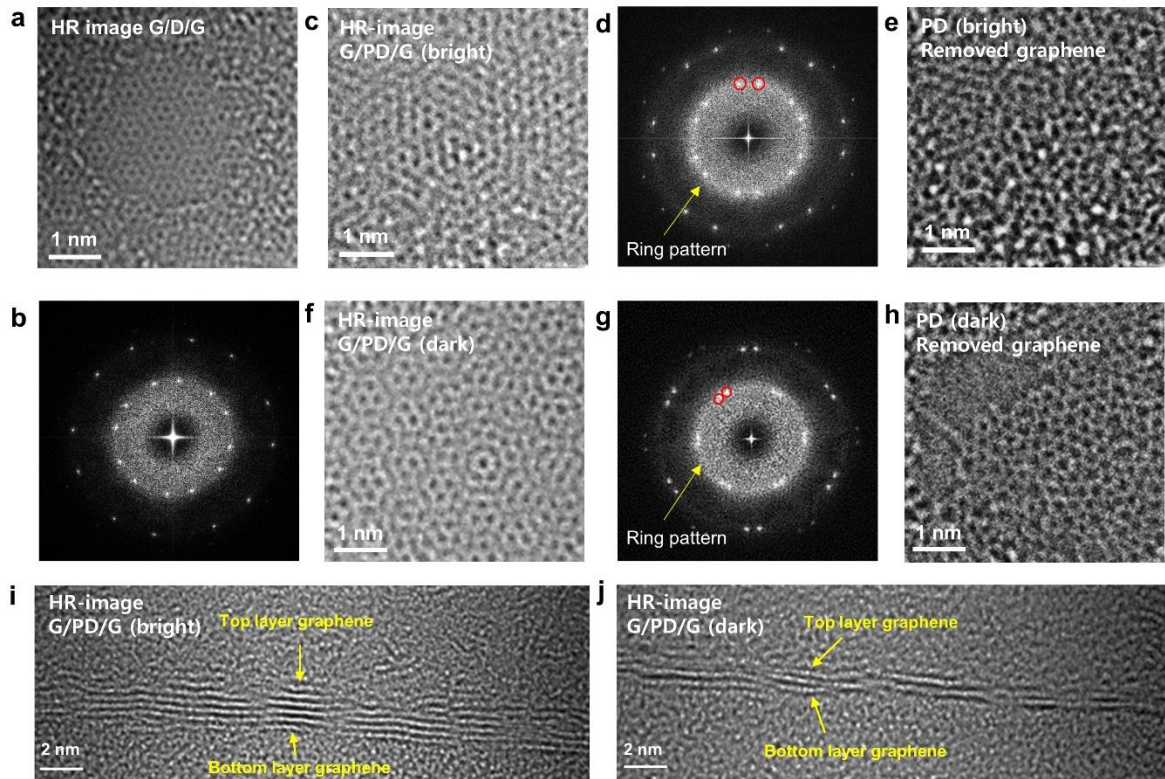


Figure 2.3.3. a) HR-image and b) fast fourier transform (FFT) of a) G/D/G. After heating, we measured TEM images of G/PD/G. c) HR-image, d) FFT and e) inverse FFT (IFFT) image of G/PD/G (bright) and f) HR-image, g) FFT and h) IFFT image of G/PD/G (dark)g) G/PD/G (dark) were measured. To check thickness difference of G/PD/G (bright) and G/PD/G (dark), cross-section of f) G/PD/G (bright) and i) G/PD/G (dark) were measured.

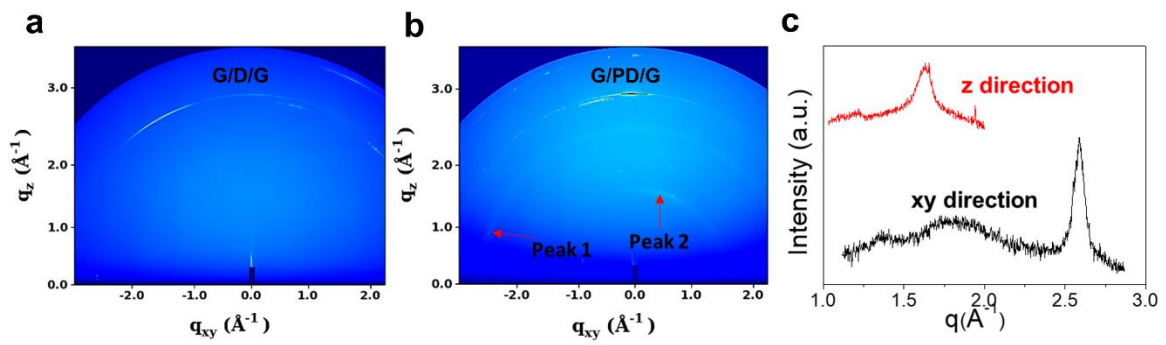


Figure 2.3.4. GI-WAXD images of a) G/D/G and b) G/PD/G. After polymerization, peaks 1 and 2 are, indicating crystalline structure. c) Linecut profile along to xy-direction and z-direction. d-spacing value could be matched with TEM results.

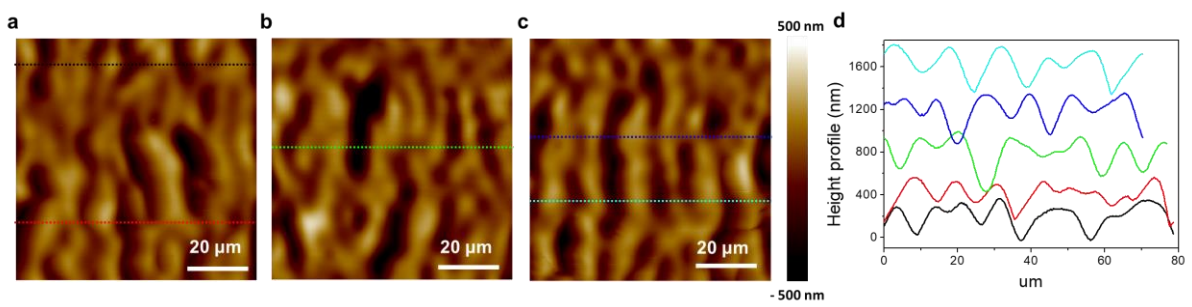


Figure 2.3.5. AFM data of graphene on Cu foil AFM images of a-c) graphene on Cu foil and d) its surface roughness. They showed large surface roughness.

2.3.3. Structural dependency of monomers in graphene sandwich vessel

To investigate the relationship between the types of monomers used in the graphene sandwich vessel, I prepared other monomers, namely oPD and EDOT. oPD is a six-membered ring monomer, albeit considerably more planar than dopamine. EDOT is five-membered ring and planar monomer, which is different from the six-membered ring monomers of dopamine and oPD. Both oPD and EDOT can be polymerized by oxidative polymerization (**Fig. 2.3.6a**). I prepared graphene sandwich structures containing oPD and EDOT and polymerized oPD and EDOT in the graphene sandwich structures through heating; the occurrence of polymerization was confirmed with XPS and UV-vis-NIR (**Fig. 2.3.7**). After heating, similar Raman spectra as those of oPD and EDOT were obtained (**Figs. 2.3.6b and 2.3.6c**). Comparing the changes in I_{2D}/I_G , the reduction in I_{2D}/I_G was the largest in the case of oPD to Poly(oPD) (1.32 to 0.52) than those in the cases of D to PD (1.75 to 0.56) and EDOT to PEDOT (2.44 to 1.12). The more planar oPD interacted more strongly between the two graphene layers, and therefore, reduction of its I_{2D}/I_G was the largest among the monomers used herein. By contrast, given that PEDOT is a five-membered ring monomer, its interaction with graphene was considerably weaker than those of dopamine and oPD, and therefore, the reduction in its I_{2D}/I_G was lesser. This expectation of structural dependency was demonstrated in cases of the monomer samples as well. Because the interaction between graphene and oPD was the strongest owing to the six-membered ring and planar structure of oPD, I_{2D}/I_G of G/oPD/G (1.32) decreased by a considerably greater extent than those of G/D/G (1.75) and G/EDOT/G (2.44).

To evaluate this expectation, I obtained TEM images of G/oPD/G, G/PoPD/G, G/EDOT/G, and G/PEDOT/G. Surprisingly, I observed ring patterns of FFT in the HR images of G/oPD/G (before heating), indicating that it exhibited polycrystalline characteristics owing to the strongest interaction between oPD and two graphene layers, even when it was not heated. After G/oPD/G was heated, a ring pattern was observed in the FFT of the HR image of G/PoPD/G, and 2D polycrystalline PoPD was successfully confirmed by means of IFFT analysis (**Fig. 2.3.7**). Two-dimensional polycrystalline PEDOT was observed in the TEM images, but the domain size of PEDOT was relatively small compared to those of other polymers. Because of the small domain size, R and R' bands were not pronounced, and I_{2D}/I_G decreased to a smaller extent than those of other polymers.

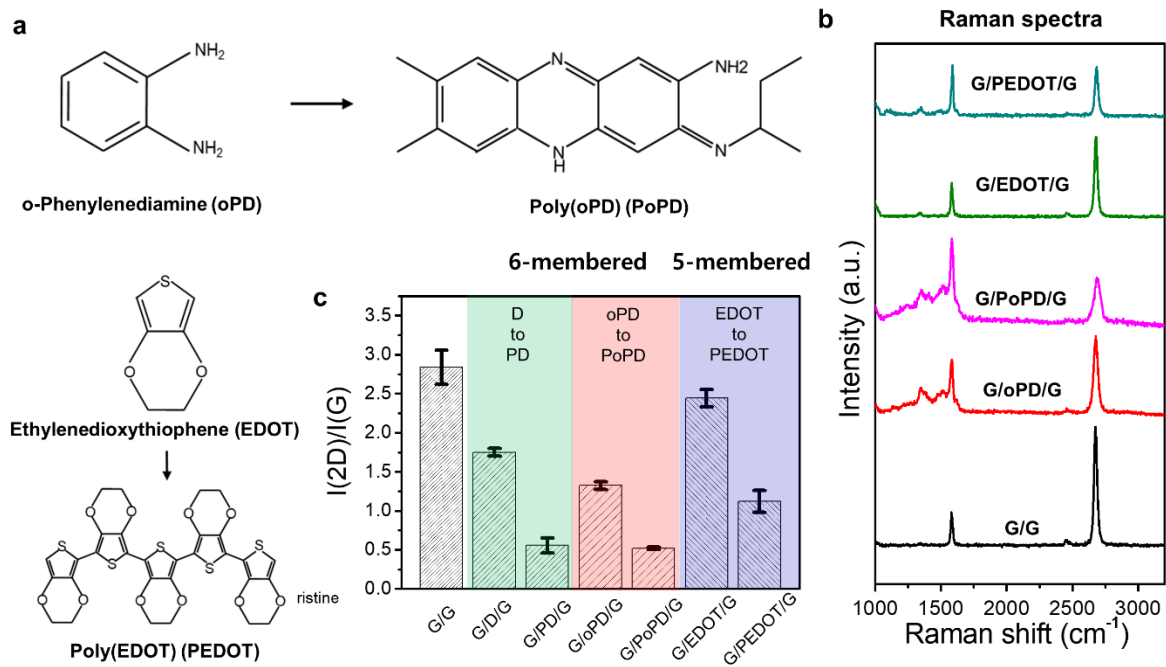


Figure 2.3.6. Polymerization of oPD and EDOT in graphene sandwich. b) Raman spectra of before and after polymerization of oPD and EDOT in graphene sandwich. Comparison of change of I_{2D}/I_G ratio of used monomers to polymers

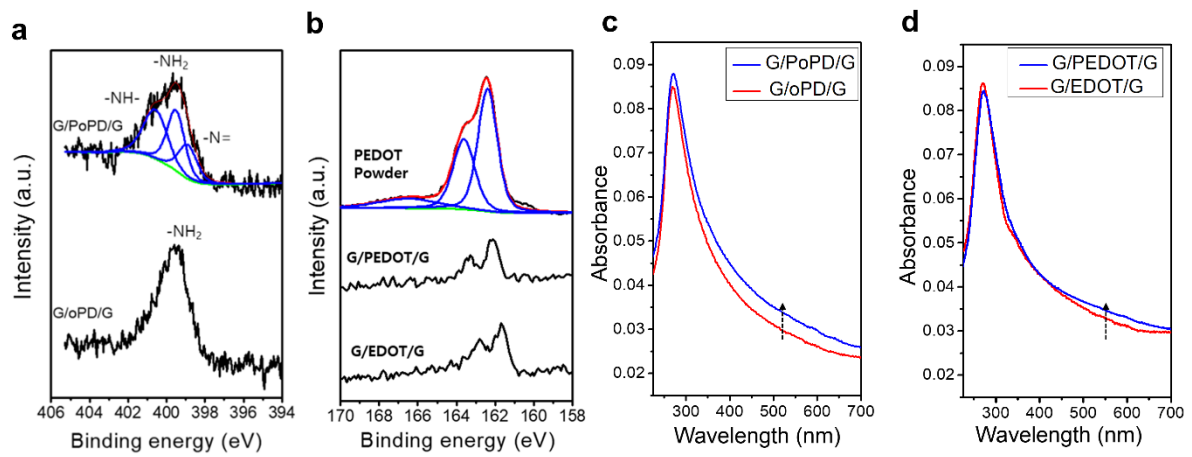


Figure 2.3.7. XPS spectra of before and after polymerization using d) oPD and e) EDOT in sandwiched graphene. UV-vis-NIR spectra of before and after polymerization using f) oPD and g) EDOT in sandwiched graphene.

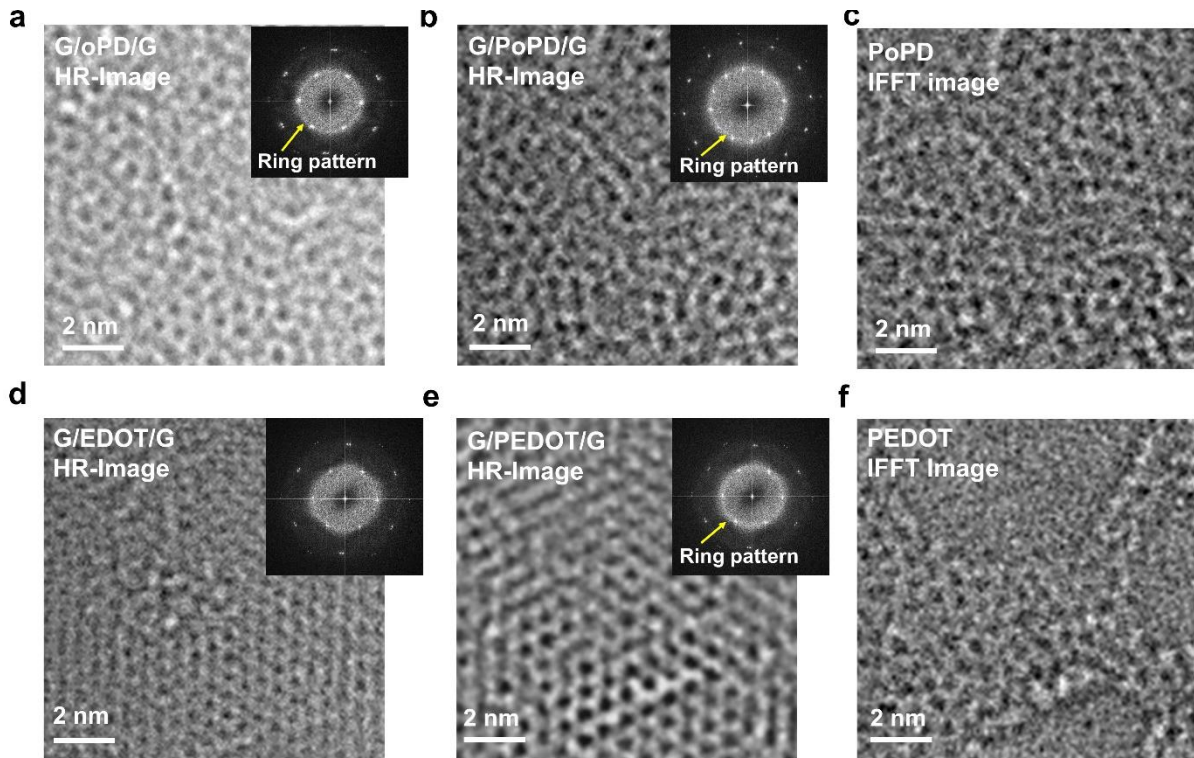


Figure 2.3.8. HR- and IFFT images of G/oPD/G, G/EDOT/G, G/PoPD/G, and G/PEDOT/G HR-images of a) before and b) after polymerization of G/oPD/G. Diffraction patterns (insets) showed that both oPD and PoPD showed ring patterns, indicating polycrystalline structure. c) IFFT image of PoPD shows 2D crystalline sheets. HR-images of d) before and e) after polymerization of G/EDOT/G. Diffraction patterns (insets) showed that PEDOT showed ring patterns, indicating polycrystalline structure. e) IFFT image of PEDOT shows small sized of crystalline domain.

2.3.4. Theoretical calculations

To support this proposal, theoretical calculations were performed. First, we investigated behavior of monomers on graphene (**Fig. 2.3.9a–c**). As expected, oPD and EDOT were planar on graphene, while dopamine was not. The binding energies between graphene and dopamine, oPD, and EDOT were calculated as -0.704, -0.558, and -0.559 eV, respectively. In the cases of the monomers in the graphene sandwich structure, graphene pockets were formed after geometrical optimization (**Fig. 2.3.9d–f**). Simultaneously, the dopamine in the graphene sandwich structure indicated significant deformation of the dopamine monomer, turning its structure into planar. When the aforementioned graphene pockets were formed, compressive force was generated, which induced a repulsive force between dopamine and graphene. Consequently, the calculation results yielded a positive binding energy. This compressive force is related to the high vdW pressure in the graphene sandwich structure. The formation of 2D polymers in the graphene sandwich structure can possibly be attributed to the planarization of monomers by high vdW pressure. The binding energy of dopamine, oPD, and EDOT in the graphene sandwich structure were calculated to be 3.72, 2.82, and 3.98 eV, respectively. Notably, oPD is the most stable in the graphene sandwich structure, and this might be ascribed to the greatest reduction in the I_{2D}/I_G of G/oPD/G and G/PoPD/G and 2D crystalline sheets of oPD and PoPD. Although the binding energy of EDOT on graphene is similar to that of oPD on graphene, the binding energy of EDOT was the highest in the graphene sandwich structure, indicating that EDOT was not more stable than the other monomers in the graphene sandwich structure. Because EDOT is five-membered ring monomer, which is different from the structure of graphene (six-membered ring), EDOT is not energetically stable in the graphene sandwich structure. Therefore, 2D crystallization and polymerization of EDOT occurred to lesser extents than those of dopamine and oPD.

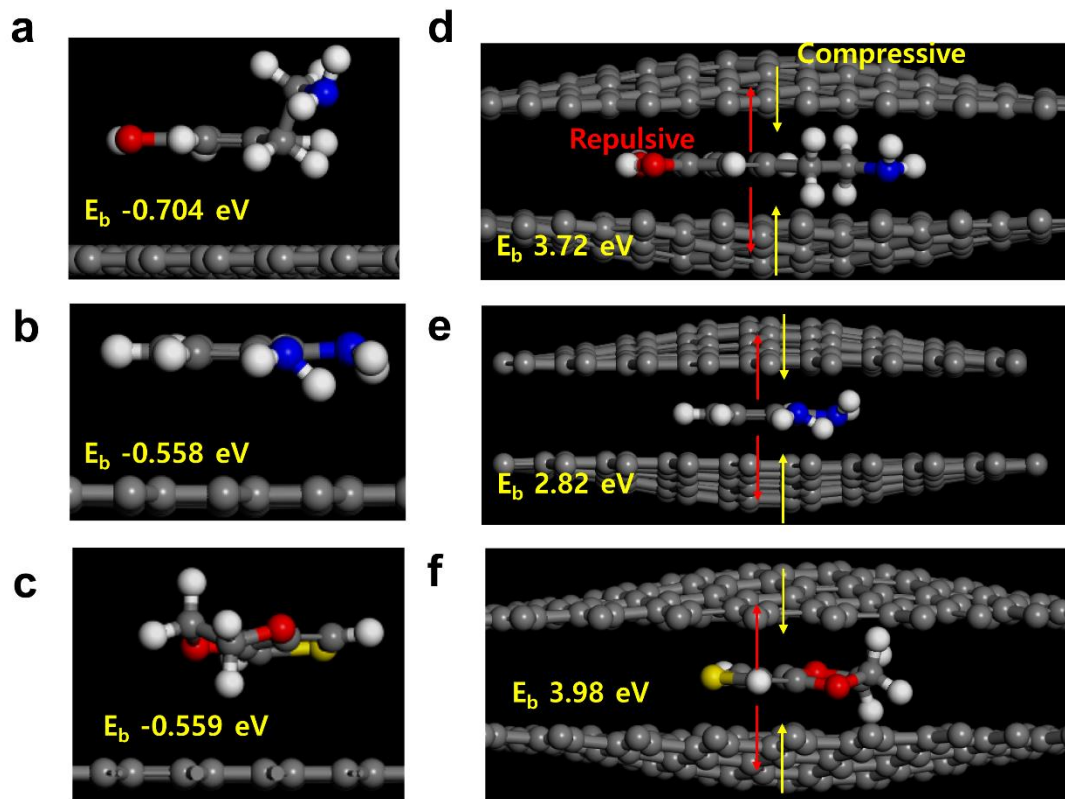


Figure 2.3.9. Calculations of monomers on graphene and in graphene sandwich. a-c) monomers on graphene. Geometry and binding energy of a) dopamine, b) oPD and c) EDOT on graphene. Binding energy (E_b) between graphene and each monomer is calculated in each figure. Geometry and binding energy of d) dopamine, e) oPD and f) EDOT in graphene sandwich. Binding energy for each monomer is calculated in each figure.

2.3.5. Effect of confined space for polymerization

To understand confinement effect and vdW pressure in polymerization in graphene sandwich, we compared G/PD/G (dopamine is polymerized in confined space) and PD/G (dopamine is polymerized in bulk space) (**Fig. 2.3.10**). Apparently, monomers on graphene appear to have polymerized after heating, but they did not form crystal structure. PD/G is prepared by heating of D/G, confirmed by XPS. However, the Raman spectra showed that there is no dramatic reduction of I_{2D}/I_G ratio after heating process. In addition, TEM images of polydopamine on graphene (Non-sandwich structure) showed that only amorphous polydopamine presents even though dopamine were successfully polymerized. Also, we check the FFT of PD/Graphene, but it shows only graphene with amorphous carbon pattern, which is different from PD in graphene sandwich. Through two control experiments, monomers on graphene, which are not in graphene sandwich, were polymerized but have no crystalline characteristics while monomers in graphene sandwich were polymerized and crystallized after heating. The presence of vdW pressures and confinement effect affect crystallization of polymers in graphene sandwich.

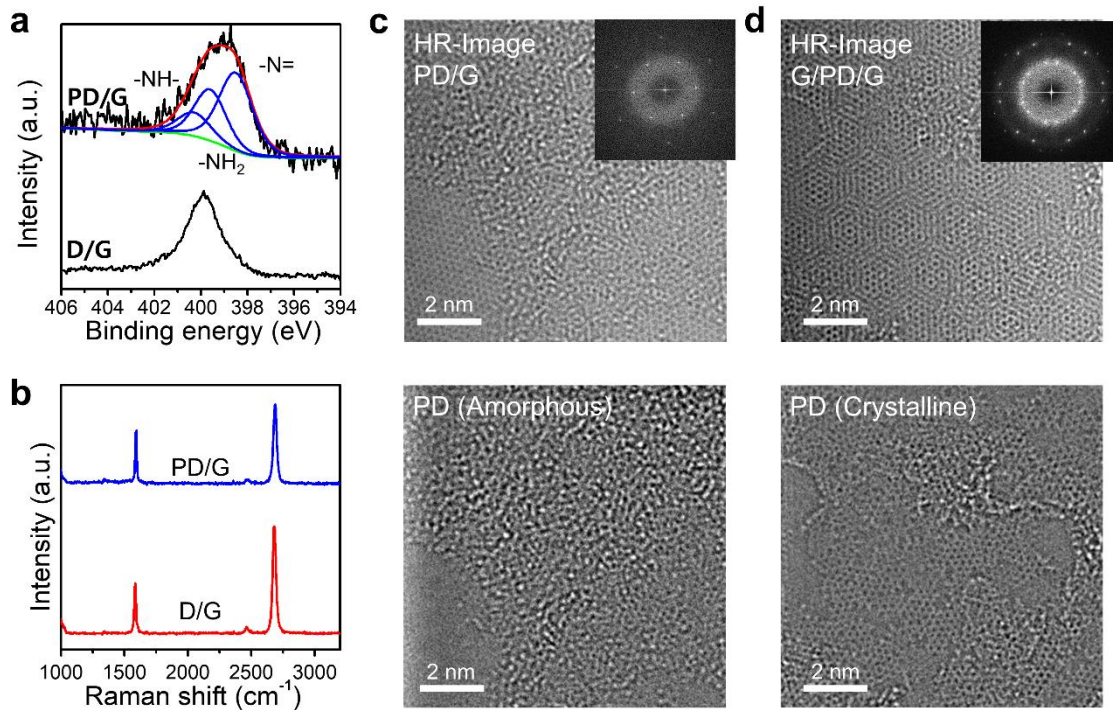


Figure 2.3.10. Comparison of non-sandwiched and sandwiched samples. a) XPS and b) Raman spectra of D/G and PD/G. PD/G is prepared by heating, and XPS confirmed polydopamine is successfully synthesized. TEM images and FFT of c) PD/G and d) G/PD/G. PD on graphene showed amorphous while PD in graphene sandwich showed polycrystalline characteristics.

2.3.6. Proposed structure of polydopamine in graphene sandwich

Based on PD (dark), which denotes single-layer polydopamine in the graphene sandwich structure, the structure of polydopamine was proposed (**Fig. 2.3.11**). An IFFT image of PD (dark) indicated the polycrystalline structure of 2D polydopamine. In PD (dark), there are multiple five-membered rings, in which N atoms are very likely to be present (**Figs. 2.3.11a–c**). The blue and green circles in the TEM images denote N and C atoms, respectively. The images of PD (dark) can be matched similarly to the images in **Figs. 2.3.11d–f**. In the TEM images and in the proposed structure, **1**, **2**, **3** correspond to pyridinic N, graphitic N, and pyrrolic N, respectively. The insets of **Figs. 2.3.11a–c** are magnified versions of the regions highlighted by white circles in each image. At the edge side of 2D polydopamine, pyridinic N (**1**) might be present in the five-membered ring as shown in **Figs. 2.3.11a** and **d**. Inside the five-membered ring, graphitic N (**2**), which is bonded to three carbon atoms, could be present (**Fig. 2.3.11b** and **2.3.11e**). Moreover, pyrrolic N (**3**) was observed where the atoms were not connected (**3** of inset of **2.3.11b** and **2.3.11c**). Overall, 2D polycrystalline polydopamine was successfully synthesized in the graphene sandwich structure owing to the nanoconfinement effect and high vdW pressure, and their structures were proposed successfully according to the TEM images of single-layer 2D polydopamine.

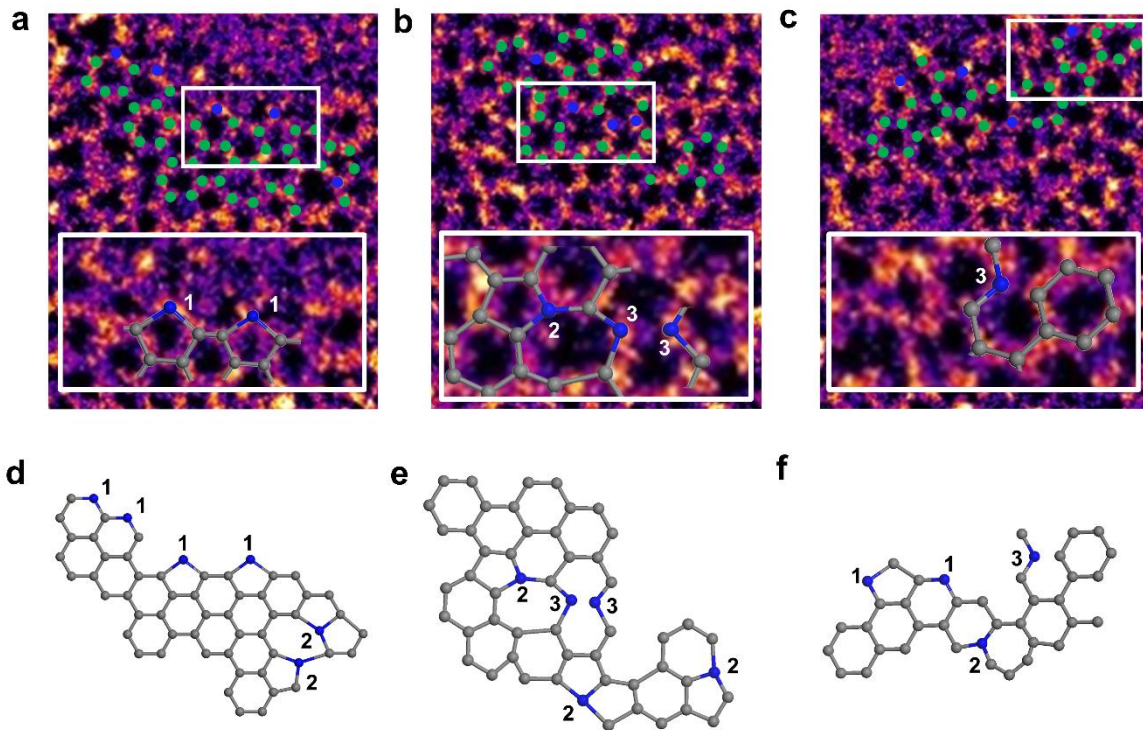


Figure 2.3.11. High-magnified IFFT image of G/PD/G (dark). a-c) In single-layer polydopamine sheets, many five-membered rings were observed. d-f) Proposed structure of polydopamine base on each figure a-c.

2.3.7. Improved sheet resistance and mechanical properties of G/polydopamine/G

It is known as the polydopamine, which is used in graphene sandwich, has good adhesive property for a long time.¹⁵⁻¹⁷ To evaluate mechanical property, bending stability and young's modulus were measured (Fig. 2.3.12). Sheet resistance of G/PD/G exhibited much lower sheet resistance ($344.38 \Omega \square^{-1}$) than single-layer graphene (G, $982.87 \Omega \square^{-1}$) and two-layer graphene (G/G, $642.03 \Omega \square^{-1}$) due to doping effect on graphene. To evaluate its bending stability, we measured sheet resistance during applying strain. Sheet resistance of G/PD/G was maintained even though strain is applied over 1.0 % while sheet resistance of G/G increased when strain is applied over 0.9 %, indicating breaking of graphene. Furthermore, Young's modulus was measured by nanoindentation test. The Young's modulus of G/PD/G is 35 % reinforced compared to G/G, indicating polydopamine enhance mechanical strength between graphene layers. In other words, 2D polydopamine makes graphene film stronger.

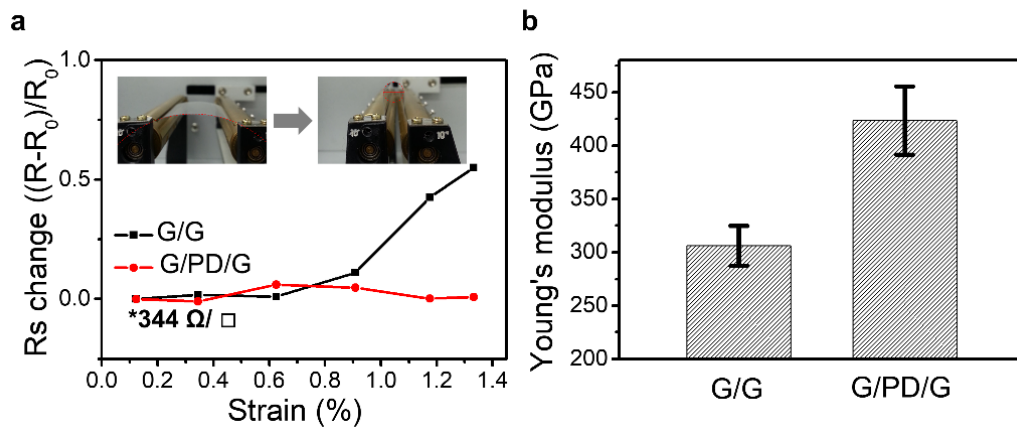


Figure 2.3.12. a) Bending stability test of G/G and G/PD/G. G/PD/G maintained sheet resistance even applying high strain compared to G/G. Transmittance of G/G and G/PD/G is 95.4% and 94.84%, respectively. b) Young's modulus of G/G and G/PD/G was measured by nanoindentation test. Polydopamine enhanced Young's modulus of two-layer graphene.

2.3.8. Optical property of 2D polydopamine

To estimate optical property of 2D polycrystalline polydopamine, reflectance contrast (RC) spectra was measured. Equation of RC spectra is explained by, $RC = 100 * (\text{Reflectance of substrate} - \text{reflectance of sample}) / (\text{reflectance of substrate} + \text{reflectance of sample})$. I compared 4 samples of G/G (graphene/graphene), PD/G (PD is amorphous, polymerized in bulk space), G/D/G (before polymerized sample) and G/PD/G (PD is 2D polycrystalline polydopamine). At 600 nm, strong absorption peak was measured due to graphene. Due to strong absorption, graphene can be distinguished by naked eye. Only graph of G/PD/G showed strong reflectivity at 520 nm, which is attributed to 2D polycrystalline polydopamine. To support our experiment results, simulation for RC spectra was performed. Simulation results of G/PD/G is similar to the experimental results for RC spectra of G/PD/G. Therefore, this strong reflectivity at 520 nm is due to 2D polycrystalline polydopamine.

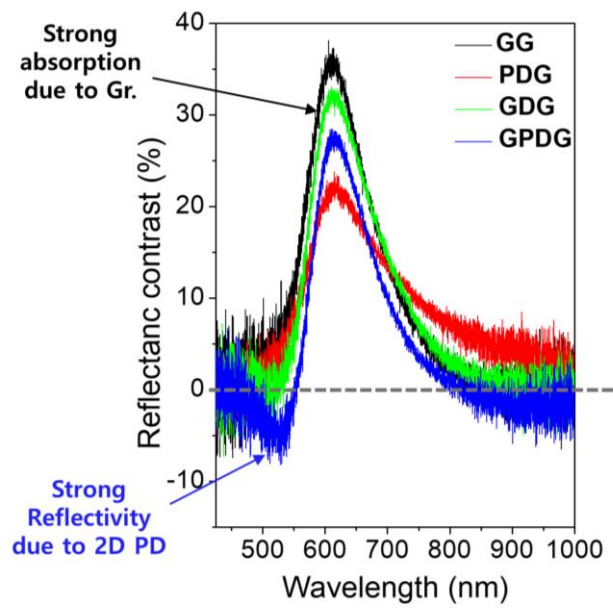


Figure 2.3.13. Reflectance contrast spectra of G/G (black), PD/G (red, PD is amorphous), G/D/G (green) and G/PD/G (blue, PD is 2D polycrystalline polydopamine). Strong absorption at 600 nm is due to graphene. Strong reflectivity at 520 nm is due to 2D polycrystalline polydopamine compared to results of PD/G.

2.3.9. Extraction of polydopamine from graphene sandwich

To extract polydopamine from graphene sandwich, splitting by Ni deposition was performed (**Fig. 2.3.14**). Since interaction between graphene and Ni is very strong, I deposited Ni film on both top and bottom-side of G/PD/G. I split prepared sample by physically. By doing so, I obtained PD/G/Ni (top) and PD/G/Ni (bottom). Raman spectra of both PD/G/Ni (top) and PD/G/Ni (bottom) showed that reduction of I_{2D}/I_G was observed in both top and bottom samples. In other words, 2D polydopamine presents both top and bottom samples. Some points in PD/G/Ni (bottom) showed single-layer graphene, indicating thin 2D polydopamine presents in bottom sample while thick 2D polydopamine presents in top sample. By this splitting technique, polydopamine is successfully extracted.

In summary, for the first time, we observed crystallization of polymer in graphene sandwich. Monomers such as dopamine, oPD, EDOT are polymerized in graphene sandwich by heating (180 °C) and polymers are crystallized during polymerization process. 2D Crystalline sheet-like structure was observed by TEM. Also, this 2D crystalline sheet-like structure is dependent on structure of monomers. The high vdW pressure and nanoconfinement effect induced 2D crystallization and polymerization in graphene sandwich. When we used adhesive polymer in graphene sandwich, mechanical property of graphene enhanced and when we used conducting polymer in graphene sandwich, electrical property of graphene enhanced. These results highlight the feasibility of graphene sandwich vessel to synthesize crystalline polymer more easily.

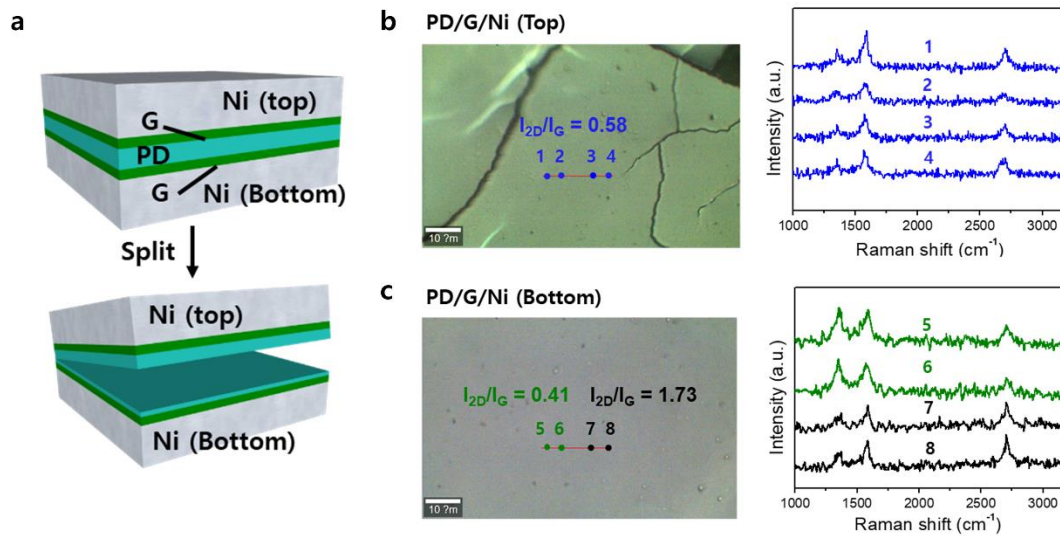


Figure 2.3.14. Extraction of polydopamine from graphene sandwich by splitting technique. a) Schematic illustration of splitting technique. Ni is deposited on both top and bottom-side of G/PD/G by using e-beam deposition and sputter. After physically splitting, PD/G/Ni (top) and PD/G/Ni (bottom) were obtained. Raman spectra of both PD/G/Ni (top) and PD/G/Ni (bottom) showed reduction of I_{2D}/I_G ratio, indicating that 2D polydopamine presents both top and bottom samples.

2.4. References

- (1) Petrosko, S. H.; Johnson, R.; White, H and Mirkin, C. A. Nanoreactors: small spaces, big implications in chemistry. *J. Am. Chem. Soc.*, **2012**, *38*, 7443-7445.
- (2) Li, H.; Xiao, J.; Fu, Q. and Bao, X. Confined catalyst under two-dimensional materials. *Proc. Natl. Acad. Sci. USA*, **2017**, *111*, 17023-17028.
- (3) Sastre, G. and Corma, A. The confinement effect in zeolites. *J. Mol. Catal. Chem.*, **2009**, *305*, 3-7.
- (4) Pan, X. and Bao, X. The effects of confinement inside carbon nanotubes on catalysts. *Acc. Chem. Res.*, **2011**, *44*, 553-562.
- (5) Yuk, J. M. *et al.* High-resolution EM of colloidal nanocrystal growth using graphene liquid cells. *Science*, **2012**, *336*, 61-64.
- (6) Park, J. *et al.* 3D Structure of individual nanocrystals in solution by electron microscopy. *Science*, **2015**, *349*, 290-295.
- (7) Wang, C.; Qiao, Q.; Shokuhfar, T. and Klie, R. F. High-resolution electron microscopy and spectroscopy of ferritin in biocompatible graphene liquid cells and graphene sandwiches. *Adv. Mater.* **2014**, *26*, 3410-3414.
- (8) Zhang, J. *et al.* Clean transfer of large graphene single crystals for high-intactness suspended membranes and liquid cells. *Adv. Mater.* **2017**, *29*, 1700639.
- (9) Chen, Q. *et al.* 3D motion of DNA-Au nanoconjugates in graphene liquid cell electron microscopy. *Nano Lett.* **2013**, *13*, 4556-4561.
- (10) Park, J. *et al.* Direct observation of wet biological samples by graphene liquid cell transmission electron microscopy. *Nano Lett.* **2015**, *15*, 4737-4744.
- (11) Algara-Siller, G. *et al.* Square ice in graphene nanocapillaries *Nature*, **2015**, *519*, 443-446.
- (12) Vasu, K. S. *et al.* van der Waals pressure and its effect on trapped interlayer molecules *Nat. Commun.*, **2016**, *7*, 12168.
- (13) Lehnert, T. *et al.* *In situ* Crystallization of the insoluble anhydrite AII phase in graphene pockets. *ACS Nano*, **2017**, *11*, 7967-7973.

- (14) Brokman, T.; Fulans, A.; Krasheninnikob, A. and Nieminen, R. van der Waals bonding in layered compounds from advanced density-functional first principles calculations. *Phys. Rev. Lett.* **108**, 235502 (2012).
- (15) Lee, H.; Dellatore, S. M.; Miller, W. M. and Messersmith P. B. Mussel-inspired surface chemistry for multifunctional coatings. *Science*, **2007**, *318*, 426-430.
- (16) Wei, Q.; Zhang, F.; Li, J.; Li, B. and Zhao C. Oxidant-induced dopamine polymerization for multifunctional coatings. *Polym. Chem.*, **2010**, *1*, 1430-1433.
- (17) Du, X. *et al.* UV-triggered dopamine polymerization: control of polymerization, surface coating, and photopatterning. *Adv. Mater.*, **2014**, *26*, 8029-8033.
- (18) Liebscher, J. *et al.* Structure of polydopamine: A never-ending story? *Langmuir*, **2013**, *29*, 10549-10548.
- (19) Luo, R. *et al.* Improved immobilization of biomolecules to quinone-rich polydopamine for efficient surface functionalization. *Colloids Surf B Biointerfaces*, **2013**, *106*, 66-73.
- (20) Liu, X.; Wang, G.; Liang, R.; Shi, L., and Qiu, J. Environment-friendly facile synthesis of Pt NPs supported on polydopamine modified carbon materials. *J. Mater. Chem. A*, **2013**, *1*, 3945-3953.
- (21) Xu, W. *et al.* Ultrathin thermoresponsive self-folding 3D graphene. *Sci. Adv.*, **2017**, *3*, e1701084.
- (22) Yan, X. *et al.* A novel imidazolium-based amphoteric membrane for high-performance vanadium redox flow battery. *Langmuir*, **2013**, *29*, 10549-10548.
- (23) Ferrari, A. C. and Basko, D. M., Raman spectroscopy as a versatile tool for studying the properties of graphene. *Nat. Nanotechnol.*, **2013**, *8*, 235-246.
- (24) Malard, L. M.; Pimenta, M. A.; Dresselhaus, G. and Dresselhaus, M. S., Raman spectroscopy in graphene. *Phys. Rep.*, **2009**, *473*, 51-87.
- (25) Das, A. *et al.* Monitoring dopamines by raman scattering in an electrochemically top-gated graphene transistor. *Nat. Nanotechnol.*, **2013**, *3*, 210-215.
- (26) Dong, X. *et al.* Doping single-layer graphene with aromatic molecules. *Small*, **2009**, *5*, 1422-1426.

(27) Jung, N. *et al.* Optical reflectivity and raman scattering in few-layer-thick graphene highly doped by K and Rb. *ACS Nano*, **2011**, *5*, 5708-5716.

(28) Sato, K. *et al.* Zone folding effect in raman G-band intensity of twisted bilayer graphene. *Phys. Rev. B*, **2012**, *86*, 125414.

(29) Carozo, V. *et al.* Resonance effects on the raman spectra of graphene superlattices. *Phys. Rev. B*, **2013**, *88*, 085401.

(30) Meyer, J. C. *et al.*, The structure of suspended graphene sheets. *Nature*, **2007**, *446*, 60-63.

Chapter 3: h-BN for Proton Exchange Membrane in Proton Exchange Membrane Fuel Cells

3.1 Introduction

Generally, atomic-thickness two-dimensional (2D) materials such as graphene and hexagonal boron nitride (h-BN) are utilized to form some of the thinnest membranes due to very low transport resistance and very high permeation flux.¹⁻⁶ In particular, it has been demonstrated that the high proton conductivity of graphene and h-BN makes them highly suitable for proton exchange membranes, both theoretically^{7,8} and experimentally⁹⁻¹². Hu *et al.* reported that mechanical-exfoliated monolayered h-BN or graphene inserted between two Nafion films shows excellent proton conductivity (approximately 0.1 or 0.04 S cm⁻², respectively, at room temperature).⁹ These conductivity values are lower than that of Nafion 211 (approximately 24 S cm⁻² at room temperature).¹³ However, the slightly lowered proton conductivities of these 2D materials can be compensated for by their atomically thin thickness. In the case of 2D materials, protons permeate through centers of hexagonal rings, the pores formed by the electron clouds.⁷⁻¹¹ Since bonding between the B and N atoms are polarized, the valence electrons to accumulate around the N atoms and so, pores of h-BN are larger than those of graphene.⁹ Thus, the proton areal conductivity of h-BN is higher than that of graphene. Definitely, the inevitable defects in large-area h-BN or graphene grown by chemical vapor deposition provide a path for protons and larger species than those, thus enhancing the conductivity but decreasing selectivity.^{1,7,12}

So far, these reports on the high proton conductivity of h-BN have led to evaluate the suitability of these materials for use in direct methanol fuel cells (DMFCs), where h-BN used with a sandwich-like structure is formed by inserting a large-area graphene or h-BN monolayer between two commercial Nafion films. The DMFC performance are improved because the sandwich-like composite structure prevents methanol crossover.^{14,15} However, it is noted that the graphene or h-BN monolayer acts as an additional membrane for proton transport along with the Nafion film, which is a primary membrane. Therefore, given their intrinsic defects and grain boundaries, CVD-grown large-area 2D materials cannot be utilized independently as proton exchange membranes in the fuel cells. As a result, 2D materials find limited use in proton exchange membrane fuel cells (PEMFCs) even though these materials show high proton conductivity and excellent chemical stability.¹⁶⁻²⁰ To overcome this limitation, it is crucial to develop methods of fabricating defect-free, large-area, single-crystal h-BN or graphene. Furthermore, multilayers of h-BN or graphene with an AA' stacking order would be even more desirable, in case unexpected defects are generated in these materials during their production and transfer.

Herein, we report the fabrication of membrane electrode assemblies (MEAs) using large-area single-layer graphene (1L-Gr) and h-BN (1L-BN), and trilayer h-BN (single-oriented 3L-BN with AA' stacking) for use as 2D material-based Nafion film-free proton exchange membranes in fuel cell systems. To simplify the handling of the atomic-scale-thickness single-layer and trilayer membranes comprising the MEAs, an interfacial binding layer (IBL) was coated on these membranes. Since 1L-BN and 1L-Gr exhibit intrinsic defects and grain boundaries, the fuel cells with the 1L-BN and 1L-Gr membranes exhibited high H₂ permeation current densities, of 10.08 and 9.1 mA cm⁻², respectively, at 0.4 V, indicating that gas crossover occurred through the membranes. However, the fuel cell with an AA'-stacked 3L-BN membrane exhibited a low H₂ permeation current density at 2.69 mA cm⁻², which is even lower than that obtained for a fuel cell with a commercial Nafion 211 film (3.7 mA cm⁻²). Furthermore, the results of an accelerated stress test (AST) revealed that the chemical inertness of the AA'-stacked 3L-BN membrane significantly improved the long-term stability of the corresponding fuel cell. These results indicate that the AA'-stacked 3L-BN membrane effectively prevented gas crossover which is one of the primary causes of radical formation during fuel cell operation. Also, the AST results exhibit that the AA'-stacked 3L-BN membrane can be used at low humidity (30% RH) and high temperature (90 °C).

3.2 Experimental process

3.2.1. Growth of single-layer graphene

Single-layer graphene was grown on Cu foil (99.8 % purity, 0.025 mm thick, Alfa Aesar) via low-pressure chemical vapor deposition (LP-CVD) method. Cu foil was placed at the center of quartz CVD furnace, and the furnace was heated to 1000 °C in flow of H₂ gas 10 sccm. The Cu foil was pre-annealed at 1000 for 30 minutes. After growth time for 30 minutes, the furnace was cooled down to room temperature, quickly.

3.2.2. Growth of single layer h-BN

Single-layer h-BN was grown on platinum foil (99.95% purity, 0.125 mm thick, Goodfellow). Pt foil was placed at the center of main quartz CVD furnace and ammonia borane (97 % purity, Sigma-Aldrich) was placed in a sub-chamber. The furnace was heated to 1100 °C in flow of a H₂ gas 10 sccm, and the sub-chamber was heated to 150 °C for the decomposition of ammonia borane. The Pt foil was pre-annealed at 1100 °C for 30 minutes under flow of H₂ gas. The growth of h-BN on Pt foil started by opening a valve of the sub-chamber, entering ammonia borane into main CVD chamber. After finishing the growth, the furnace was quickly cooled down to room temperature under H₂ gas condition.

3.2.3. Growth of trilayer h-BN

Trilayer h-BN with AA' stacking order was grown by a LPCVD method. A sapphire substrate (c-plane) was placed in the middle of a 2-inch alumina tube CVD furnace, and ammonia borane (97% purity, Sigma-Aldrich) was placed in a sub-chamber. The furnace was heated to 1400 °C under flow of Ar gas (10 sccm) and H₂ gas (10 sccm). The sub-chamber was heated to 130 °C for the decomposition of ammonia borane. The growth of trilayer h-BN with AA' stacking order on sapphire substrate was initiated by opening a valve of the sub-chamber. After opening a valve of the sub-chamber, source was supplied for 30 minutes. After growth completion, the furnace was cooled down to room temperature under Ar and H₂ gas.

3.2.4. Preparation of trilayer h-BN by repeated transfer method

Single-layer h-BN was synthesized on Pt foil substrate by using LP-CVD methods. PMMA (Poly(methyl methacrylate)) was coated on h-BN on Pt foil. By using electrochemical bubbling system, PMMA/h-BN was transferred onto SiO₂ substrate. PMMA was removed by immersing prepared PMMA/h-BN into acetone and annealing at 400 °C with Ar atmosphere. Another single-layer h-BN was transferred onto h-BN/SiO₂ sample to prepare PMMA/bi-layer h-BN. To remove PMMA,

immersion in acetone and annealing process were used. By repeated transfer, trilayer h-BN/SiO₂ sample was prepared.

3.2.5. Characterization of trilayer h-BN with AA' stacking order

The surface morphology of trilayer h-BN with AA' stacking order was characterized by atomic force microscopy (Dimension Icon, Bruker). Raman spectra were measured by using micro Raman spectrometer (alpha 300, WITec GmbH) with 532-nm laser. The peak around 1370 cm⁻¹ corresponds to E_{2g} mode. The UV-visible absorption spectrum was measured by using UV-vis-NIR spectrometer (Cary 5000 UV-vis-NIR, Agilent). To obtain low-energy electron diffraction (LEED) (SPECTRALEED, Omicron NanoTechnology GmbH) patterns, trilayer h-BN on Al₂O₃ sample was loaded in ultra-high vacuum system (~10⁻¹⁰ torr). The LEED pattern shows hexagonally arranged spots in Figure S1e, rather than a ring-shaped pattern, revealing that the trilayer h-BN is single-oriented over the entire sample.²¹ For high-resolution imaging and selected area electron diffraction (SAED) of h-BN, low voltage Cs aberration-corrected transmission electron microscopy (Titan Cube G2 60-300, FEI) was operated at 80 kV with monochromated electron beam. Since trilayer h-BN was grown with AA' stacking order, a Moiré pattern was not shown in TEM top-view image unlike 3L-BN-transferred. Also, diffraction pattern of AA'-stacked 3L-BN revealed that h-BN shows AA'-stacking order.

3.2.6. Fabrication process of fuel cells using 2D materials

We developed a method to fabricate a fuel cell without any damage of 2D materials. The ink of anode and cathode catalysts was prepared by mixing 0.135 g Pt/C (HiSPEC-4000, Johnson-Matthey), 0.932 g of DI water, 0.186 g of isopropyl alcohol, and 0.999 g of 5 wt% Nafion ionomer (1100 EW, DuPont Fuel Cells). All cathodes and anodes had 27 wt% Nafion ionomer. The Pt contents on anode and cathode catalysts were controlled at 0.15 and 0.35 mg cm⁻², respectively.

The anode catalyst layer, which consisted of the Nafion ionomer and Pt/C, was spray-coated on a SiO₂ substrate (3.0 cm × 3.0 cm). The catalyst-coated SiO₂ substrate was dried completely to remove residual solvent in 80 °C. The Mylar anode sample was hot-pressed to sufficiently flatten the surface of the anode catalyst at 153 kgf cm⁻² and 30 °C for 30 sec. In this work, we coated an interfacial binding layer (IBL) using 5 wt% Nafion solution (1100 EW, DuPont Fuel Cells) in the MEA fabrication process to create an IBL/2D material/IBL structure because it is usually difficult to handle 2D materials that can be easily torn on the catalyst layer. Specifically, the structure of IBL/anode catalyst layer was prepared by spin-coating the 5 wt% Nafion solution onto the anode catalyst layer. To form the IBL/2D material/IBL (thickness: 20 μm) structure, a CVD-grown graphene or h-BN sheet (size: 2 cm × 2 cm)

was transferred by using the IBL layer instead of poly(methyl methacrylate) (PMMA) used in a typical transfer process. The IBL/2D material was prepared by spin-coating the 5 wt% Nafion solution onto the 2D material, after which the IBL/2D material was detached from the substrate used to grow the 2D material, and then transferred onto an IBL/anode catalyst layer to complete the IBL/2D material/IBL/anode sample. A cathode catalyst layer was then spray-coated on the prepared sample. The cathode catalyst was also dried completely at 80 °C. A hydrofluoride (HF, 10 wt%) solution was used to detach the prepared MEA from the SiO₂ substrate. The edge of the MEA was then sealed with polyethylene terephthalate (PET) by pressing for easier handling MEA, leaving an exposed active area measuring 1.5 cm × 1.5 cm.

3.2.7. Evaluation of fuel cells

All single cell experiments were conducted at 70 °C, 100% RH, and atmospheric pressure conditions. The temperature of the gas lines to the anode and the cathode were always set 10 °C above the temperature of the humidifier to avoid condensation of water vapor. H₂ and air gases were used as anode and cathode reactants, respectively. The reactant flow rates for the anode and cathode were 60 and 250 mL min⁻¹, respectively. In this work, we conducted a conventional activation by repeating the voltages in a range of potential from 0.8 to 0.3 V until stabilizing the single cell's performance for 10 h. After confirmation of an open circuit voltage (OCV), the polarization curves were obtained at a scan rate of 10 mV s⁻¹ from OCV to 0.3 V. The cathode and the anode were purged with N₂ (75 mL min⁻¹) and H₂ (200 mL min⁻¹) and then cyclic voltammetry (CV) and H₂ permeation current density were measured using an EIS potentiostat. The potential range and the scan rate were 0.04 to 1.2 V (vs. RHE) and 20 mV s⁻¹, respectively. The accelerated stress test (AST) was performed by applying OCV for 100 h under 30% RH, 90 °C, and atmospheric pressure conditions.

3.3 Results and discussions

3.3.1. Fabrication of fuel cells using 2D materials

The fuel cell with 2D materials are followed by the methods in **Fig. 3.3.1**. To fabricate a fuel cell with this structure, a modified process based on the use of 2D materials and slightly different from the general process for fabricating PEMFCs was employed (**Fig. 3.3.1b**). The fabrication process is discussed in the Experimental section. Step (i) in **Fig. 3.3.1b** corresponds to the transfer of the IBL/2D material onto the IBL/anode/SiO₂ substrate structure. Spin- or spray-coating the 5 wt% Nafion solution for the IBL was used in the proposed MEA fabrication process in order to form an IBL/2D material/IBL structure, because it is usually extremely difficult to handle 2D materials as they are readily ripped off from the catalyst layer. It should be noted that this IBL layer did not serve as a proton exchange membrane. The characteristics of the IBL layer are discussed later. A cathode catalyst slurry was then spray-coated on the prepared sample (steps (ii) and (iii) in **Fig. 3.3.1b**). A hydrogen fluoride (HF) solution was used to separate the prepared MEA from the SiO₂ substrate. The edge of the MEA was then sealed with polyethylene terephthalate (PET) by pressing to allow for easier handling, resulting in an exposed active area with dimensions of 1.5 cm × 1.5 cm. The fuel cells were then assembled using the edge-sealed MEA and the gas-diffusion layers (GDLs), bipolar plates, current collectors, and end plates (step (vi) in **Fig. 3.3.1b**).

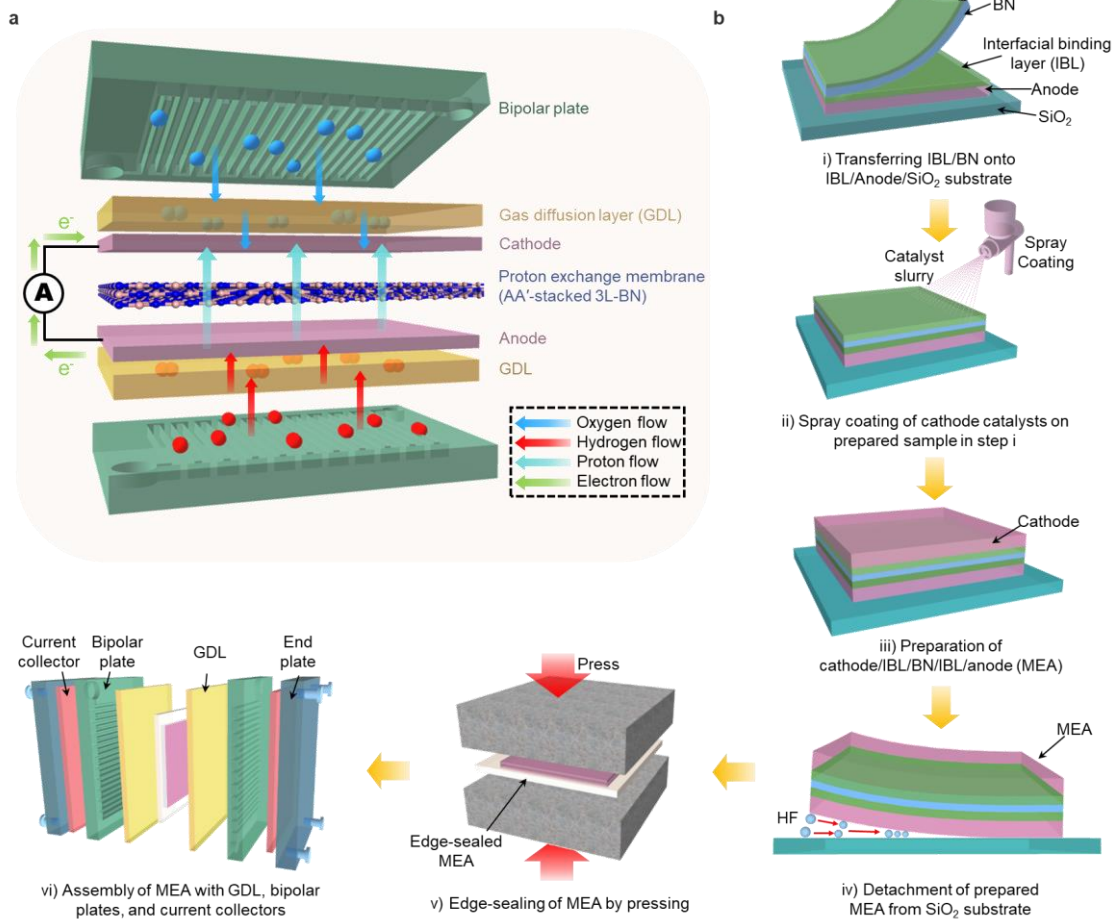


Figure 3.3.1. Schematic illustration of fuel cells formed using 2D materials for proton exchange membrane. a), Schematic illustration of fuel cell formed using AA'-stacked 3L-BN for proton exchange membrane. b) Schematic illustration of process for fabricating fuel cells using 2D materials. Fabrication process is modified and different from general process for fabricating PEMFCs.

3.3.2. Performances of fuel cell using single-layer materials

We compared the performances of the fuel cell with 2D materials and Nafion 211 (thickness 25 μm). First, we measured performance of the fuel cell with single-layer h-BN and graphene (**Fig.3.3.2 and Fig. 3.3.3**). Cyclic voltammetry showed that fuel cell with single-layer h-BN and graphene is working well. In I-V curves of fuel cell with single-layer h-BN and graphene, the current densities were 1.03 and 1.05 A cm^{-2} at 0.6 V and maximum power densities were 0.68 and 0.67 W cm^{-2} , respectively. These values are comparable to fuel cell using commercial Nafion 211 (Current density at 0.6 V = 1.30 A cm^{-2} , Maximum power density = 0.86 W cm^{-2}). To evaluate permeability of the fuel cell, H_2 permeation current densities were measured. The H_2 permeation current densities of fuel cell with single-layer h-BN and graphene showed 10.08 and 9.1 mA cm^{-2} at 0.4 V and open circuit voltage (OCV) values are 0.894 and 0.899 V, respectively. The H_2 permeation current density and OCV value of fuel cell with Nafion 211 are 3.70 mA at 0.4 V and 0.942, respectively. It is noted that fuel cell with single-layer h-BN and graphene showed low OCV due to gas crossover through defects and grain boundaries generated in these 2D materials during their growth by CVD and subsequent transfer process (**Fig. 3.3.4**).

3.3.3. Performances of fuel cell using only IBL layers

For reference experiment, we fabricated fuel cell with only IBLs (**Fig. 3.3.5**). We measured cyclic voltammetry and H_2 permeation current density of fuel cell with only IBLs. CV spectra showed inclined slopes, indicating that IBL does not act as proton exchange membrane. Additionally, H_2 permeation current density is too high (14 mA cm^{-2}), only IBL does not act as proton exchange membrane. This means that 2D materials can be utilized as primary proton exchange membranes.

3.3.4. Performances of fuel cell using trilayer h-BN; turbostratic stacking and AA'-stacking

To overcome the limitation of CVD-grown single-layer materials, two types of trilayer h-BN were prepared by repeated-stacking of single-layer h-BN (3L-BN-transferred, turbostratic stacking) and by direct growth (AA'-stacked 3L-BN). Cyclic voltammetry showed that fuel cell with 3L-BN-transferred and AA'-stacked 3L-BN is working well. From I-V curves and power density curves, the current densities were 0.88 and 1.00 mA cm^{-2} at 0.6 V for 3L-BN-transferred and AA'-stacked 3L-BN, respectively. The maximum power densities were 0.63 and 0.66 W cm^{-2} for 3L-BN-transferred and AA'-stacked 3L-BN, respectively. To begin with, the H_2 permeation current density of 3L-BN-transferred was lower at 6.32 mA cm^{-2} than those of the cells based on 1L-BN and 1L-Gr and its OCV was higher at 0.919 V. These improvements in the H_2 permeability and the OCV can be explained by the structural

differences shown in **Fig. 3.3.4**. As shown in **Fig. 3.3.4**, 3L-BN-transferred exhibited turbostratic stacking. Therefore, even if defects and grain boundaries were present in each layer of 3L-BN-transferred, some of them were probably blocked in the stacked 3L-BN-transferred structure, so that crossover through 3L-BN-transferred was reduced. However, the current density of 3L-BN-transferred was slightly lower than that of 1L-BN because 3L-BN-transferred not only exhibited a lower degree of gas crossover but also poorer proton transport owing to the random stacking of the three layers. In other words, turbostratic configuration not only blocks H₂ gas but also proton transport in the fuel cell with 3L-BN-transferred.

On the other hand, the fuel cell with AA'-stacked 3L-BN were measured. The polarization data, power density, H₂ permeation current density, and CV curves, and of the fuel cell based on AA'-stacked 3L-BN are shown in **Fig. 3.3.2**, while the values are listed in **Table 1**. The OCV and H₂ permeation current density at 0.4 V of this fuel cell were 0.958 V and 2.69 mA cm⁻², respectively, which are much higher values than those for the cells based on 1L-BN and 3L-BN-transferred. In polarization curves, the current density at 0.6 V of the fuel cell based on AA'-stacked 3L-BN was 1.0 A cm⁻² and its power density was 0.66 W cm⁻²; these values are similar to those of the cell based on 1L-BN. Due to configuration of AA'-stacking, proton transport is not prevented like turbostratic stacking. With low power density, high OCV and low H₂ permeation current density was obtained in the fuel cell with AA'-stacked 3L-BN.

3.3.5. Characterization of 3L-BN-transferred and AA'-stacked 3L-BN

AA'-stacked 3L-BN was characterized by various methods. We used 2 cm x 2 cm size of AA'-stacked 3L-BN (**Fig. 3.3.6** and **Fig. 3.3.7**). The thickness of AA'-stacked 3L-BN is approximately 1.3 nm, corresponding to trilayer h-BN thickness. Raman spectra is shown at 1370 cm⁻¹ with high crystallinity, indicating E_{2g} mode of h-BN. UV-vis-NIR spectrum showed absorption bandgap is a 6 eV. Low-energy electron diffraction (LEED) pattern demonstrated that our h-BN is single-oriented on sapphire substrate. The spots marked with red and yellow circles in zoomed-in LEED pattern correspond to h-BN and sapphire, respectively. Transmission electron image demonstrated that 3L-BN grown on sapphire is AA'-stacking. Our AA'-stacked 3L-BN showed excellent uniformity, which is confirmed by AFM measurement. After transfer onto SiO₂, uniformity of our film is maintained. On the other hand, 3L-BN made by repeated transfer showed turbostratic stacking characteristics (**Fig. 3.3.8**). Moire patterns were observed in top-view TEM images of 3L-BN-transferred and 18 spots were observed in FFT diffraction patterns, indicating that turbostratic trilayers of h-BN.

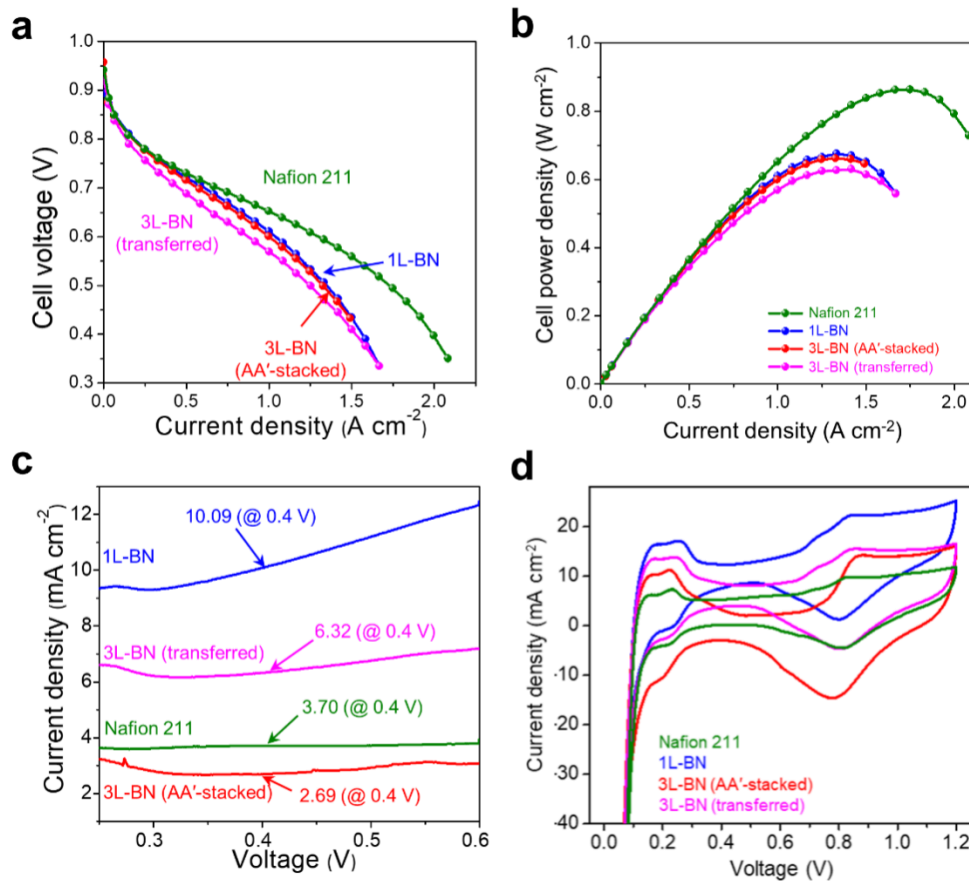


Figure 3.3.2. Comparison of performances for fuel cell using various 2D materials and commercial Nafion 211. a) Polarization curves, b) power density curves, and c) H₂ permeation current density results d) cyclic voltammetry (CV) for various 2D materials and Nafion 211. To obtain polarization results, fuel cells are operated at 70 °C and relative humidity 100%. H₂ gas (0.06 L min⁻¹) and air (0.246 L min⁻¹) were used as fuel and oxidant, respectively. For H₂ permeation current density measurements, H₂ gas was supplied at anode (0.2 L min⁻¹) and N₂ gas was supplied at cathode (0.075 L min⁻¹). All measurements were performed at atmospheric pressure condition.

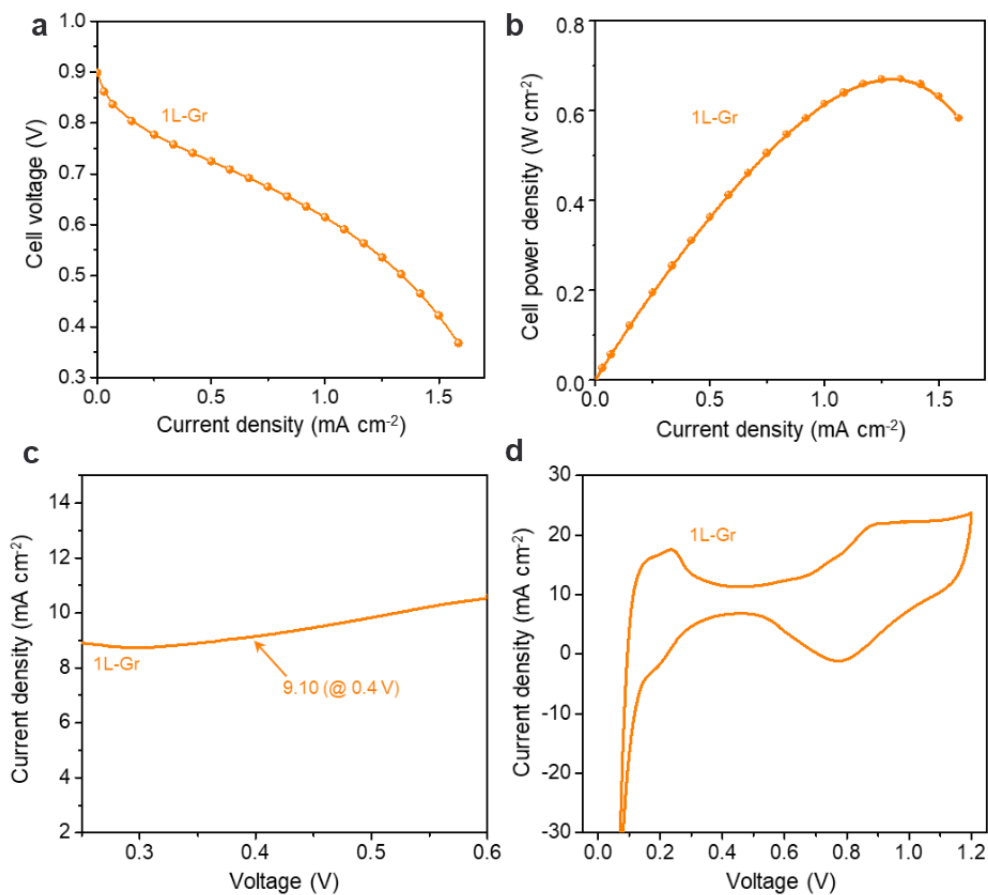


Figure 3.3.3. Performances of fuel cell using single-layer graphene. a) polarization, b) power density, c) H₂ permeation current density, and d) CV results for fuel cell using single-layer graphene. To obtain polarization results, fuel cells are operated at 70 °C, relative humidity 100%, and atmospheric and H₂ gas (0.06 L min⁻¹) and air (0.246 L min⁻¹) was used as fuel and oxidant, respectively. For CV and H₂ permeation current density measurements, H₂ gas was supplied at anode (0.2 L min⁻¹) and N₂ gas was supplied at cathode (0.075 L min⁻¹). All measurements were done at atmospheric pressure condition.

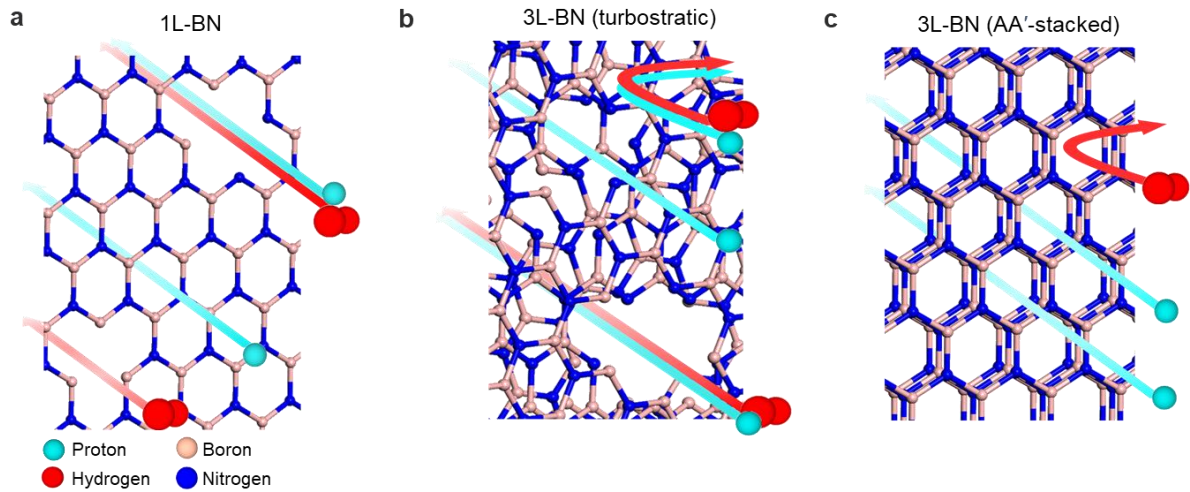


Figure 3.3.4. Schematic illustrations of proton exchange membranes in a) 1L-BN , b) 3L-BN made by transfer repeatedly, c) AA'-stacked 3L-BN. Through defects of 1L-BN, H₂ gas crossover occurred, corresponds to high H₂ permeation current density and low OCV of fuel cell with 1L-BN. In case of 3L-BN (transferred, turbostratic stacking), H₂ permeation current density was lowered, but current density is also lowered due to prevention of proton transport. AA'-stacking configuration does not prevent proton transport and blocks H₂ gas crossover, resulting in high OCV and low H₂ permeation current density.

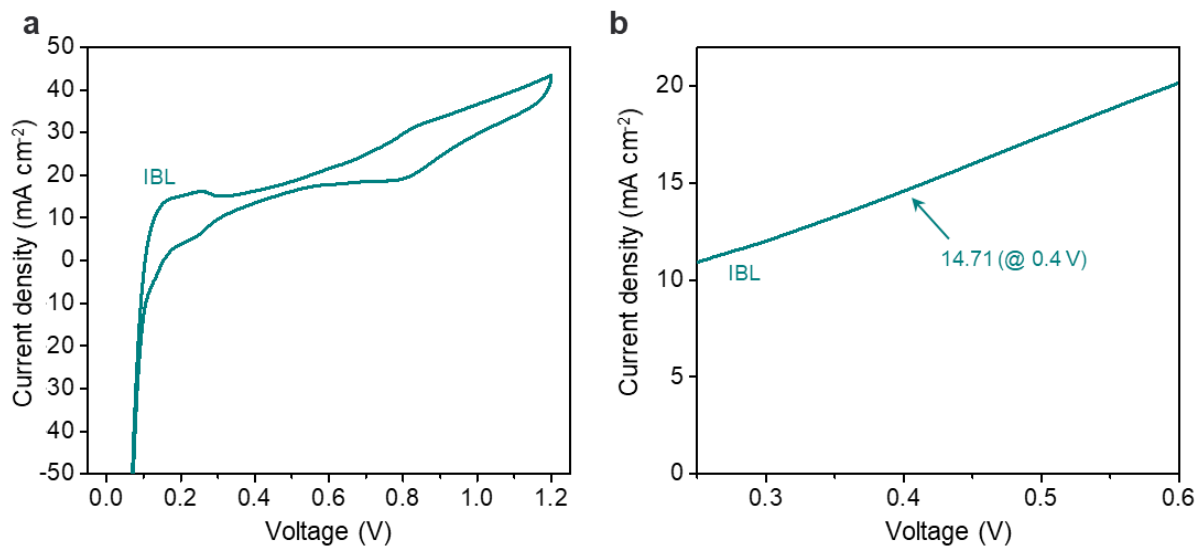


Figure 3.3.5. Performances of fuel cell using only IBL (without 2D materials). a) CV curve of fuel cell using only IBL. b) H₂ permeation current density measurement indicates that considerable gas crossover occurred. Inclined feature indicates internal short circuit in fuel cell using only IBL. For CV and H₂ permeation current density measurements, H₂ gas was supplied at anode (0.2 L min⁻¹) and N₂ gas was supplied at cathode (0.075 L min⁻¹). All measurements were done at atmospheric pressure condition.

Table 1. OCV, current density, and H₂ permeation current density values of fuel cells based on 2D materials and Nafion 211 film.

	Fuel/ Oxidant	1L-BN	1L-Gr	3L-BN (transferred)	3L-BN (AA'-stacked)	Nafion 211 (25 um)
Open circuit voltage (V)	H ₂ /Air	0.894	0.899	0.919	0.958	0.942
Current density @ 0.6 V (A cm ⁻²)	H ₂ /Air	1.04	1.05	0.88	1.00	1.30
Maximum power density (W cm ⁻²)	H ₂ /Air	0.68	0.67	0.63	0.66	0.86
Permeation current density @ 0.4 V (mA cm ⁻²)	H ₂ /Air	10.09	9.10	6.32	2.69	3.70

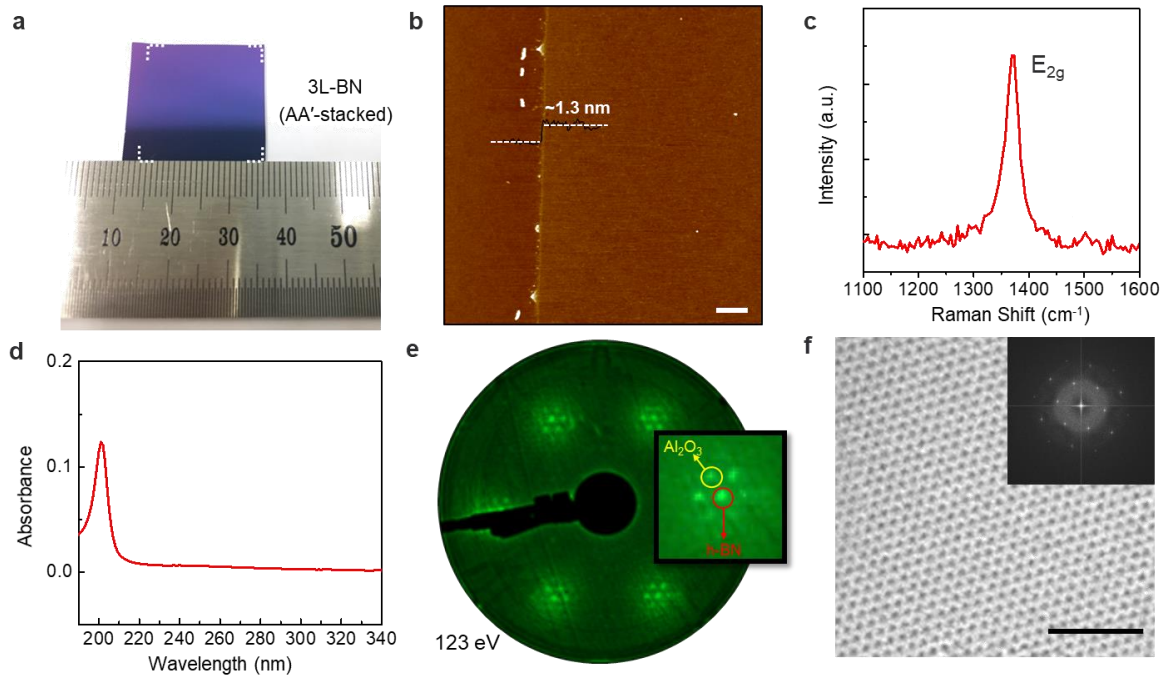


Figure 3.3.6. Characterization of trilayer BN with AA' stacking order. a) Photograph of 2 cm x 2 cm sized AA'-stacked 3L-BN transferred onto SiO₂ substrate. b) Atomic force microscope (AFM) image of AA'-stacked 3L-BN transferred onto SiO₂ substrate, indicating 1.3 nm thickness of AA'-stacked 3L-BN. Scale bar is 1 μm. c) Raman and d) UV-vis-NIR spectroscopy of AA'-stacked 3L-BN on Al₂O₃ substrate. e) Low-energy electron diffraction (LEED) pattern of single-oriented AA'-stacked 3L-BN on Al₂O₃ substrate, which was measured at 123 eV. The spots marked with red and yellow circles in zoomed-in LEED pattern correspond to h-BN and Al₂O₃, respectively. f) Transmission electron microscope top-view image of AA'-stacked 3L-BN and inset is fast Fourier transform image of AA'-stacked 3L-BN, which indicates AA' stacking order. Scale bar is 2 nm.

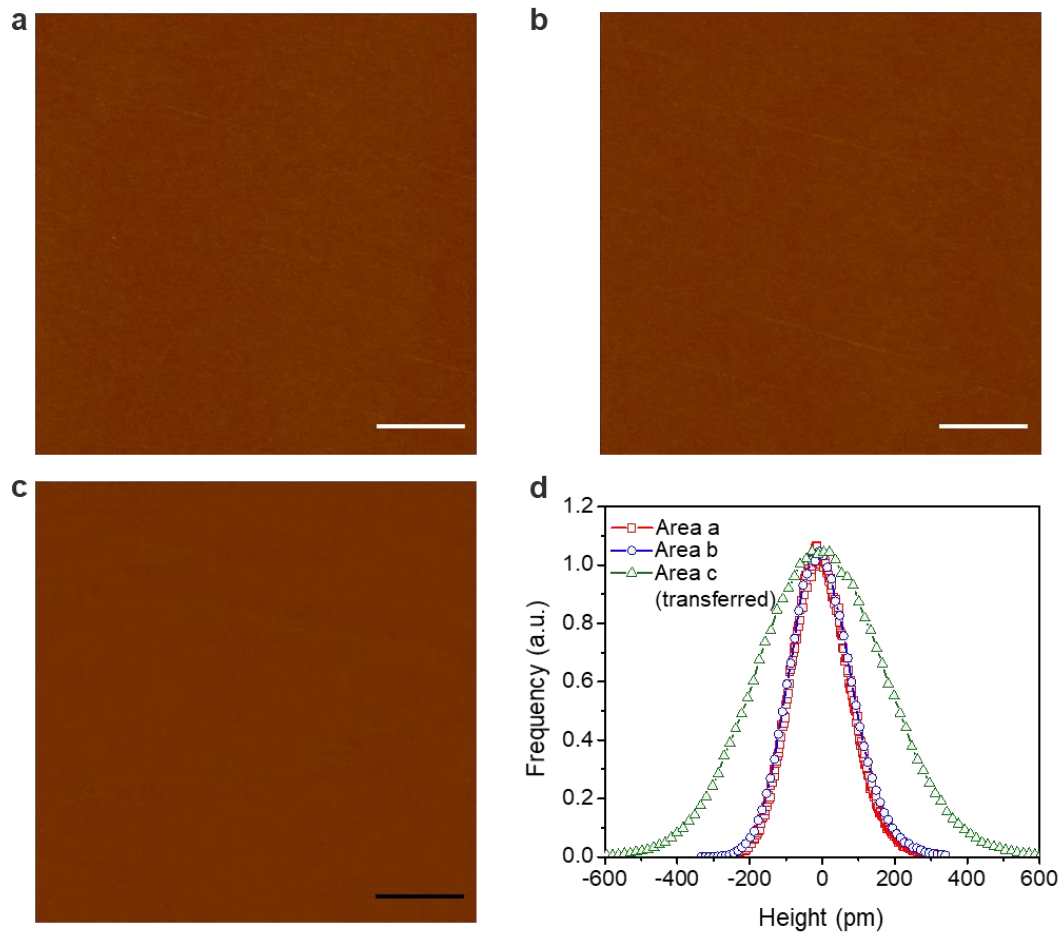


Figure 3.3.7. AFM images of AA'-stacked 3L-BN. 20 μm x 20 μm size AFM images of AA'-stacked 3L-BN on sapphire substrate (a and b were measured at different positions), which indicates wrinkle-free surface. Root mean square (RMS) roughness in a) and b) is 0.0913 and 0.0854 nm, respectively. c) From 10 μm x 10 μm size AFM image of AA'-stacked 3L-BN transferred onto SiO₂ substrate, indicating that AA'-stacked 3L-BN exhibits still smooth surface after transfer onto SiO₂ substrate. RMS roughness is 0.180 nm. White scale bars in (a and b) are 4 μm and black scale bar in c) is 2 μm . d) Histogram of height distribution (surface roughness) of area 1, 2, and 3 (corresponding to a to c) measured by AFM.

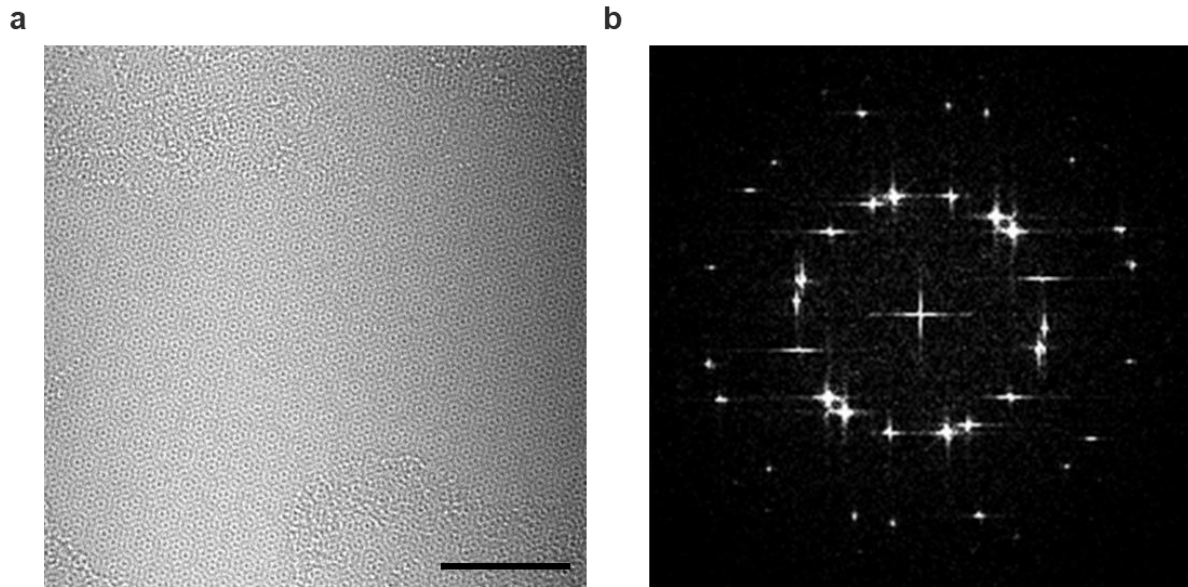


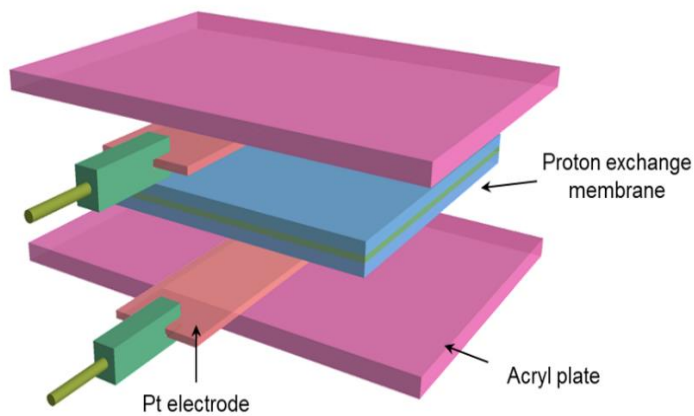
Figure 3.3.8. TEM results of 3L-BN-transferred. a) High-resolution TEM top-view image and b) diffraction pattern of 3L-BN-transferred. A Moiré pattern in top-view image and diffraction pattern indicates that 3L-BN-transferred shows turbostratic stacking order. Scale bar in a) is 5 nm.

3.3.6. Measurement of proton conductivity of performances of fuel cell using trilayer h-BN; turbostratic stacking and AA'-stacking

To measure proton conductivity of the used proton exchange membranes, we prepared Nafion 211 (25 μm), IBL/1L-BN/IBL (20 μm), and IBL/AA'-stacked 3L-BN/IBL (20 μm) samples which were same as those used in fuel cell evaluation. The membranes with size of 1.7 cm \times 1.7 cm were immersed in deionized water for 12 h. Then, the membranes were taken out from deionized water and immediately sandwiched between two Pt electrodes (0.5 cm \times 2.5 cm). The proton conductivity of each membrane was obtained by impedance spectroscopy using a Solartron Frequency Response Analyzer at room temperature. The measurements were conducted in potentiostatic mode in the frequency range from 4 MHz to 100 Hz with an oscillating voltage of 5 mV. The membrane based on AA'-stacked 3L-BN ensured proton transport, and its value is lower than that based on 1L-BN. Of course, the two membranes are worse than Nafion 211 in terms of proton conductivity. The proton conductivities of Nafion 211, 1L-BN, and AA'-stacked 3L-BN membranes are 0.030, 0.037, and 0.049, respectively. It was noted that intrinsic proton conductivity of Nafion 211 is better than those of 2D materials. Also, these results correspond to polarization data and power density curves, indicating that current density or maximum power density of Nafion 211 is higher than those of 2D materials. It was demonstrated that proton conductivity in 1L-BN is higher than AA'-stacked 3L-BN but AA'-stacked 3L-BN is suitable for proton exchange membrane due to low defects and low gas crossover.

3.3.7. Direct methanol fuel cell application of h-BN membranes

We confirmed whether AA'-stacked 3L-BN exhibits desirable performance as a proton exchange membrane in DMFCs. We fabricated and evaluated DMFCs using Nafion 212/Nafion 212, Nafion 212/AA'-stacked 3L-BN/Nafion 212, Nafion 212/3L-BN-transferred/Nafion 212. The polarization curves were measured by feeding 1 M methanol solution in the anode and air into the cathode. It was noted that the fuel cell based on AA'-stacked 3L-BN showed a higher power density (0.134 W cm^{-2}) than did the fuel cells based on 3L-BN-transferred (0.100 W cm^{-2}) and Nafion (0.110 W cm^{-2}) when operated at 70 $^{\circ}\text{C}$ in a 1 M MeOH solution. AA'-stacked 3L-BN, which is inserted in Nafion 211 membranes, reduced the crossover of MeOH without interfering with proton transport, while 3L-BN-transferred, when inserted between two Nafion 212 films in a sandwich-like structure, hindered proton transport because of its turbostratic stacking, resulting in the performance of the corresponding cell being slightly lower than that of the Nafion-based one. These results are consistent with polarization data and power density curves in PEMFCs using 2D materials.



	Proton conductivity (S cm ⁻¹)
IBL/AA'-stacked 3L-BN/IBL	0.030
IBL/1L-BN/IBL	0.037
Nafion 211	0.049

Figure 3.3.9. Schematic illustration of proton conductivity measurement system and results of proton conductivity. The resistance (R) of the membrane is measured by impedance spectroscopy. And, the proton conductivity (σ) of the membrane was calculated by using the equation,^{26,27} $\sigma = L/RWd$, where L is the distance between Pt electrodes, W is the width of the membrane, and d is the thickness of the membrane.

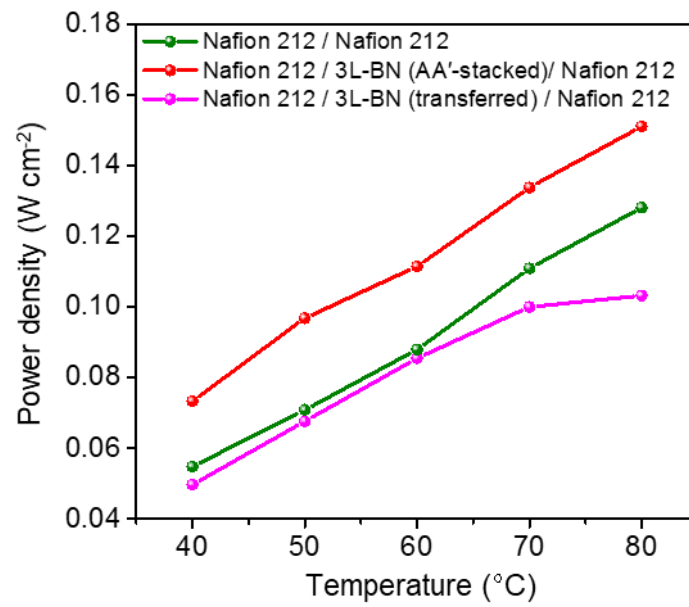


Figure 3.3.10. Comparison of performances of DMFCs using Nafion 212 (50 μm)/Nafion 212, Nafion 212/AA'-stacked 3L-BN/Nafion 212, Nafion 212/3L-BN-transferred/Nafion 212.

3.3.8. Accelerated stress test (AST) for fuel cell with 2D Materials

Since h-BN show high chemical and thermal stability, it is expected that the fuel cell with h-BN can show high stability against the radicals generated during fuel cell operation. To evaluate the stabilities of the various 2D materials, the changes in the OCV values over time of the cells based on single-layer h-BN (1L-BN), trilayer h-BN with AA'-stacking order (AA'-stacked 3L-BN), and Nafion 211 during the AST were compared. To provide harsh condition for prepared membranes, AST was conducted in more harsh condition (90 °C, 30% RH) than normal operation (70 °C, 100% RH). We measured evolution of OCV over time (100 h) of fuel cell with 1L-BN, AA'-stacked 3L-BN and Nafion 211 at the harsh condition. **Fig. 3.3.11.** exhibited that the OCV values of the fuel cells with 1L-BN and AA'-stacked 3L-BN are degraded by 5 % at a rate of 0.46 mV h⁻¹ after 100 h and by 10% at 0.8 mV h⁻¹. On the other hand, OCV of the fuel cell with Nafion 211 are degraded by 55% at 4.95 mV h⁻¹, which is much higher than degradation rate of 2D materials. Thus, as expected, the OCV degradation rate of the 2D materials was lower than that of Nafion 211 due to the excellent chemical stability of h-BN.

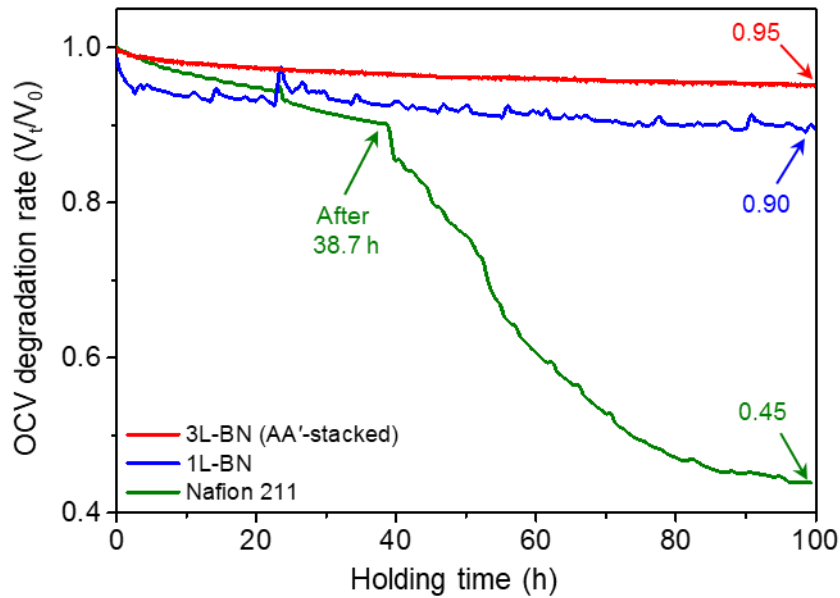


Figure 3.3.11. Evolution of open circuit voltage (OCV) over time of fuel cell using AA'-stacked 3L-BN, 1L-BN, and commercial Nafion 211 during accelerated stress test (AST). AA'-stacked 3L-BN and 1L-BN shows excellent chemical stability (See red and blue arrows for degradation rate after 100 h AST) compared to Nafion 211 (See green arrow). AST was operated at 90 °C, relative humidity 30%, and atmospheric pressure condition. H₂ gas (0.06 L min⁻¹) and Air (0.246 L min⁻¹) was used as fuel and oxidant, respectively.

3.3.9. Comparison of before and after AST for fuel cell with 2D materials

Finally, we compared the performance of the fuel cell with 2D materials before and after operation at harsh condition (AST) to evaluate stability of our fuel cells (**Fig. 3.3.12**, **Fig. 3.3.13** and **Table 2**). For measuring the performance of the fuel cell with 2D materials again, operation condition is set to 70 °C and 100% RH. In case of the fuel cell with AA'-stacked 3L-BN and 1L-BN, marginal changes in OCV values after 100 h of the AST. OCV of AA'-stacked 3L-BN and 1L-BN is changed to from 0.958 to 0.950 and 0.894 to 0.869, respectively. On the other hand, OCV of the cell based on Nafion 211 changed considerably from 0.942 to 0.6 V. Further, the H₂ permeation current densities of the cells based on AA'-stacked 3L-BN and 1L-BN decreased from 2.69 to 2.25 mA cm⁻² and from 10.08 to 9.4 mA cm⁻² at 0.4 V, respectively, indicating that the H₂ permeation current densities of the cells based on AA'-stacked 3L-BN and 1L-BN were slightly improved. In contrast, the Nafion 211 cell showed sharp changes in its CV curve and H₂ permeation current density (3.70 to 574.90 mA cm⁻² at 0.4 V), indicating that this cell could not be operated after 100 h of the AST.

Even though the variations in the H₂ permeation current densities of the 1L-BN and AA'-stacked 3L-BN cells before and after the AST were quite similar, their performances were different. The AA'-stacked 3L-BN cell exhibited similar power densities before (0.66 W cm⁻²) and after 100 h (0.63 W cm⁻²) of the AST. In contrast, the power density of the 1L-BN cell decreased from 0.68 to 0.51 W cm⁻². In case of fuel cell with commercial Nafion 211, the power density of the fuel cell with Nafion 211 was significantly reduced after the AST (it decreased from 0.83 W cm⁻² to 0.45 W cm⁻²); this result is consistent with the lowering in the OCV and H₂ permeation current density shown.

To understand these results, we measured cross-section SEM images of our membranes, which are used in performance tests and AST. **Fig. 3.3.14a** and **Fig. 3.3.14b** showed that membranes based on AA'-stacked 3L-BN before and after AST. It is noted that interfaces between catalyst (both cathode and anode) and of AA'-stacked 3L-BN membrane is not damaged before and after AST. Also, there is no crack and degradation inside of AA'-stacked 3L-BN membrane after AST. Generally, the chemical degradation mechanism of Nafion films is followed by two-step process: i) the formation of reactive radicals by H₂O₂, which is mostly generated when the H₂ gas (crossover of hydrogen gas) is changed to reactive 2H, and the 2H react with O₂ to form H₂O₂ ii) a reaction of highly reactive radicals such as hydrogen, hydroxyl, and hydrogen peroxide radicals with the proton exchange membrane.²²⁻²⁴ These reactive radicals result in the breakage of the carbon–sulfur bonds and sulfonated groups of Nafion to generate OCF₂ and SCF₂, leading to a decrease in PEMFC performance. Considering AA'-stacked 3L-BN membrane, it is noted that AA'-stacked 3L-BN is thermal stable and reduced H₂ gas crossover,

resulting in improvement of fuel cell stability at harsh condition. On the other hand, Nafion 211 film is fully degraded after AST (**Fig. 3.3.14a and Fig. 3.3.14b**). It is noted that interfaces between catalyst and Nafion 211 were damaged after AST, and cracks (blue arrows) and degradation of membranes were observed inside of the Nafion 211 after AST. Thus, it was demonstrated that reduction of performance of fuel cell with Nafion 211 is attributed to degradation of Nafion 211 while maintenance of performance of fuel cell with 2D materials is attributed to low gas crossover due to AA'-stacked 3L-BN.

In summary, for the first time, we fabricated MEAs using 2D materials without commercial Nafion films and evaluated the performances of fuel cells based on these MEAs. To improve the OCV values and H₂ permeation current densities of the pristine single-layer 2D materials, AA'-stacked 3L-BN was prepared, and it retarded gas crossover to a significant degree. Moreover, during the AST, the fuel cell based on AA'-stacked 3L-BN exhibited significantly higher chemical stabilities than did the cell based on Nafion, and even after the AST it was operated without any loss of performance, indicating that it can be operated at low humidity and high temperature. These results highlight the feasibility of monoatomic-thick membrane fuel cell (MMFC) using 2D materials as proton exchange membranes, as the fuel cells fabricated using these materials exhibited better thermal and chemical stabilities as compared to those of the cell based on Nafion.

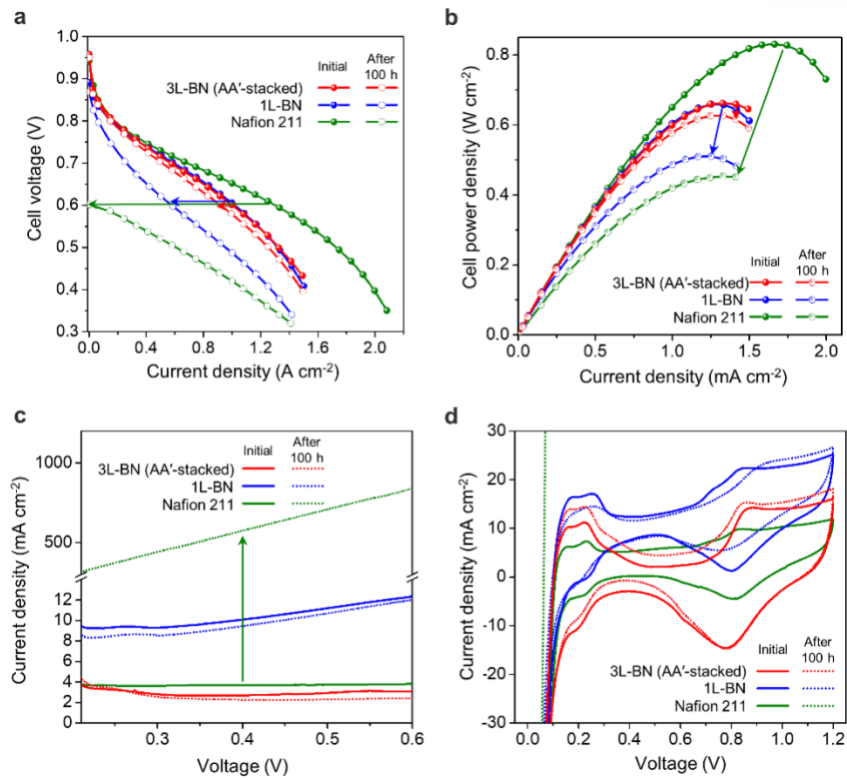


Figure 3.3.12. a-c) Comparison of fuel cells using AA'-stacked 3L-BN, 1L-BN, and commercial Nafion 211 before and after AST. a) Polarization curves, b) power density, and c) H_2 permeation current density results for AA'-stacked 3L-BN, 1L-BN, and Nafion 211 before and after AST. Current density and power density of Nafion 211 dramatically decreased after AST (See green arrow) compared to AA'-stacked 3L-BN and 1L-BN (see red and blue arrows, respectively). From c) H_2 permeation current density results, degradation of Nafion after AST was confirmed (See change of green graph).

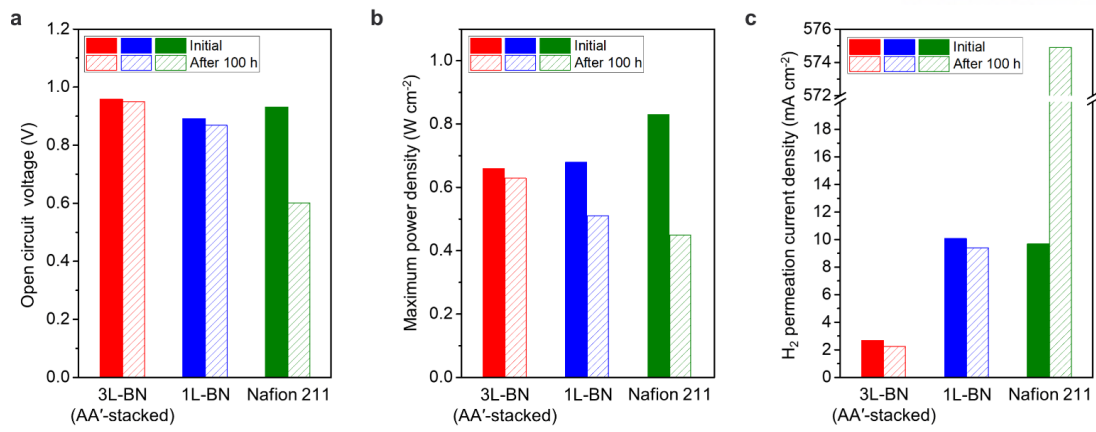


Figure 3.3.13. Changes in a) open circuit voltage, b) maximum power density, and c) H₂ permeation current density for each fuel cell before and after AST are described.

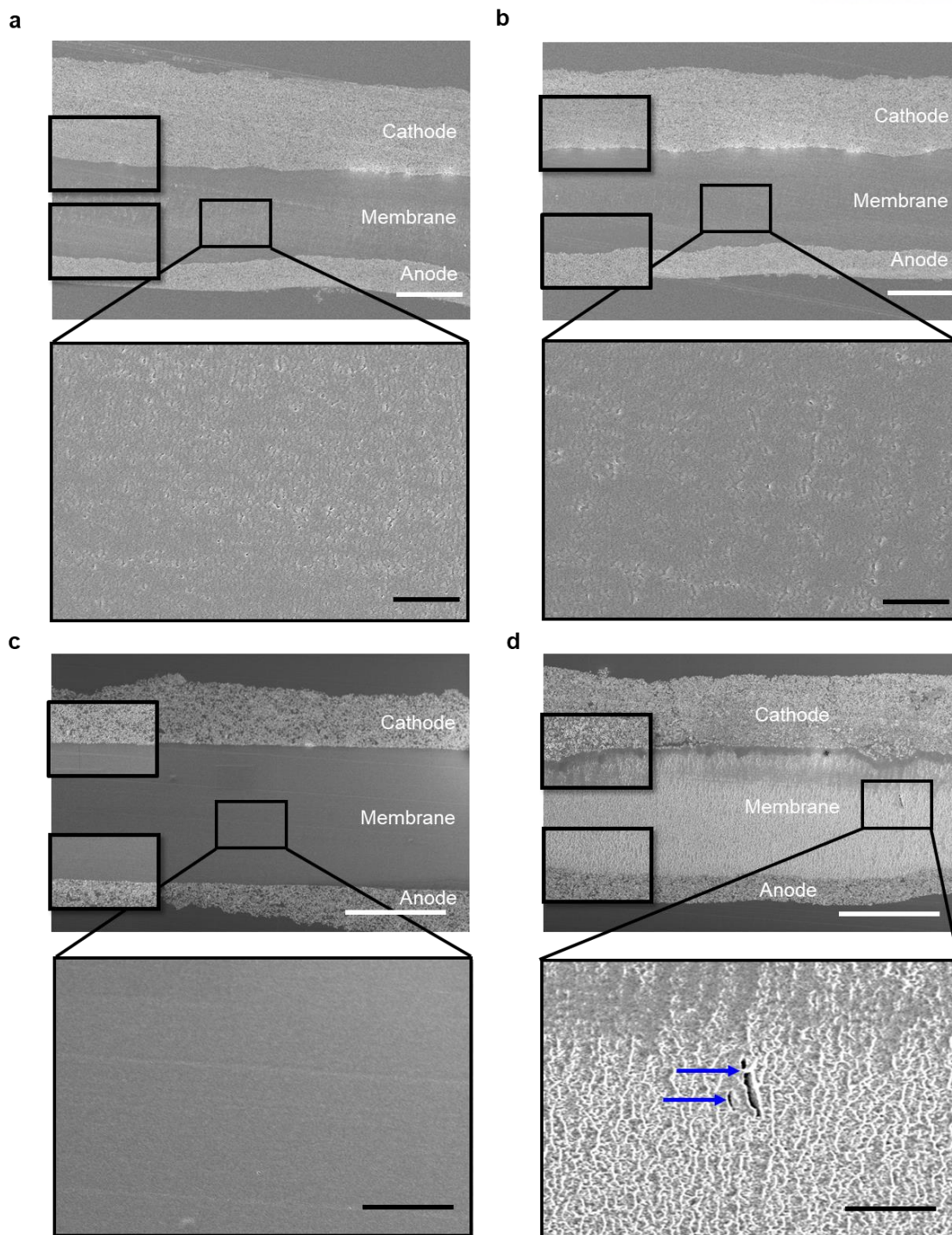


Figure 3.3.14. Comparison of cross-sectional SEM images of membranes using AA'-stacked 3L-BN and commercial Nafion 211 before and after AST. a-b) Cross-sectional SEM images of the MEA using the membrane based on AA'-stacked 3L-BN (IBL/ AA'-stacked 3L-BN/IBL) a) before and b) after AST. c-d) Cross-sectional SEM images of the MEA using Nafion 211 c) before and d) after AST. To measure cross-sectional SEM images, MEAs used in this work were cut by a microtome.

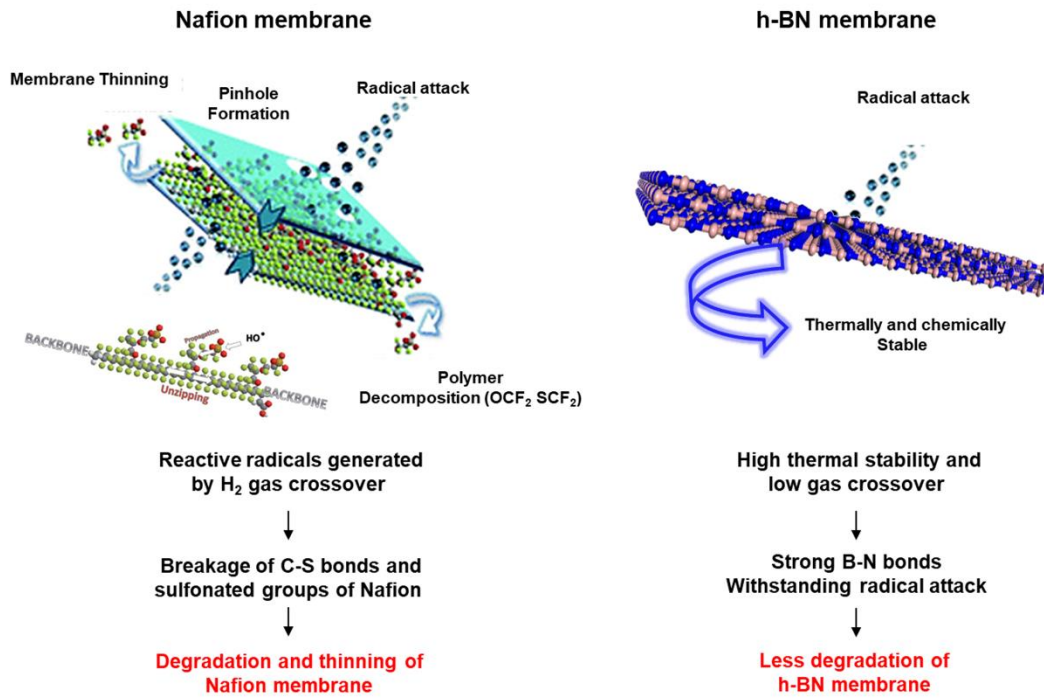


Figure 3.3.15. Comparison of degradation mechanism in case of Nafion and h-BN membrane at harsh condition. In case of Nafion, reactive radicals generated by gas crossover attack Nafion to break C-S bonds and sulfonated groups of Nafion. Thus, degradation and thinning of Nafion membrane were observed. Meanwhile, h-BN membrane has high thermal stability and low gas crossover. Also, it has strong B-N bonds, and so h-BN membrane withstands attack by reactive radicals. Therefore, less degradation of h-BN membrane was observed.

Table 2. OCV, current density, power density, and H₂ permeation current density of fuel cells using AA'-stacked 3L-BN, 1L-BN, and Nafion 211 film: before and after 100 h of accelerated stress test.

	3L-BN (AA'-stacked)		1L-BN		Nafion 211	
	Initial	After 100 h	Initial	After 100 h	Initial	After 100 h
Open circuit voltage (V)	0.958	0.950	0.894	0.869	0.942	0.600
Current density @ 0.6 V (A cm⁻²)	1.00	0.92	1.04	0.59	1.30	0
Maximum power density (W cm⁻²)	0.66	0.63	0.68	0.51	0.86	0.45
Permeation current density @ 0.4 V (mA cm⁻²)	2.69	2.25	10.09	9.40	3.70	574.90

3.4. References

- (1) Kim, H. W. *et al.* Selective gas transport through few-layered graphene and graphene oxide membranes. *Science*, **2013**, *342*, 91-95.
- (2) Celebi, K. *et al.* Ultimate permeation across atomically thin porous graphene. *Science*, **2014**, *344*, 289-292.
- (3) Huang, K.; Liu, G.; Lou, Y.; Dong, Z.; Shen J.; Jin, W. Graphene oxide membrane with highly selective molecular separation of aqueous organic solution. *Angew. Chem. Int. Ed.*, **2014**, *53*, 6929-6932.
- (4) Koenig, S. P.; Wang, L.; Pellegrino J.; Bunch, J. S. Selective molecular sieving through porous graphene. *Nat. Nanotech.*, **2012**, *7*, 728.
- (5) Homaeigohar S. and Elbahri, M. Graphene membranes for water desalination. *NPG Asia Mater.*, **2017**, *9*, e427.
- (6) Liu, G.; Jin, W. and Xu, N. Two-dimensional-material membranes: A new family of high-performance separation membranes. *Angew. Chem. Int. Ed.*, **2016**, *55*, 13384-13397.
- (7) Max, S. and Ravindra, P. Proton and hydrogen transport through two-dimensional monolayers. *2D Materials*, **2016**, *3*, 025004.
- (8) Shi, L.; Xu, A.; Chen, G. and Zhao, T. Theoretical understanding of mechanisms of proton exchange membranes made of 2D crystals with ultrahigh selectivity. *J. Phys. Chem. Lett.*, **2017**, *8*, 4354-4361.
- (9) Hu, S. *et al.* Proton transport through one-atom-thick crystals. *Nature*, **2014**, *516*, 227-230.
- (10) Lozada-Hidalgo, M. *et al.* Sieving hydrogen isotopes through two-dimensional crystals. *Science*, **2016**, *351*, 68-70.
- (11) Lozada-Hidalgo, M.; Zhang, S.; Hu, S.; Esfandiari, A.; Grigorieva, I. V. and Geim, A. K. Scalable and efficient separation of hydrogen isotopes using graphene-based electrochemical pumping. *Nat. Commun.*, **2017**, *8*, 15215.
- (12) Achtyl, J. L. *et al.* Aqueous proton transfer across single-layer graphene. *Nat. Commun.*, **2015**, *6*, 6539.

- (13) Peron, J.; *et al.* Properties of Nafion® NR-211 membranes for PEMFCs. *J. Membr. Sci.*, **2010**, *356*, 44-51.
- (14) Yan, X. H.; Wu, R.; Xu, J. B.; Luo, Z. and Zhao, T. S. A monolayer graphene – Nafion sandwich membrane for direct methanol fuel cells. *J. Power Sources*, **2016**, *311*, 188-194.
- (15) Holmes, S. M. *et al.* 2D crystals significantly enhance the performance of a working fuel cell. *Adv. Energy Mater.*, **2017**, *7*, 1601216.
- (16) Prasai, D.; Tuberquia, J. C.; Harl, R. R.; Jennings, G. K. and Bolotin, K. I. Graphene: corrosion-inhibiting coating. *ACS Nano*, **2012**, *6*, 1102-1108.
- (17) Wang, B.; Cuning, B. V.; Park, S-Y.; Huang, M.; Kim, J-Y. and Ruoff, R. S. Graphene coatings as barrier layers to prevent the water-induced corrosion of silicate glass. *ACS Nano*, **2016**, *10*, 9794-9800.
- (18) Zan, R.; Ramasse, Q. M.; Jalil, R.; Georgiou, T.; Bangert, U. and Novoselov, K. S. Control of radiation damage in MoS₂ by graphene encapsulation. *ACS Nano*, **2013**, *7*, 10167-10174.
- (19) Kim, G.; Kim, M.; Hyun, C.; Hong, S.; Ma, K. Y.; Shin, H. S. and Lim, H. Hexagonal boron nitride/Au substrate for manipulating surface plasmon and enhancing capability of surface-enhanced raman spectroscopy. *ACS Nano*, **2016**, *10*, 11156-11162.
- (20) Ahn, S.; Kim, G.; Nayak, P. K.; Yoon, S. I.; Lim, H.; Shin, H-J. and Shin, H. S. Prevention of transition metal dichalcogenide photodegradation by encapsulation with h-BN Layers. *ACS Nano*, **2016**, *10*, 8973-8979.
- (21) Jang, A. R. *et al.* Wafer-scale and wrinkle-free epitaxial growth of single-orientated multilayer hexagonal boron nitride on sapphire. *Nano Lett.*, **2016**, *16*, 3360-3366.
- (22) de Bruijn, F. A.; Dam, V. A. T. and Janssen, G. J. M. Review: durability and degradation issues of PEM fuel cell components. *Fuel Cells*, **2008**, *8*, 3-22.
- (23) Yu, T. H.; Sha, Y.; Liu, W-G.; Merinov, B. V.; Shirvastian, P. and Goddard, W. A. Mechanism for degradation of Nafion in PEM fuel cells from quantum mechanics calculations. *J. Am. Chem. Soc.*, **2011**, *133*, 19857-19863.
- (24) Chen, C.; Levitin, G.; Hess, D. W. and Fuller, T. F. XPS investigation of Nafion® membrane degradation. *J. Power Sources*, **2007**, *169*, 288-295.

- (25) Kim, G.; Jang, A-R.; Jeong, H. Y.; Lee, Z.; Kang, D. J. and Shin, H. S. Growth of High-crystalline, single-layer hexagonal boron nitride on recyclable platinum foil. *Nano Lett.*, **2013**, *13*, 1834-1839.
- (26) Lee, M-S.; Kim, T.; Park, S-H.; Kim, C-S. and Choi, Y-W. A highly durable cross-linked hydroxide ion conducting pore-filling membrane. *J. Mater. C*, **2012**, *22*, 13928-13931.
- (27) Wright, A. G. *et al.* Hexamethyl-p-terphenyl poly(benzimidazolium): a universal hydroxide-conducting polymer for energy conversion devices. *Energy Environ. Sci.*, **2016**, *9*, 2130-2142.

Chapter 4: Pt NPs/h-BN hybrid system for cathode

4.1 Introduction

In 2018, I reported a AA'-stacked tri-layer hexagonal boron nitride (AA'-stacked 3L-BN) membrane as a proton exchange membrane: A fuel cell based on the AA'-stacked 3L-BN membrane exhibited excellent chemical and thermal stability compared to commercial Nafion 211 membrane.¹ However, the current density and power density of the fuel cell based on Nafion 211 were higher than those of the fuel cell based on AA'-stacked 3L-BN. For a long time, researchers have focused on the cathode reaction of fuel cells, especially the transport resistance of oxygen in the cathode system.²⁻⁴ Transport resistance of oxygen and catalytically active sites constitute an important factor influencing the cathode reaction.^{5,6} Minimizing oxygen transport resistance while maintaining catalytically active sites is important for increasing the current density and power density of the fuel cell based on AA'-stacked 3L-BN. Furthermore, optimization of the amount of Pt nanoparticles might reduce costs. Herein, I studied a system consisting of Pt nanoparticles on h-BN. To prepare Pt nanoparticles, electrochemical and atomic layer deposition (ALD) were used.⁷⁻⁹ I prepared thin and uniform Pt nanoparticles on SiO₂ by means of ALD. The Pt nanoparticles were transferred onto the AA'-stacked 3L-BN by using a conventional transfer method, and I used the Pt nanoparticles on h-BN as the cathode of the fuel cell. I will introduce the preliminary results of this fuel cell system and plans for a new system.

4.2 Experimental process

4.2.1. Growth of trilayer h-BN

Trilayer h-BN with AA' stacking order was grown by a LPCVD method. A sapphire substrate (c-plane) was placed in the middle of a 2-inch alumina tube CVD furnace, and ammonia borane (97% purity, Sigma-Aldrich) was placed in a sub-chamber. The furnace was heated to 1400 °C under flow of Ar gas (10 sccm) and H₂ gas (10 sccm). The sub-chamber was heated to 130 °C for the decomposition of ammonia borane. The growth of trilayer h-BN with AA' stacking order on sapphire substrate was initiated by opening a valve of the sub-chamber. After opening a valve of the sub-chamber, source was supplied for 30 minutes. After growth completion, the furnace was cooled down to room temperature under Ar and H₂ gas.¹⁰

4.2.2. Preparation of Pt on substrate by electrochemical deposition

Pt NPs were prepared by electrochemical deposition methods. First, 0.1 M H₂PtCl₆ solution were prepared. For electrochemical deposition, bare Pt foil is negatively charged while target substrate is positively charged. With charge, Pt NPs are deposited onto target substrate.

4.2.3. Preparation of Pt on substrate by atomic layer deposition

Methylcyclopentadienyl Trimethyl-platinum were used as precursor. One cycle of atomic layer deposition (ALD) consists of pulse of precursor, counter-reactant and purging time. Precursor is pulsed for 2s. As counter-reactant, O₂ gas is pulsed with plasma. For purging, Ar is flowed for 10s. Temperature of target substrate is set to 300 °C. Optimized condition is 40 W and 300 cycles for Pt deposition.

4.2.4. Fabrication of fuel cells using 2D materials with prepared Pt nanoparticles

We developed a method to fabricate a fuel cell without any damage of 2D materials. The ink of anode and cathode catalysts was prepared by mixing 0.135 g Pt/C (HiSPEC-4000, Johnson-Matthey), 0.932 g of DI water, 0.186 g of isopropyl alcohol, and 0.999 g of 5 wt% Nafion ionomer (1100 EW, DuPont Fuel Cells). All cathodes and anodes had 27 wt% Nafion ionomer. The Pt contents on anode catalysts were controlled at 0.15 and 0.35 mg cm⁻², respectively.

The anode catalyst layer, which consisted of the Nafion ionomer and Pt/C, was spray-coated on a SiO₂ substrate (3.0 cm × 3.0 cm). The catalyst-coated SiO₂ substrate was dried completely to remove residual solvent in 80 °C. The Mylar anode sample was hot-pressed to sufficiently flatten the surface of the anode catalyst at 153 kgf cm⁻² and 30 °C for 30 sec. In this work, we coated an interfacial binding

layer (IBL) using 5 wt% Nafion solution (1100 EW, DuPont Fuel Cells) in the MEA fabrication process to create an 2D material/IBL structure because it is usually difficult to handle 2D materials that can be easily torn on the catalyst layer. To form the 2D material/IBL (thickness: 10 μm) structure, a CVD-grown graphene or h-BN sheet (size: 2 cm \times 2 cm) was transferred by typical transfer process. Prepared Pt NPs are transferred onto 2D materials/IBL/Anode. Furthermore, single-layer graphene was transferred onto encapsulating Pt NPs. Finally, Graphene/Pt NPs (cathode)/AA'-stacked h-BN/IBL/Anode were obtained.

4.2.5. Evaluation of fuel cells

The cathode and the anode were purged with N_2 (75 mL min^{-1}) and H_2 (200 mL min^{-1}) and then cyclic voltammetry (CV) and H_2 permeation current density were measured using an EIS potentiostat. The potential range and the scan rate were 0.04 to 1.2 V (vs. RHE) and 20 mV s^{-1} , respectively.

4.3 Results and discussions

The final structure of the new Pt NPs/h-BN hybrid system for the fuel cell cathode is depicted in **Fig. 4.3.2**. The most important aspect is the deposition of Pt nanoparticles on h-BN. For fuel cell measurement, Pt nanoparticles of sizes 10–15 nm are needed, considering the degradation, large surface area, and high stability of Pt nanoparticles.^{11,12} First, I will discuss the results of Pt deposition on h-BN. After then, I will deal with the new structure of Pt NPs/h-BN hybrid system for the fuel cell cathode.

4.3.1. Pt deposition on graphene by electrochemical deposition

For electrochemical deposition, 0.1 M of H_2PtCl_6 was prepared. Bare Pt foil was negatively charged, while the target substrate (graphene/ SiO_2) was positively charged. SEM images of 1min, 15min and 30min are depicted in **Fig. 4.3.3**. White Pt nanoparticles can be observed in the SEM images, indicating that Pt nanoparticles were successfully deposited onto the graphene surface. Because the surface energy of defects and grain boundaries is high,¹³⁻¹⁷ Pt nanoparticles are present on the grain boundaries and in defects. With increasing deposition time, the quantity of deposited Pt nanoparticles increased. However, at the deposition times of 15 and 30 min, the sizes of the Pt nanoparticles were 100–200 nm, which were larger than the target size. When I decrease deposition time to 1 min, size of Pt is still 30-40 nm. Moreover, as the deposition time was shortened and the concentration of H_2PtCl_6 was reduced, Pt deposition did not occur. Therefore, the atomic layer deposition method was introduced.

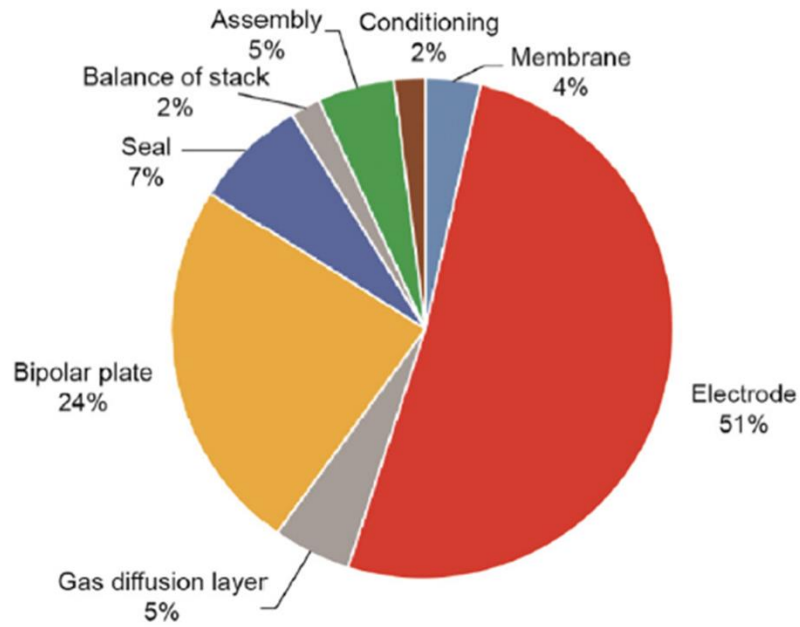


Figure 4.3.1. Portion of total fuel cell costs

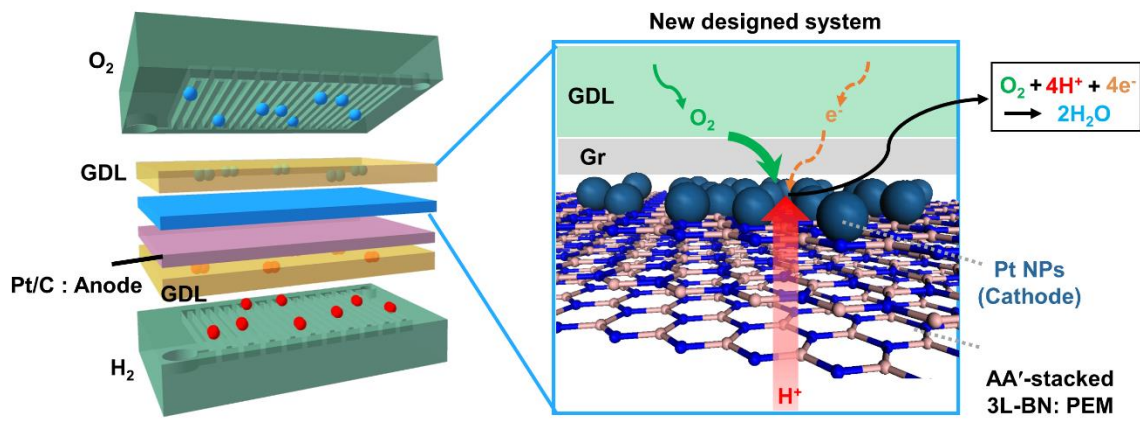


Figure 4.3.2. Schematic illustration of Pt NPs/h-BN hybrid system for cathode.

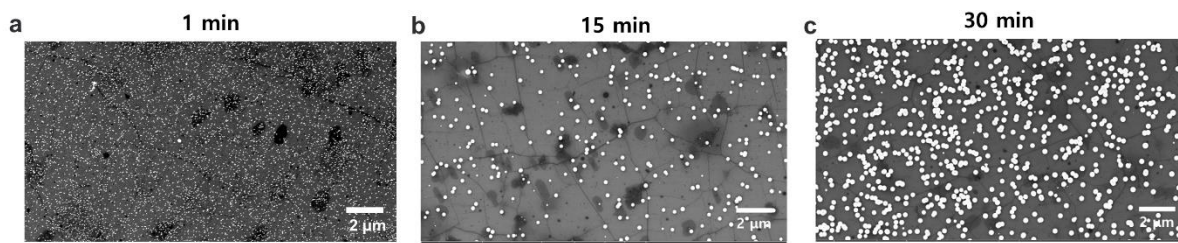


Figure 4.3.3. SEM images of Pt NPs on graphene by electrochemical deposition for a) 1 min, b) 15 min and c) 30 min.

4.3.2. Pt deposition on SiO₂ by atomic layer deposition

As alternative methods, atomic layer deposition (ALD) method were utilized. Methylcyclopentadienyl trimethyl-platinum were used as precursor. During ALD deposition, plasma treatment is needed and thus, graphene on SiO₂ was easily etched. Due to burning of graphene during ALD process, Pt deposition condition was not well-defined. To solve this problem, we deposited Pt NPs on SiO₂ substrate, directly. Optimized condition for ALD is 30 W and 300 cycles. **Fig. 4.3.4.** is SEM images of Pt NPs on SiO₂ substrate by ALD methods. Uniform with high density of Pt NPs were observed in prepared samples in **Fig. 4.3.4a**. In magnified image of **Fig. 4.3.4b**, size of Pt NPs is around 12 nm, which is suitable for fuel cell measurement.

4.3.3. Characterization of Pt NPs

To identify density of Pt NPs, we performed inductively coupled plasma (ICP) elemental analysis (Table 1). ICP elemental analysis demonstrated that mass per unit area of Pt NPs on SiO₂ is 0.36 mg cm⁻². For activation of fuel cell, over 0.3 mg cm⁻² is needed at least. Therefore, Pt NPs on SiO₂ by ALD could be used as cathode of fuel cell. For reduction of Pt NPs, annealing under H₂ gas was performed. Before annealing, large PtO peak was shown in XPS spectrum (**Fig. 4.3.5a**). However, after annealing with H₂ gas, only sharp Pt peak was shown, indicating that Pt NPs are successfully reduced (**Fig. 4.3.5b**).

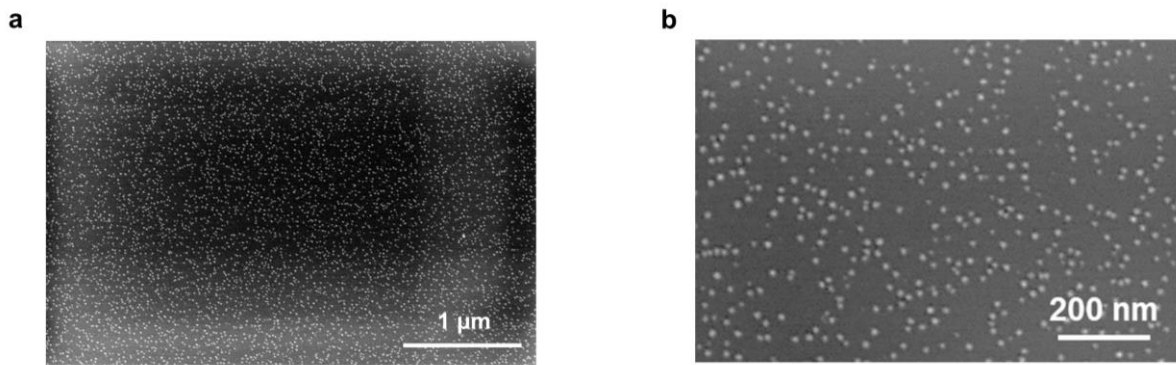


Figure 4.3.4. a) SEM images of Pt NPs on SiO₂ by ALD min and b) magnified image of a).

Table 1. ICP elemental analysis of Pt NPs on SiO₂ by ALD.

	Sol'n Conc.	Units	SD	%RSD	Int. (c.s)	Calc Conc.	DF
Pt	0.057	mg/kg	0.005	8.4	80.9	1.44 mg/kg	1.00

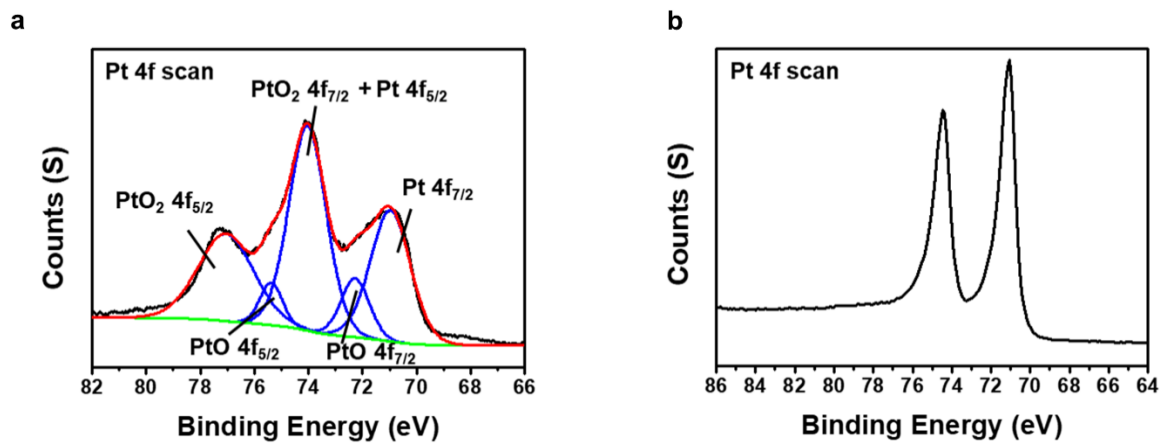


Figure 4.3.5. XPS spectra of Pt NPs on SiO₂ a) before and b) after annealing.

4.3.4. Fabrication of fuel cell based on Pt NPs/h-BN hybrid system and evaluation

A fuel cell based on the Pt NPs/h-BN hybrid system was fabricated and evaluated using methods similar to the ones described in **Chapter 3**. By spray coating the anode on the SiO₂ substrate, anode/SiO₂ was prepared. The 5 wt.% Nafion solution for the interfacial binding alyer (IBL) was spin-coated to form the AA'-stacked 3L-BN/IBL/anode structure for handling membrane electrodes assembly in an easier manner. As a cathode material, annealed Pt nanoparticles were transferred onto the AA'-stacked 3L-BN/IBL/anode to obtain a Pt nanoparticles/AA'-stacked 3L-BN/IBL/anode. By means of SEM analysis, I compared SEM images obtained before and after the transfer of Pt nanoparticles. Notably, Pt nanoparticles were successfully transferred by using typical transfer methods involving poly(methyl methacrylate) (**Fig. 4.3.6**). For encapsulating Pt nanoparticles, single-layer graphene was used to cover the Pt nanoparticles. Since graphene is a conducting material and is used here as an encapsulating material, it is expected that the Pt nanoparticles can be encapsulated without loss of current. I determined the H₂ permeation current density of the fuel cell based on the Pt NPs/h-BN hybrid system (**Fig. 4.3.7**). However, the H₂ permeation current density was excessive from the viewpoint of evaluating cell performance. This excessive H₂ permeation current density might be attributed to ample transfer processes compared to those in the previous experiment in **Chapter 3**. Moreover, the number of IBL layers used decreased from two in the previous experiment to one in the current experiment, and H₂ permeation current density was high. Notably, reducing the number of defects in 2D materials, which are generated during the transfer process, is crucial for realizing the proposed system.

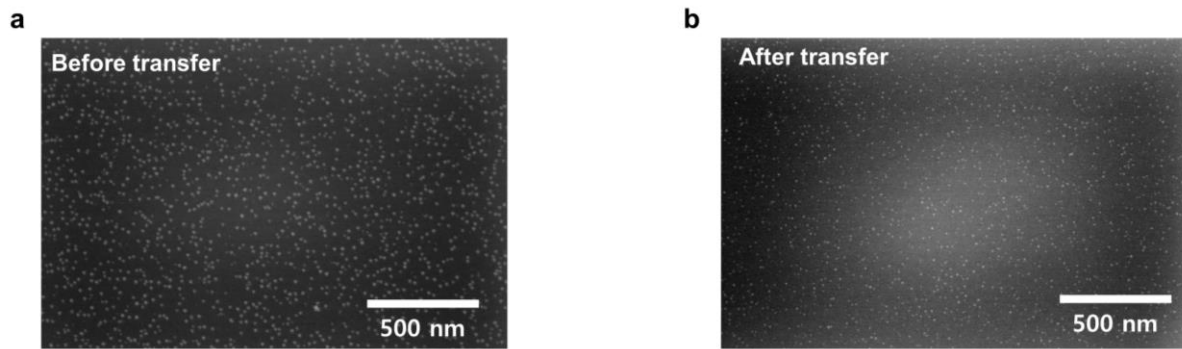


Figure 4.3.6. SEM images of Pt NPs on SiO₂ a) before and b) after transfer.

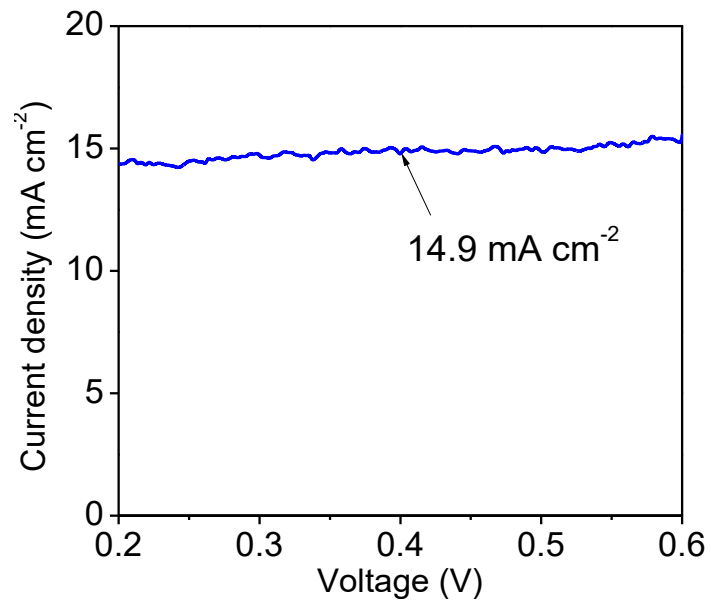


Figure 4.3.7. H₂ permeation current density of fuel cell based on Pt/h-BN hybrid cathode.

4.4. References

- (1) Yoon, S. I. *et al.*, AA'-Stacked trilayer hexagonal boron nitride membrane for proton exchange membrane fuel cells, *ACS Nano*, **2018**, *12*, 10764-10771.
- (2) Gasteiger, H. A.; Kocha, S. S.; Sompalli, B. and Wagner, F. T. Activity benchmarks and requirements for Pt, Pt-alloy, and non-Pt oxygen reduction catalysts for PEMFCs. *Appl. Catal., B*, **2005**, *56*, 9-35.
- (3) Yoon, W. and Weber, A. Z. Modeling Low-Platinum-Loading Effects in Fuel-Cell Catalyst Layers. *J. Electrochem. Soc.* **2011**, *158*, B1007-B1018.
- (4) Nonoyama, N.; Okazaki, S.; Weber, A. Z.; Ikogi, Y. and Yoshida, T. Analysis of oxygen-transport diffusion resistance in proton-exchange-membrane fuel cells. *J. Electrochem. Soc.*, **2011**, *158*, B416-B423.
- (5) Weber, A. Z. and Kusoglu, A., Unexplained transport resistances for low-loaded fuel-cell catalyst layers, *J. Mater. Chem. A*, **2014**, *2*, 17027.
- (6) Liu, H.; Epting, W. K. and Litster, S., Gas transport resistance in polymer electrolyte thin films on oxygen reduction reaction catalysts, *Langmuir*, **2015**, *31*, 9753-9858.
- (7) Yoon, T. *et al.* Healing graphene defects using selective electrochemical deposition: toward flexible and stretchable devices. *ACS Nano*, **2016**, *10*, 1539-1545.
- (8) Kim, K. *et al.* Selective metal deposition at graphene line defects by atomic layer deposition. *Nat. Commun.*, **2014**, *5*, 4781.
- (9) Yu, S. U. *et al.*, Simultaneous visualization of graphene grain boundaries and wrinkles with structural information by gold deposition. *ACS Nano*, **2014**, *8*, 8662-8668.
- (10) Jang, A. R. *et al.*, Wafer-scale and wrinkle-free epitaxial growth of single-oriented multilayer hexagonal boron nitride on sapphire. *Nano Lett.*, **2016**, *16*, 3360-3366.
- (11) Holby, E. F.; Sheng, W.; Shao-Horn, Y. and Morgan, D., Pt nanoparticle stability in PEM fuel cells: influence of particle size distribution and crossover hydroge. *Ener. Environ. Sci.*, **2009**, *2*, 865-871.
- (12) Shao-Horn, Y.; Sheng, W. C.; Chen, S.; Ferreira, P. J.; Holby E. F. and Morgan, D. Instability of supported platinum nanoparticles in low-temperature fuel cells. *Top. Catal.*, **2007**, *46*, 285-305.

- (13) Wang, B.; Puzyrev, Y. S. and Pantelides, S. T., Enhanced chemical reactions of oxygen at grain boundaries in polycrystalline Graphene. *Polyhedron*, **2013**, *64*, 158–162.
- (14) Wang, X.; Tabakman, S. M. and Dai, H. Atomic layer deposition of metal oxides on pristine and functionalized graphene. *J. Am. Chem. Soc.* **2008**, *130*, 8152–8153.
- (15) Xuan, Y. *et al.* Atomic-layer-deposited nanostructures for graphene-based nano electronics. *Appl. Phys. Lett.* **2008**, *92*, 013101.
- (16) Xie, G. *et al.* Graphene edge lithography. *Nano Lett.* **2012**, *12*, 4642–4646.
- (17) Javey, A. *et al.* High-k dielectrics for advanced carbon-nanotube transistors and logic gates. *Nat. Mater.* **2002**, *1*, 241–246.

Chapter 5: Conclusion and Future Work

5.1 Conclusion

The main goal of this dissertation is application of 2D materials for membranes. In first part, I studied polymerization reaction in graphene sandwich, which introduced as a novel 2D confined space platform. Monomers such as dopamine, oPD and EDOT were prepared in graphene sandwich, and prepared monomers were polymerized in graphene sandwich by simple heating. Normally, these monomers are polymerized as linear and amorphous form in bulk space, but these monomers are polymerized as 2D and polycrystalline form in confined space. 2D sheet-like structures of polymers in confined space were confirmed by TEM. Polycrystalline characteristics were confirmed by diffraction pattern and GI-WAXD. These 2D polymer formed superlattices with two graphene layers, and so zone-folding effect occurs, which is attributed to G band enhancement. It is noted that 2D polycrystalline polymerization reaction depends on structure of monomers in graphene sandwich. Planar and 6-membered ring monomer is preferred for 2D polycrystalline polymerization reaction in graphene sandwich. Further, we observed improved sheet resistance, bending stability and Young's modulus of graphene by using polydopamine. This study demonstrated that chemical reaction of organic substances in graphene sandwich (confined space), for the first time. This study extends comprehensive understanding of reaction in confined space.

Meanwhile, we fabricated fuel cell with h-BN proton exchange membranes, which is a primary proton exchange membrane, for the first time. We utilized CVD-grown h-BN and demonstrated that AA'-stacked 3L-BN is superior to 1L-BN for PEMFCs. CVD-grown 1L-BN has intrinsic defects, leading to high H₂ gas crossover, despite a good maximum power density. To resolve this issue, we used AA'-stacked 3L-BN, which was synthesized on a sapphire substrate via CVD. Based on the configuration of AA'-stacked 3L-BN, the fuel cell with AA'-stacked 3L-BN exhibited enhanced OCV and H₂ gas crossover performance (OCV = 0.957 V, H₂ permeation current density @ 0.4 V = 2.35 mA cm⁻²) while maintaining a high maximum power density (0.657 W cm⁻²). Additionally, we performed stability tests on fuel cells with 2D materials and commercial Nafion under harsh conditions. In the case of fuel cells with 2D materials, the OCV degradation rate was low (5% for AA'-stacked 3L-BN and 10% for 1L-BN), because 2D materials have excellent thermal and chemical stability. In contrast, OCV degradation rate of Nafion was high (approximately 56% over 100 h) because the Nafion membrane was fully degraded. In high-gas-crossover systems, reactive radicals are easily formed, leading to the degradation of Nafion membranes. When they compared the performance of fuel cells with 2D materials and Nafion, the fuel cells with 2D materials maintained their performance, whereas the fuel cells with

Nafion did not maintain their performance. These results demonstrated the feasibility of fuel cells with 2D materials, which provide excellent thermal and chemical stability.

Furthermore, I studied a system consisting of Pt nanoparticles on h-BN to reduce the cost of Pt and oxygen resistance in cathode reactions. In the proposed system, the deposited Pt nanoparticles act as the cathode catalyst. I used the ALD method to obtain uniform and high-density Pt nanoparticles with sizes of 10–15 nm, which is the target size. The prepared Pt nanoparticles were adequate for activating the fuel cell based on the novel Pt/h-BN hybrid system. However, because of excessive H₂ permeation current density, cell evaluation was not possible. To overcome this problem, reducing the number of defects generated during the transfer process is essential.

5.2 Future work

Since high vdW pressure presents in graphene sandwich, graphene sandwich could be used for reaction vessel that needs high pressure for synthesis. Also, confined space inside graphene sandwich is a clean space, which is not affected by bulk environment. Therefore, graphene sandwich can be used for reactions that needs inert or clean conditions. In future studies, extracting the required products from the graphene sandwich structure can be an important topic. The graphene sandwich structure is very strong, which makes it difficult to extract products from it. This warrants the use of external force. Herein, I proposed two methods for extracting products from the graphene sandwich structure. One method involves subjecting the structure to H₂ plasma treatment. Usually, H₂ plasma treatment is widely used for etching graphene on a substrate. The etching condition is related to the flow rate and pressure of hydrogen gas, plasma power, and plasma time. By optimizing the etching condition, one can etch only the top-layer graphene from G/product/G, and it might be possible to obtain product/G sample. The second method involves tearing away the top and bottom graphene layers by applying an external force. In this method, Ni film deposition is performed on both the top and bottom layers of G/product/G to obtain Ni/G/product/G/Ni. It is known that the interaction between Ni-G is considerably stronger than that between product-G. Thus, by physically splitting it, one might obtain product/Gr./Ni samples. This would help analyze the exact structure of the product formed in the confined space by using scanning tunneling microscopy and other tools. Such knowledge would facilitate fundamental studies of chemistry in confined spaces

For future studies on h-BN for proton exchange membranes, the development of synthesis techniques for large-scale single-crystal h-BN will be crucial. In addition to it, another important issue is the development of techniques to handle very thin h-BN layers, because it is very difficult to handle atomic thick materials for a device fabrication. The development of fuel cells using h-BN will facilitate higher-temperature operation of PEMFCs. In conventional PEMFCs, commercial Nafion have been widely used as proton exchange membranes. Typically, PEMFCs with commercial Nafion are operated at low temperatures (approximately 80 °C) based on the poor thermal stability of Nafion. Because h-BN exhibits excellent thermal stability compared to polymers, it is expected that fuel cells utilizing h-BN could be operated at higher temperatures compared to conventional operation conditions. Proton conductivity is proportional to temperature, so the operation of PEMFCs with h-BN at higher temperatures is expected to improve the power density of fuel cells. Additional to high temperature fuel cell, h-BN has a potential of hydrogen storage system due to inertness to extreme conditions. Even though it is expected that h-BN is excellent membranes for proton exchange membrane or hydrogen storage, synthesis of large-scale single crystal h-BN is crucial for real-world application.

Publication Lists

1. H. Lim, **S. I. Yoon**, G. Kim, A. R. Jang and H. S. Shin* “Stacking of two-dimensional materials in lateral and vertical directions” *Chem. Mater.* **2014**, *26*, 4891.
2. A. R. Jang, S. Hong, C. Hyun, **S. I. Yoon**, G. Kim, H. Y. Jeong, T. J. Shin, S. O. Park, K. Wong, S. K. Kwak, N. Park, K. Yu. E. Choi, A. Mishchenko, F. Withers, K. Novoselov, H. Lim* and H. S. Shin* “Wafer-scale and wrinkle-free epitaxial growth of single-orientated multilayer hexagonal boron nitride on sapphire” *Nano Lett.* **2016**, *16*, 3360.
3. S. J. Ahn, G. Kim, P. K. Nayak, **S. I. Yoon**, H. Lim, H-J. Shin and H. S. Shin* “Prevention of transition metal dichalcogenide photodegradation by encapsulation with h-BN layers” *ACS Nano* **2016**, *10*, 8973.
4. K. Y. Ma, **S. I. Yoon**, A-R. Jang, H. Y. Jeong, Y-J. Kim, P. K. Nayak and H. S. Shin* “Hydrogenation of monolayer molybdenum diselenide via hydrogen plasma treatment” *J. Mater. Chem.* **2017**, *5*, 11294-11300.
5. H. J. Jo, J. H. Lyu, R. S. Ruoff, H. Lim, **S. I. Yoon**, H. Y. Jeong, T. J. Shin, C. W. Bielawski * and H. S. Shin* “Conversion of Langmuir-Blodgett monolayers and bilayers of poly (amic acid) through polyimide to graphene” *2D Materials* **2017**, *4*, 014005.
6. D. Fu, X. Zhao, Y-Y. Zhang, L. Li, H. Xu, A-R. Jang, **S. I. Yoon**, P. Song, S. M. Poh, T. Ren, Z. Ding, W. Fu, T. J. Shin, H. S. Shin, S. T. Pantelides, W. Zhou and K. P. Loh* “Molecular beam epitaxy of highly crystalline monolayer molybdenum disulfide on hexagonal boron nitride” *J. Am. Chem. Soc.* **2017**, *4*, 014005.
7. **S. I. Yoon**, D. J. Seo, G. Kim, M. Kim, C. Y. Jung, Y. G. Yoon, S. H. Joo, T. Y. Kim* and H. S. Shin* “AA'-stacked trilayer hexagonal boron nitride membrane for proton exchange membrane fuel cells” *ACS Nano* **2018**, *12*, 10764-10771.
8. S. Lee, S. H. Jung, A-R. Jang, **S. I. Yoon**, H. S. Shin and J. Lee* “Large area patterning of residue-free metal oxide nanostructures by liquid transfer imprint lithography” *Nanotechnology* **2019**, *30*, 235301.
9. J. H. Yang, H. W. Yang, B. O. Jun, J. H. Shin, S. Kim, A-R. Jang, **S. I. Yoon**, H. S. Shin, D. Park, K. Park, D. Yoon, J. I. Sohn, S. Cha, D. J. Kang and J. E. Jang* “Improving radio frequency transmission properties of graphene via carrier concentration control toward high frequency transmission line applications” *Adv. Funct. Mater.* **2019**, *29*, 1808057.
10. G. Kim, S. S. Kim, J. Jeon, **S. I. Yoon**, S. Hong, Y. J. Cho, A. Misra, S. Ozdemir, D. Ghazaryan, A. Mishchenko, D. V. Andreeva, Y. J. Kim, H. J. Chung, A. K. Geim, K. S. Novoselov*, B. S. Sohn* and H. S. Shin* “Planar and van der Waals heterostructures for vertical tunnelling single electron transistors” *Nat. Commun.* **2019**, *10*, 230.
11. H. Yamaguchi, F. Liu, J. DeFazio, M. Gaowei, L. Guo, A. Alexander, **S. I. Yoon**, C. Hyun, M. Critchley, J. Sinsheimer, V. Pavlenko, D. Strom, K. L. Jensen, D. Finkenstadt, H. S. Shin, M. Yamamoto, J. Smedley and N. A. Moody* “Quantum efficiency enhancement of bialkali photocathodes by an atomically thin layer on substrates” *Phys. Status Solidi A* **2019**, *10*, 1900501.

Acknowledgement

박사 과정을 마무리하며 시간이 많이 지났다는 것을 느낍니다. 돌이켜보니 박사과정을 하면서 정말 많은 분들께 도움을 받았다는 것을 다시 한번 느낍니다. 먼저 지도교수인 신현석 교수님께 감사인사를 전하고 싶네요. 교수님 덕분에 다양한 경험도 할 수 있었고, 연구자로서 지녀야할 태도에 대해서 가르침을 받은 것 같습니다. 그리고 학위 심사를 흔쾌히 해 주신 김태영 박사님, 이종훈 교수님, 주상훈 교수님, 박혜성 교수님께 감사드리고 싶습니다. 그리고 제 메인 연구에 큰 도움을 준 코워커 효주와 동준이 형에게도 감사하다고 전하고 싶습니다.

학위 기간 동안 연구자로서 올바른 길을 갈 수 있게 많은 도움을 주신 랩 선배들께도 감사드립니다. 현섭이 형, 아랑이 형, 지은 누나, 동우 형 덕분에 맛있는 것도 정말 많이 얻어먹었고, 대학원생 생활과 실험 관련 많은 조언을 받아서 무사히 잘 졸업한 것 같습니다. 그리고 동기인 성준이랑 광우 덕분에 재미있게 학위를 마칠 수 있었던 것 같습니다. 훈주형, 경열이형, 영진이형 후배님들. 돌이켜보면 장난도 많이 하고 잔소리도 많이 한 거 같은데 잘 받아줘서 고맙고, 석모, 현태, 민수도 고생하고 있는데 다들 더 힘내서 빨리 졸업했으면 좋겠네요. 이번에 새롭게 들어올 형준이도 힘든 시간이 될 거라고 생각하지만 극복할 수 있을 거라고 생각합니다. 그리고 졸업하고 울산을 떠난 혜진이, 초희, 윤정이, 한재 앞날에 행운을 빌어주고 싶네요.

학교에서 축구를 하며 만난 친구들이 생각이 많이 나네요. 학교 후문에서 축구 끝나고 술 마시던 승영이랑 윤호. 재밌는 이야기도 많이 하고 도움도 많이 받은 거 같아 고맙다고 말하고 싶습니다. 커피를 통해 일하는 동기부여를 잘 확립해준 배명환님, 무거동 능력 좋은 사람 김민우님, 대리 마을 두벽이 김지훈님들 덕분에 무미건조한 대학원생 생활이 조금 더 재밌었던 것 같네요. 또 마지막 룸메이트 성철이, 같은 아파트 주민 민구님, 돌이켜 보니 같이 나이 들면서 재밌는 기억들이 많은 거 같아 고맙다고 전하고 싶습니다.

마지막으로 지금까지 저를 기다려준 부모님께도 감사하다고 전하고 싶고, 고생하고 있는 친형에게도 고맙고 사랑한다고 전하고 싶습니다. 엄청 긴 시간이었지만 그 기간동안 생각보다 더 많은 걸 배웠다고 말을 할 수 있을 것 같습니다. 다시 한번 학위를 마칠 수 있게 도움 주신 많은 분들께 진심으로 감사드립니다. 더 좋은 연구자가 되도록 노력하는 사람이 되겠습니다.